

**Ionization Dynamics and
Magnetorotational Instability in
Protoplanetary and Circumplanetary Disks**

原始惑星系円盤及び周惑星円盤における
電離度のダイナミクスと磁気回転不安定性

Yuri I. Fujii

Laboratory for Theoretical Astronomy & Astrophysics (Ta-Lab)

Department of Physics, Nagoya University

Furo-cho, Chikusa-ku, Nagoya, Aichi 464-8602, Japan

Abstract

Gaseous disks form around young stars as by-products of star formation. Because planets are formed in them, these disks are called protoplanetary disks. Protoplanetary disks consist of mainly molecular hydrogen and atomic helium, and dust grains account for about 1% of the total mass. Dust grains are thought to be the building blocks of planets. Various astronomical observations suggest gas accretion toward the central star. Such mass accretion implies that the angular momentum of the gas is transported outward. The most promising mechanism of this is magnetohydrodynamical (MHD) turbulence driven by the magnetorotational instability (MRI). For the MRI to operate, the ionization degree must be sufficiently high. However, because of their low temperature and high density, the ionization degree of protoplanetary disks is very low. Neutral gas is ionized by ionization sources such as cosmic rays, X-rays and UV from the central star, and radionuclides, and various resultant particles are formed. In this thesis, we first develop a method to solve the rate equations governing the ionization chemistry quickly and accurately. Next, we investigate the viability of the MRI in circumplanetary disks, gaseous disks formed around newly-born gas giants, utilizing our method of calculation of ionization degree. We find that well-developed MHD turbulence cannot be sustained in circumplanetary disks. Because satellites are thought to form in circumplanetary disks, our results

suggest that satellite formation may take place over a long timescale in a quiescent disk. Finally, we implement our ionization degree calculation scheme into the Athena MHD code and investigate the effects of ionization dynamics. When the disk has mostly dissipated and tiny dust grains have grown larger, we find that the ionization degree in the surface layer becomes smaller than the equilibrium value for the corresponding density. This is because a disk wind transports the low ionization degree gas in the lower layers to the surface layer. This effect is also expected to be important in the complicated chemical evolution of protoplanetary disks.

Contents

| | |
|--|-----------|
| Abstract | ii |
| 1 Introduction | 1 |
| 1.1 Protoplanetary Disks as Sites of Planet Formation . . . | 1 |
| 1.1.1 Observations of Protoplanetary Disks | 1 |
| 1.1.2 Theory of Protoplanetary Disks | 5 |
| 1.2 Circumplanetary Disks as Sites of Satellite Formation . | 8 |
| 1.3 Magnetorotational Instability as a Mechanism for Mass Accretion | 10 |
| 1.3.1 MHD Turbulence | 10 |
| 1.3.2 Conditions for MRI Growth | 10 |
| 2 Time-dependent Calculation of Ionization Degree | 14 |
| 2.1 Reactions and Equations | 14 |
| 2.1.1 Gas Phase Reactions | 14 |
| 2.1.2 Grain Surface Reactions | 15 |
| 2.1.3 Basic Equations | 17 |
| 2.1.4 Ionization Rate | 19 |
| 2.1.5 Rate Coefficients | 21 |

| | | |
|----------|--|-----------|
| 2.2 | Fast and Accurate Method for Ionization Degree Calculations | 23 |
| 2.2.1 | Gaussian Approximation of Charge Distribution of Dust Grains | 23 |
| 2.2.2 | Piecewise Exact Solution Method | 27 |
| 2.3 | Test Calculations | 29 |
| 3 | Viability of the Magnetorotational Instability in Circumplanetary Disks | 32 |
| 3.1 | Ionization Degree in Circumplanetary Disks | 32 |
| 3.1.1 | Properties of Circumplanetary Disks | 33 |
| 3.1.2 | Limitations of Standard Model | 34 |
| 3.2 | Alternative Disk Models | 39 |
| 3.2.1 | Surface Density Evolution | 39 |
| 3.2.2 | Analytic Treatment | 41 |
| 3.2.3 | MRI Activity in Circumplanetary Disks | 43 |
| 3.3 | Implications | 51 |
| 4 | Ionization Dynamics in Protoplanetary Disks | 54 |
| 4.1 | Effects of Non-equilibrium Ionization | 54 |
| 4.2 | A Toy Model of Turbulent Mixing | 55 |
| 4.3 | Timescales | 58 |
| 4.4 | MHD Simulations | 72 |
| 4.4.1 | Simulation Setup | 72 |
| 4.4.2 | Results | 76 |
| 4.5 | Conclusions and Discussion | 87 |

| | |
|---------------------------------------|-----------|
| Contents | vi |
| 5 Summary and Future Prospects | 90 |
| Acknowledgments | 96 |

Chapter 1

Introduction

1.1 Protoplanetary Disks as Sites of Planet Formation

A variety of observations have suggested the presence of substantial gas accretion disks around young stellar objects. Because planets are thought to form in these disks, they are called protoplanetary disks. Protoplanetary disks are by-products of star formation.

1.1.1 Observations of Protoplanetary Disks

Because spatially resolving large samples of protoplanetary disks is difficult, the spectral energy distribution (SED) is often used to discuss statistical measures such as disk frequency and lifetime. The SED is the distribution of radiative flux or brightness as a function of frequency or wavelength. Protostars and pre-main sequence stars, or young stellar objects (YSOs), are classified into four groups based on the slope of their SEDs (Andre et al., 1993; Armitage, 2009; Lada, 1987). The spectral index, defined as

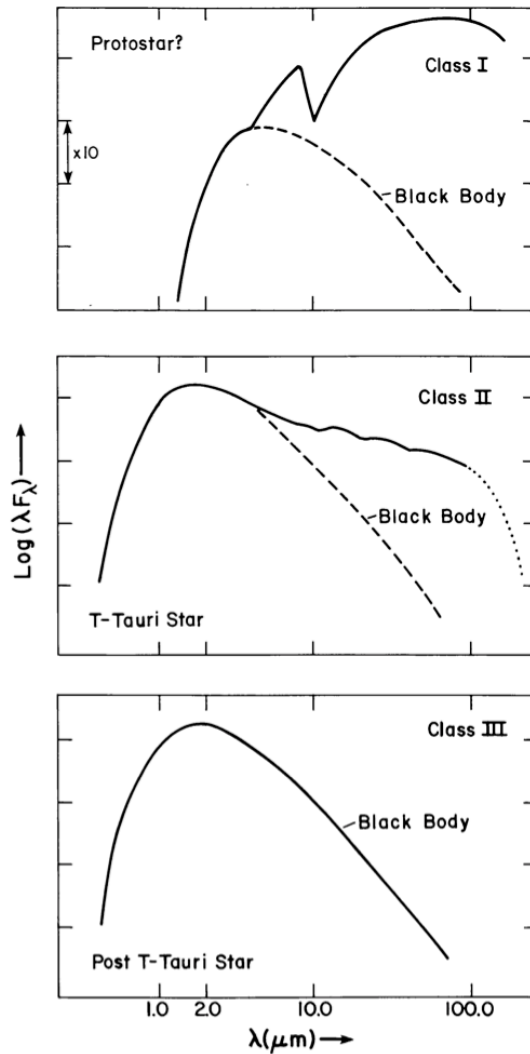


Figure 1.1: Classification scheme for the energy distributions of embedded YSOs taken from Figure 2 of Lada (1987).

$$\alpha_{\text{IR}} \equiv \frac{d \log(\lambda F_{\lambda})}{d \log(\lambda)}, \quad (1.1)$$

where λ is wavelength and F_{λ} is flux density, is calculated in the wavelength range from near-IR to mid-IR (typically $2.2 \mu\text{m}$ to 10 or $24 \mu\text{m}$). When near-IR emission is not detected and the SED peaks in the far-IR or at mm wavelengths, the object is classified as Class 0. This corresponds to the cloud-collapse phase, the earliest stage of star formation, during which protostars are deeply embedded within

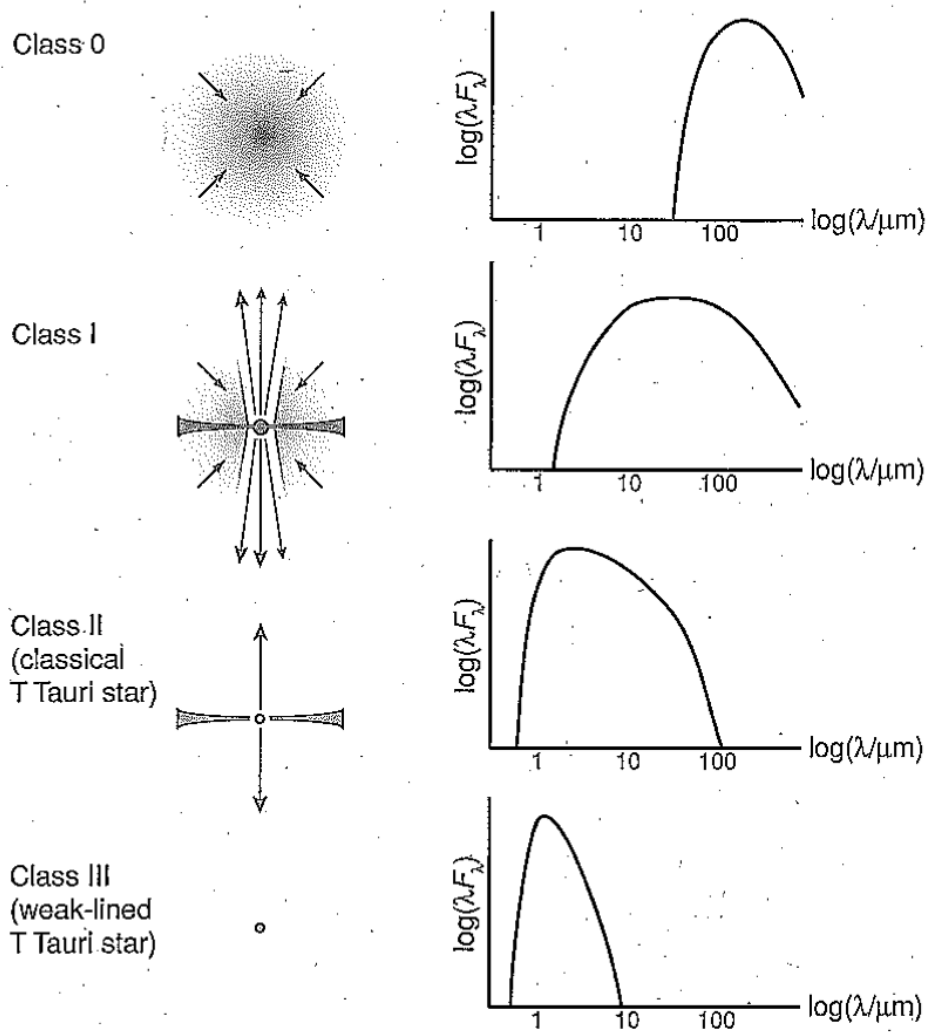


Figure 1.2: Classification of YSOs and their corresponding stellar evolution stage, taken from Figure 2.1 of Armitage (2009).

optically thick gas and dust grains. Sources with $\alpha_{\text{IR}} \geq 0.3$ are classified as Class I (upper panel of Figure 1.1). They consist of YSOs and disks embedded within envelopes, and outflows or jets launched from the vicinity of the central stars are detected. For $-1.6 \leq \alpha_{\text{IR}} < 0.3$, the object is classified as Class II (middle panel of Figure 1.1). In this phase, most of envelopes have been accreted onto the disks, and optical emission from classical T-Tauri stars and IR to mm emission from

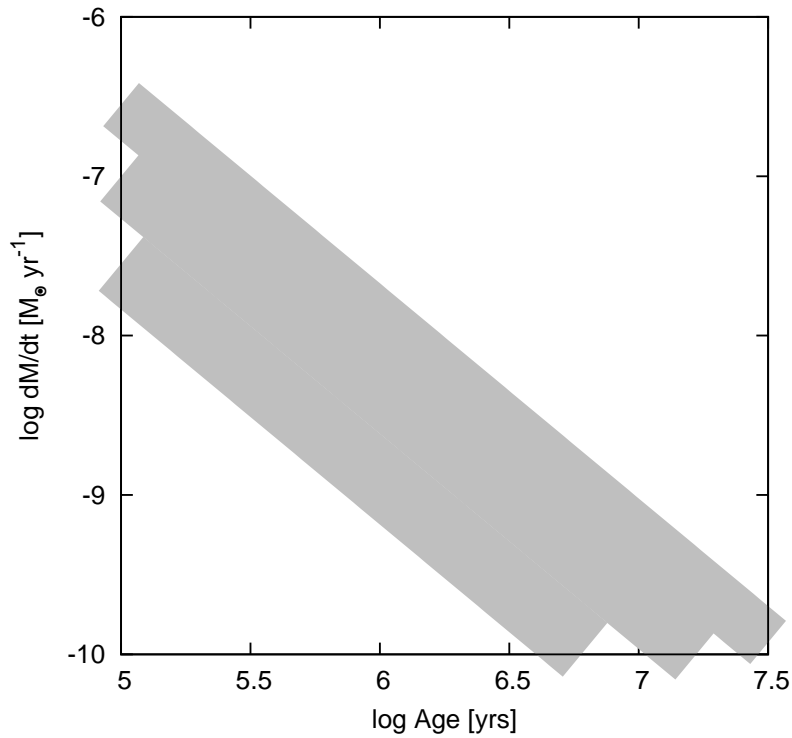


Figure 1.3: A schematic of the time evolution of gas accretion rate, based on Hartmann et al. (1998).

protoplanetary disks are detected. Finally, objects with $\alpha_{\text{IR}} < -1.6$ are classified as Class III (lower panel of Figure 1.1), which are mostly represented by blackbody emission from weak-lined T-Tauri stars that have almost no gas disks. The distinction between classical and weak-lined T-Tauri stars is based on the strength of the $\text{H}\alpha$ emission from the accretion shock at the stellar surface. Classical T-Tauri stars have stronger $\text{H}\alpha$ emission which implies gas accretion from the disks to the central stars. This classification scheme is summarized in Figure 1.2.

The UV excess beyond the expected stellar emission is also attributed to gas accretion from the disk. Based on the calibration of accretion luminosity, estimated from UV excess by Gullbring et al.

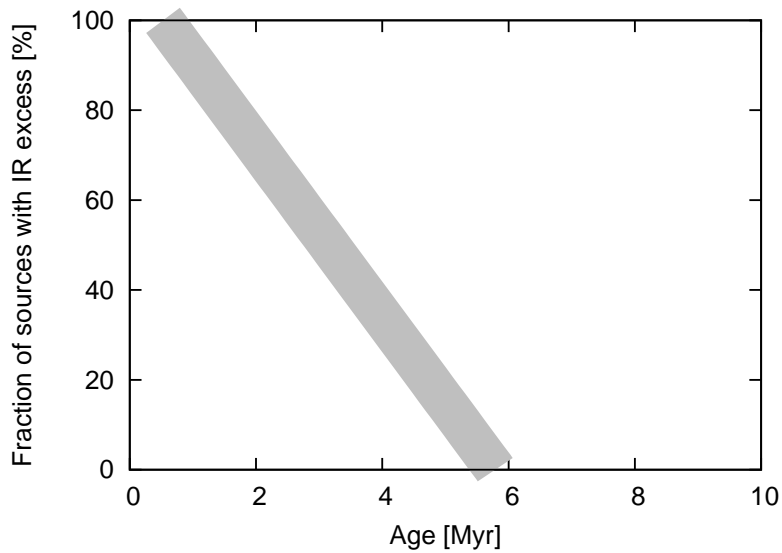


Figure 1.4: Fraction of sources with SEDs showing an IR excess as a function of stellar age based on Haisch et al. (2001).

(1998), a correlation between gas accretion rate and the age of the central star is derived (Hartmann et al., 1998): with increasing age the gas accretion rate decreases (Figure 1.3). On the other hand, IR excess, which signifies the presence of a disk itself, can often be seen in young clusters, but becomes rare after a few Myr (Haisch et al. 2001), as shown in Figure 1.4. This suggests that the lifetime of protoplanetary disks is a few Myr.

1.1.2 Theory of Protoplanetary Disks

As described in Section 1.1.1, gas accretion onto a central star has been observed. For gas orbiting a star to move inward, angular momentum must be transported outward. The typically observed accretion rate ($\sim 10^{-8} M_{\odot} \text{yr}^{-1}$) is far larger than can be explained by molecular viscosity. Thus, as an alternative mechanism, angular momentum

is thought to be removed by turbulent viscosity. This idea comes from the theory of black hole accretion disks, and a non-dimensional α parameter is introduced to express the strength of the turbulence (Shakura and Sunyaev, 1973). α varies between 0 and 1, where 0 means inviscid, and observationally the value in protoplanetary disks is estimated as $\sim 10^{-2}$ (Hartmann et al., 1998). At present, magnetohydrodynamic (MHD) turbulence driven by the magnetorotational instability (MRI) is the most promising mechanism of gas accretion. For the MRI to operate, the disk gas must be sufficiently ionized. However, protoplanetary disks have a very low fraction of charged components. This is because of their low temperature and high density. In order to understand disk evolution, we must investigate MRI activity. The MRI is discussed in more detail in Section 1.3.

In the standard model for the formation of the Solar System, the minimum mass solar nebula (MMSN) model (Hayashi, 1981) is used for the protoplanetary disk. The basic idea of this model is that the total estimated amount of solid materials, consisting of the rocky planets and cores of the gas giants in the Solar System, is distributed in a disk and hydrogen and helium gas are added to reproduce the Solar composition. The surface density and temperature profiles of the MMSN model are

$$\Sigma_{\text{g}} = 1.7 \times 10^3 \left(\frac{r}{1\text{AU}} \right)^{-1.5} \text{ g cm}^{-2}, \quad (1.2)$$

$$T = 280 \left(\frac{r}{1\text{AU}} \right)^{-0.5} \text{ K}, \quad (1.3)$$

where r is the orbital radius. For a disk in hydrostatic equilibrium,

the density of the disk is given by:

$$\rho_{\text{g}}(r, z) \equiv \frac{\Sigma_{\text{n}}}{\sqrt{2\pi}H} \exp\left(-\frac{z^2}{2H^2}\right), \quad (1.4)$$

where z is the distance from the mid-plane and H is the scale height of the disk:

$$H \equiv \frac{c_{\text{s}}}{\Omega_{\text{k}}}, \quad (1.5)$$

where $c_{\text{s}} = \sqrt{\gamma k_{\text{B}}T/\mu m_{\text{H}}}$ is the sound speed, $\Omega_{\text{k}} = \sqrt{GM_*/r^3}$ is the Keplerian frequency, γ is the specific heat ratio, μ is the mean molecular weight of the neutral gas, m_{H} is the mass of a hydrogen atom, G is the gravitational constant, and M_* is the mass of the central star. In this Thesis, we adopt $\mu = 2.34$ and $M_* = M_{\odot}$, and we assume disks are vertically isothermal; γ is set to 1. We use Equation (1.5) for the disk scale height throughout this Thesis, apart from Sections 4.3 and 4.4.

1.2 Circumplanetary Disks as Sites of Satellite Formation

During the formation of gas giant planets, mass is gained from parent protoplanetary disks. Due to the conservation of angular momentum, disks are formed around newly-born planets as the gas flows onto them. These gaseous disks are called circumplanetary disks. Note that circumplanetary disks are different from solid rings like those of Saturn.

The evolution of circumplanetary disks is important not only for the formation of gas giants but also for that of satellites. Regular satellites, whose orbits are almost circular and in the equatorial plane of the host planet, are thought to form in circumplanetary disks.

There have been several theoretical studies on satellite formation in circumplanetary disks (e.g., Canup and Ward, 2002, 2006; Mosqueira and Estrada, 2003; Ogiwara and Ida, 2012; Sasaki et al., 2010). They assumed the structures of circumplanetary disks and discussed satellite formation in the disks. Canup and Ward (2002, 2006) performed N-body simulations and successfully explained the total mass of the Galilean satellites of Jupiter. A remaining problem is how to form circumplanetary disks including their viscous evolution and mass infall from protoplanetary disks. Recently, a new idea for satellite formation based on solid tidal disks has been advocated by Crida and Charnoz (2012). If a sufficient amount of solid material is supplied within the Roche radius, the mass distributions of most regular satellite systems in the Solar system can be well explained. They suggest, however, that

Galilean satellites have formed in a gaseous circumplanetary disk.

Nowadays, thanks to the SEEDS survey by the Subaru telescope (Tamura, 2009) and ALMA, detailed observations of protoplanetary disks are being realized, and more and more researchers are interested in the structures caused by giant planets such as surface density gaps. These structures are interesting in themselves, but also, because the structures of circumplanetary disks are greatly affected by them, they are very important for satellite formation. However, it is still difficult to resolve circumplanetary disks embedded in protoplanetary disks. Thus, at present, we have to rely on theoretical studies when we discuss satellite formation.

Numerical simulations of gas giant formation (e.g. Ayliffe and Bate, 2009; Machida et al., 2010; Uribe et al., 2013) have shown that circumplanetary disks form during the accretion phases of giant planets. Because their studies focused on gas giant formation, the resolution was not sufficient to describe the formation of circumplanetary disks. Tanigawa et al. (2012) performed high-resolution 3D simulation and analyzed the flux of gas infall from a protoplanetary disk to a circumplanetary disk. For the evolution of a circumplanetary disk itself, however, the driving mechanism for the angular momentum transfer of the disk gas is not yet understood. In some circumplanetary disk models, the viscous parameter corresponding to MRI-driven turbulence is adopted, but a more detailed investigation of MRI activity is required.

1.3 Magnetorotational Instability as a Mechanism for Mass Accretion

1.3.1 MHD Turbulence

If a differentially rotating disk is threaded by weak magnetic field and the disk gas is sufficiently ionized to apply the ideal MHD approximation, the disk becomes unstable. This is called the magnetorotational instability (MRI; Balbus and Hawley 1991). Figure 1.5 is a schematic view of the MRI. For simplicity, we focus on two fluid elements which are frozen into the magnetic field. Initially they are in the same orbit (Figures 1.5 (a) and (a')). If they are perturbed as shown in Figure 1.5 (b) and (b'), the fluid element that is moved inward orbits faster and the other element orbits slower; their separation becomes larger. Then, magnetic tension acting like a spring force subtracts angular momentum from the inner fluid element and adds to that of the outer element. Consequently, each element migrates further inward and outward, respectively, and the perturbation grows (Figure 1.5 (c)). This mechanism makes magnetic field and frozen-in gas turbulent (Figure 1.5 (d)). Presently, the MRI is the most promising driving source for gas accretion.

1.3.2 Conditions for MRI Growth

There are two criteria for the MRI to be active (Balbus and Hawley, 1991; Okuzumi and Hirose, 2011; Sano and Miyama, 1999). First, the ionization degree of the disk gas must be sufficiently high to couple to

1.3. Magnetorotational Instability as a Mechanism for Mass Accretion11

the magnetic field. We use the Elsasser number to investigate MRI activity. The Elsasser number is written as

$$\Lambda = \frac{v_{Az}^2}{\eta\Omega_K}, \quad (1.6)$$

where v_{Az} is the z component of the Alfvén velocity, η is the magnetic diffusivity, and Ω_K is the Keplerian frequency. In order for the MRI to operate, Λ must be greater than unity (Sano and Miyama, 1999). A region with $\Lambda < 1$ is called a dead zone. The magnetic diffusivity

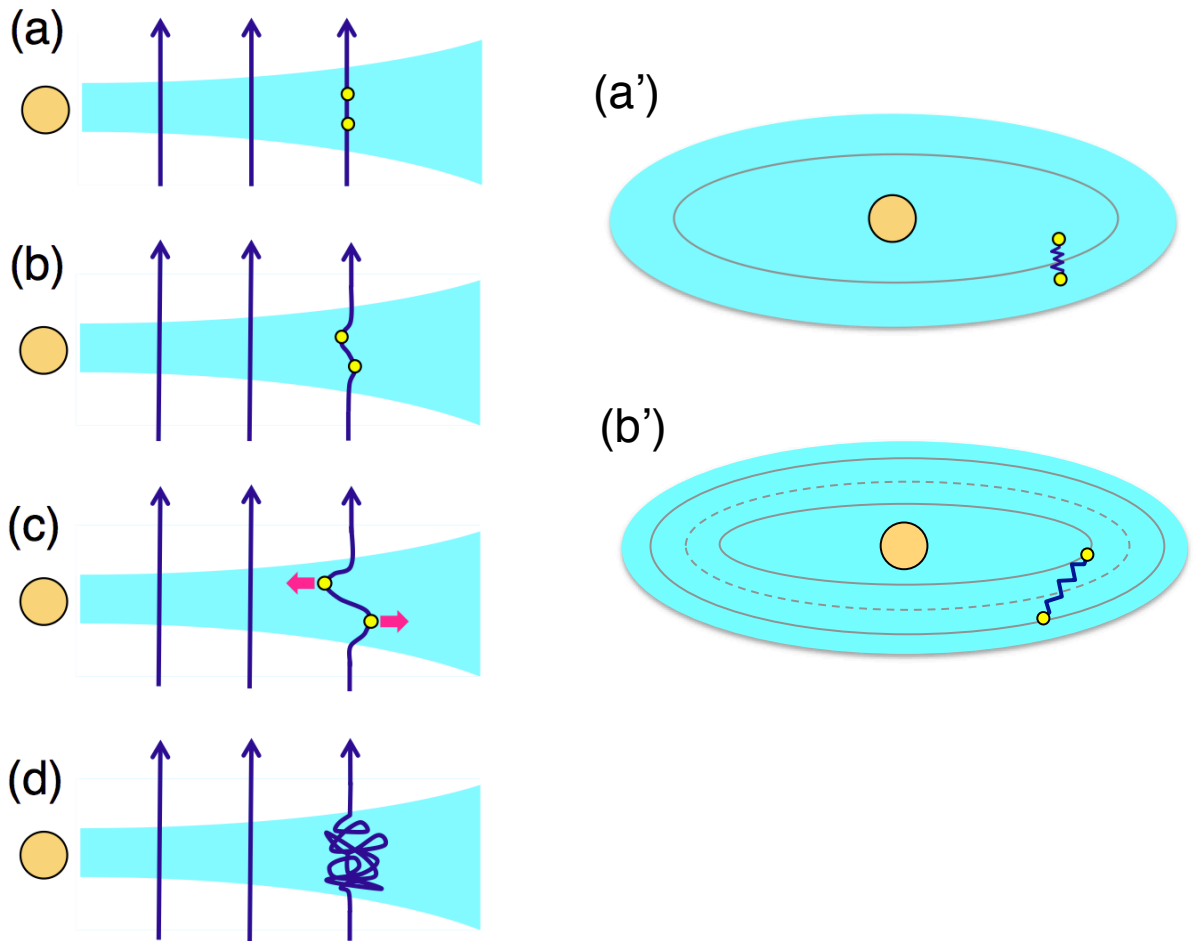


Figure 1.5: Illustration of the MRI. (a)-(d) are edge-on views and (a') and (b') are face-on views of a disk. Arrows represent magnetic field lines and yellow balls represent fluid elements.

1.3. Magnetorotational Instability as a Mechanism for Mass Accretion 12

can be written as (Blaes and Balbus, 1994):

$$\eta = 234 \left(\frac{T}{1\text{K}} \right)^{1/2} x_e^{-1} \text{ cm}^2 \text{ s}^{-1}, \quad (1.7)$$

where $x_e \equiv n_e/n_n$ (the ratio of number densities of electrons and neutral gas molecules) is the ionization degree. If we know the magnetic field strength and gas temperature, we only need the ionization degree to estimate Λ . In this Thesis, we treat the magnetic field strength as a parameter. The higher net field strength means that more magnetic flux threads the disk. Using the z components of gas pressure $P_{\text{gas},z}$ and magnetic pressure $P_{\text{mag},z}$, the z component of plasma beta is given by

$$\beta_z \equiv \frac{P_{\text{gas},z}}{P_{\text{mag},z}} = \frac{\rho_g c_s^2}{B_z^2/8\pi} = \frac{2c_s^2}{v_{Az}^2}, \quad (1.8)$$

where B_z is the net vertical magnetic field, $v_{Az} = B_z/\sqrt{4\pi\rho_g}$ is the z component of the Alfvén velocity, c_s is the sound speed, and ρ_g is gas density. Note that β_z is defined in terms of net magnetic flux. From Equations (1.6)-(1.8), and assuming that B_z is vertically constant, the first condition for the operation of MRI can be written as

$$\Lambda = \frac{2c_s^2 x_e}{234\sqrt{T}\Omega_K\beta_0} \exp\left(\frac{z^2}{2H^2}\right) > 1, \quad (1.9)$$

where β_0 is the mid-plane value of β_z , z is the height from the mid-plane, and H is the disk scale height. Here, we assume the disk is vertically hydrostatic (see Equation (3.6)).

Second, the wavelength of the most unstable mode, $\lambda_{\text{MRI}} = 2\pi v_A/\Omega_K$ should be smaller than the scale height of the disk. This corresponds to the condition for sufficiently weak magnetic field: if the magnetic

1.3. Magnetorotational Instability as a Mechanism for Mass Accretion13

field is too strong, magnetic tension will prevent disk gas from becoming turbulent. We refer to the region with $\lambda_{\text{MRI}} > H$ as the magnetically-dominated atmosphere, in which the MRI is suppressed. From Equation (1.8),

$$\begin{aligned} 2\pi v_A/\Omega_K = \lambda_{\text{MRI}} < H = c_s/\Omega_K \\ \beta_z > 8\pi^2. \end{aligned} \tag{1.10}$$

When the MRI is driven, magnetic field is amplified by turbulence and the magnetically dominated atmosphere encroaches on the active region. Okuzumi and Ormel (2013) quantitatively evaluated this using MHD simulations by Okuzumi and Hirose (2011) and Gressel et al. (2012). At the border separating active from dead zones, B_z^2 is amplified to be roughly 30 times larger than the original value (see Equation (37) of Okuzumi and Ormel, 2013). This implies that the real plasma beta at the border becomes $\beta_z/30$. Thus, when the turbulence is well-developed, the criterion to have MRI becomes $\beta_z/30 > 8\pi^2$, or approximately,

$$\beta_z \gtrsim 2000. \tag{1.11}$$

The onset of the MRI occurs only in the region where the two conditions of Equations (1.9) and (1.10) are both met. The conditions to have well-developed MRI turbulence, given by Equations (1.9) and (1.11), are more severe than those for just the onset of the MRI, . The height-averaged effective viscous stress of MRI can be calculated in terms of the thicknesses of an MRI-active region and a dead zone (Okuzumi and Hirose, 2011).

Chapter 2

Time-dependent Calculation of Ionization Degree

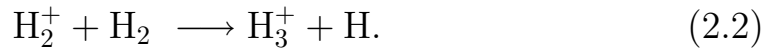
In this chapter, we explain the ionization chemical networks and calculation method of ionization degree in protoplanetary and circumplanetary disks. Some parts of this chapter have previously appeared in Fujii et al. (2011).

2.1 Reactions and Equations

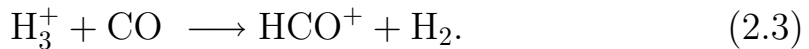
2.1.1 Gas Phase Reactions

Protoplanetary disks mainly consist of hydrogen molecules and contain a small fraction of heavy elements. Because of exposure to ionization sources such as cosmic rays, X-rays, UV, and radiation generated by radionuclides, hydrogen gas in disks is believed to be weakly ionized. Resultant ionized particles produce secondary ions and molecules, which enable further complex reactions. Here, we describe representative reactions.

Ionization of hydrogen molecules leads to the following reactions and produces H_3^+ :



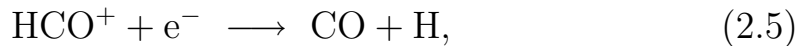
Reactions between H_3^+ and molecules (e.g., CO) lead to heavier molecular ions:



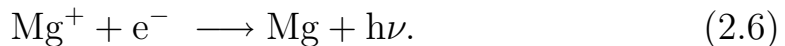
Molecular ions are removed by charge exchange reactions with atomic heavy metals such as Mg:



As long as atomic heavy metals are abundant, dissociative recombination,



is slow, and charge exchange reactions (Equation (2.4)) dominate. A small fraction of metal ions are removed by radiative recombination:



We denote major molecular ions (e.g. H_2^+ , H_3^+ , and HCO^+) by m^+ , and major heavy metal ions (e.g. Mg^+ , Fe^+) by M^+ for simplicity (Ilgner and Nelson, 2006; Oppenheimer and Dalgarno, 1974; Sano et al., 2000).

2.1.2 Grain Surface Reactions

Ions and free electrons propagating in neutral gas are captured on grain surfaces. Since the velocity of electrons is far greater than that

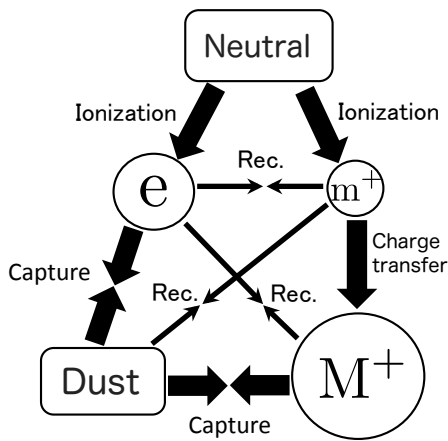


Figure 2.1: Schematic view of simplified reactions. m^+ , M^+ , and e represent molecular ions, heavy metal ions, and electrons, respectively. Neutral gas is ionized by the ionization source, and m^+ transfer their charge to M^+ . Some amount of ions and electrons are captured by dust grains and only a small amount of ions and electrons recombine.

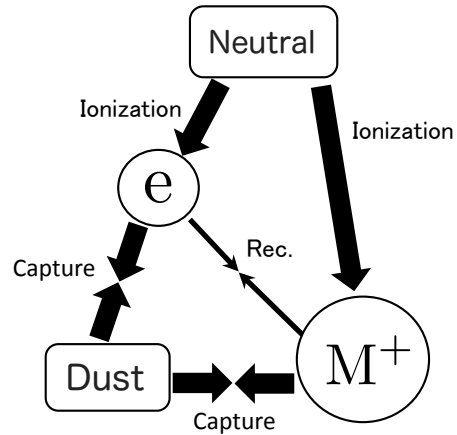


Figure 2.2: m^+ is not shown because charge transfer is so fast that dissociative recombination and capture by dust grains can be neglected; m^+ immediately transfer its charge to M^+ .

of ions, dust grains tend to be negatively charged. In most cases, this reaction proceeds faster than the collisions between dust grains (Okuzumi, 2009). Thus, we neglect mutual collisions of dust grains. In this study, we define the ionization degree as the number density fraction of free electrons to neutral gas. With sufficient dust grains, electrons (and ions) are captured onto dust grains efficiently and the ionization degree is mainly determined by the balance of ionization and the electron capture rate of dust grains. In Figure 2.1, we show a schematic view of reactions in protoplanetary disks.

2.1.3 Basic Equations

Since the number density of neutral gas, n_n , is far greater than that of charged particles, we can assume it does not depend on ionization degree; n_n can be treated as constant. The reaction equations for the chemical network illustrated in Figure 2.1 are the following:

$$\frac{dn_{m^+}}{dt} = \zeta n_n - \alpha_{m^+} n_{m^+} n_e - \beta n_{m^+} n_M - \sum_Z k_{m^+d}(Z) n_d(Z) n_{m^+}, \quad (2.7)$$

$$\frac{dn_{M^+}}{dt} = -\alpha_{M^+} n_{M^+} n_e + \beta n_{m^+} n_M - \sum_Z k_{M^+d}(Z) n_d(Z) n_{M^+}, \quad (2.8)$$

$$\frac{dn_e}{dt} = \zeta n_n - \alpha_{m^+} n_{m^+} n_e - \alpha_{M^+} n_{M^+} n_e - \sum_Z k_{ed}(Z) n_d(Z) n_e, \quad (2.9)$$

$$\begin{aligned} \frac{dn_d(Z)}{dt} = & -k_{m^+d}(Z) n_d(Z) n_{m^+} - k_{M^+d}(Z) n_d(Z) n_{M^+} - k_{ed}(Z) n_d(Z) n_e \\ & + k_{m^+d}(Z-1) n_d(Z-1) n_{m^+} + k_{M^+d}(Z-1) n_d(Z-1) n_{M^+} \\ & + k_{ed}(Z+1) n_d(Z+1) n_e, \end{aligned} \quad (2.10)$$

where n_j is the number density of each particle (m^+ , molecular ions; M^+ , heavy metal ions; M , heavy metal atoms; e , electrons; d , dust grains), Z is the charge of dust grains, ζ is the ionization rate, and α_{m^+} , α_{M^+} , β , and $k_{jd}(Z)$ are the rate coefficients for dissociative recombination, radiative recombination, charge transfer, and capture of gaseous particles by dust grains, respectively. For molecular ions, the timescale of charge transfer is short enough to neglect dissociative recombination and capture onto dust grains. This means that almost all positive charges are transferred to heavy metal ions. From Equation (2.7), we obtain the relation $\beta n_{m^+} n_M \simeq \zeta n_n$. Thus, we can write the

equations more simply as:

$$\frac{dn_{M^+}}{dt} = \zeta n_n - \alpha_{M^+} n_{M^+} n_e - \sum_Z k_{M^+d}(Z) n_d(Z) n_{M^+}, \quad (2.11)$$

$$\frac{dn_e}{dt} = \zeta n_n - \alpha_{M^+} n_{M^+} n_e - \sum_Z k_{ed}(Z) n_d(Z) n_e, \quad (2.12)$$

$$\begin{aligned} \frac{dn_d(Z)}{dt} = & -k_{M^+d}(Z) n_d(Z) n_{M^+} - k_{ed}(Z) n_d(Z) n_e \\ & + k_{M^+d}(Z-1) n_d(Z-1) n_{M^+} \\ & + k_{ed}(Z+1) n_d(Z+1) n_e, \end{aligned} \quad (2.13)$$

In this way, we can treat the reaction equations as if M^+ are formed directly by primary ionization, as shown in Figure 2.2. Note that Equation (2.13) must be solved for dust grains of each charge value Z .

When we treat micron-sized or smaller grains, the number of charge values, $|Z|$, that we have to consider is not so large. On the other hand, when we are interested in several tens of μm to cm-sized grains, the maximum value of $|Z|$ becomes larger and the number of terms and equations increases; the system of equations becomes more complicated. In such cases, numerical calculation of Equations (2.11)–(2.13) is not an easy task. On top of that, the timescales in the system are very different and it is time-consuming to solve the equations explicitly in time. In order to avoid those difficulties, we use Gaussian approximation for the charge distribution of dust grains and a piecewise exact solution method to solve the time evolution; these are explained in Sections 2.2.1 and 2.2.2, respectively.

2.1.4 Ionization Rate

There are various sources of primary ionization such as Galactic cosmic rays, UV and X-rays from the host star, and the decay of short-lived radionuclides. In the vicinity of the host star ($< \sim 0.1$ AU for solar type stars), despite the high density, thermal ionization is the dominant ionization source. Because of its small attenuation length, UV ionization is only effective at the surface of the disk and is not important within the inner layers. Here, we take into account cosmic rays, X-rays, and radionuclides as ionization sources. Denoting the ionization rates due to cosmic rays, stellar X-rays, and radiation from radionuclides as ζ_C , ζ_X , and ζ_R , respectively, the ionization rate at radius r and height z from the disk mid-plane can be written as

$$\zeta(r, z) \simeq \zeta_C + \zeta_X + \zeta_R. \quad (2.14)$$

The cosmic ray ionization rate is given by the following equation

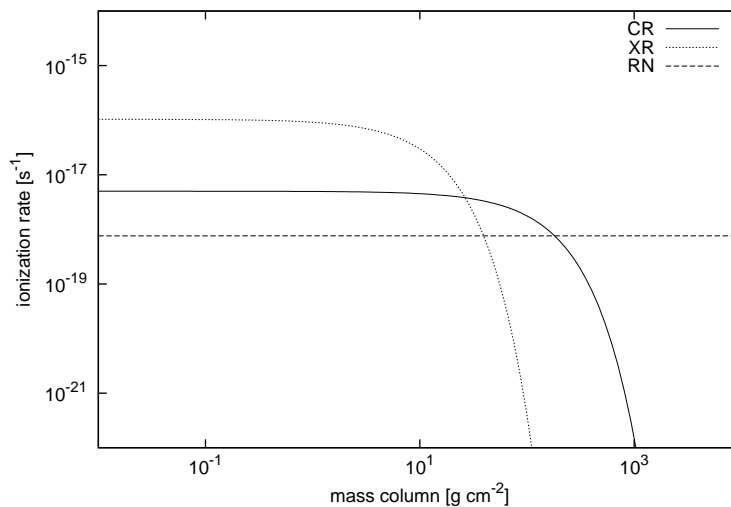


Figure 2.3: Ionization rates due to cosmic rays (solid line), X-rays (dotted line), and radionuclides (dashed line) as a function of the vertical mass column density χ .

(Umebayashi and Nakano, 1981):

$$\zeta_{\text{C}} \simeq \frac{\zeta_{\text{CR}}}{2} \left\{ \exp \left[-\frac{\chi(r, z)}{\chi_{\text{CR}}} \right] + \exp \left[-\frac{\Sigma(r) - \chi(r, z)}{\chi_{\text{CR}}} \right] \right\}, \quad (2.15)$$

where $\zeta_{\text{CR}} \sim 1.0 \times 10^{-17} \text{ s}^{-1}$ is the cosmic ray ionization rate in interstellar space. Cosmic rays may be blown out by stellar winds and the ionization rate may be lower by several orders of magnitude depending on stellar activity (Cleeves et al., 2013). $\chi_{\text{CR}} \sim 96 \text{ g cm}^{-2}$ is the attenuation length of cosmic rays (Umebayashi and Nakano, 1981), and $\Sigma(r)$ is the surface density of a disk at r . The vertical column density from z to the outside of the disk is given by

$$\chi(r, z) = \int_z^{\infty} \rho(r, z) dz. \quad (2.16)$$

The X-ray ionization rate is

$$\zeta_{\text{X}} \simeq \zeta_{\text{XR}} \left(\frac{r_*}{1\text{AU}} \right)^{-2} \left(\frac{L_{\text{XR}}}{2 \times 10^{30} \text{ erg s}^{-1}} \right) \times \left\{ \exp \left[-\frac{\chi(r, z)}{\chi_{\text{XR}}} \right] + \exp \left[-\frac{\Sigma(r) - \chi(r, z)}{\chi_{\text{XR}}} \right] \right\}, \quad (2.17)$$

where r_* is the distance from the host star, $L_{\text{XR}} \sim 2 \times 10^{30} \text{ erg s}^{-1}$ is the X-ray luminosity, and $\zeta_{\text{XR}} \sim 2.6 \times 10^{-15} \text{ s}^{-1}$ and $\chi_{\text{XR}} \sim 8.0 \text{ g cm}^{-2}$ are the fitting parameters (Igea and Glassgold 1999; Turner and Sano 2008). A new study on X-ray ionization rates done by Ercolano and Glassgold (2013) confirmed the calculation of Igea and Glassgold (1999) and also calculated rates using parameters based on current observations. Equation (2.17) only takes into account X-rays scattered by the diffuse gas well above the mid-plane and neglects direct X-ray irradiation (see Turner and Sano, 2008). This may cause the underestimation of ionization degree in the surface layer, but the scattered

X-rays are dominant near the border of the active/dead zones. In addition, when we study on circumplanetary disks, a protoplanetary disk likely blocks direct irradiation and prevents it from reaching a geometrically much thinner circumplanetary disk. We adopt an ionization rate due to radionuclides of $\zeta_{\text{R}} = 7.6 \times 10^{-19} \text{ s}^{-1}$ (Umebayashi and Nakano, 2009). A plot of each ionization source is provided in Fig. 2.1.4.

2.1.5 Rate Coefficients

We use the UMIST database (RATE'06) for the reaction rate of radiative recombination, $\alpha_{\text{M}^+} = 2.80 \times 10^{-12} (T/300)^{-0.86} \text{ cm}^3 \text{ s}^{-1}$, where T is temperature. Because we assume polarization of dust grains is negligible, the capture rate of positive ions (electrons) by dust grains can be written as

$$k_{\text{i(e)d}}(Z) \equiv \langle \sigma_{\text{i(e)d}}(Z) v_{\text{i(e)}} \rangle_v, \quad (2.18)$$

where $\langle \rangle_v$ represents a value averaged by the Maxwellian distribution, and $\sigma_{\text{i(e)d}}$ is the collisional cross section between dust grains and positive ions (electrons):

$$\sigma_{\text{i(e)d}} = \begin{cases} S_{\text{i(e)}} \pi a^2 \left(1 - \frac{2Q_{\text{i(e)}}Q_{\text{d}}}{am_{\text{i(e)}}v^2} \right) & \left(\frac{1}{2}m_{\text{i(e)}}v^2 > \frac{Q_{\text{i(e)}}Q_{\text{d}}}{a} \right) \\ 0 & \left(\frac{1}{2}m_{\text{i(e)}}v^2 < \frac{Q_{\text{i(e)}}Q_{\text{d}}}{a} \right) \end{cases} \quad (2.19)$$

where $Q_{\text{i(e)}}$ is the charge of positive ions (electrons), Q_{d} is that of dust grains, and $S_{\text{i(e)}}$ is the sticking probability. We assume $S_{\text{i(e)}} = 1$ in this work. Using Equation (2.19), Equation (2.18) can be calculated

as:

$$k_{\text{id}}(z) = \begin{cases} \pi a^2 \langle v_{\text{i}} \rangle_v \exp\left(-\frac{q^2 Z}{ak_{\text{B}}T}\right) & (Z > 0) \\ \pi a^2 \langle v_{\text{i}} \rangle_v \left(1 - \frac{q^2 Z}{ak_{\text{B}}T}\right) & (Z < 0) \end{cases} \quad (2.20)$$

$$k_{\text{ed}}(z) = \begin{cases} \pi a^2 \langle v_{\text{e}} \rangle_v \left(1 + \frac{q^2 Z}{ak_{\text{B}}T}\right) & (Z > 0) \\ \pi a^2 \langle v_{\text{e}} \rangle_v \exp\left(\frac{q^2 Z}{ak_{\text{B}}T}\right) & (Z < 0), \end{cases} \quad (2.21)$$

where q is the charge of an electron, a is the radius of the grains, k_{B} is the Boltzmann constant, and $\langle v_{\text{i(e)}} \rangle_v$ is the thermal velocity of an ion (electron):

$$\langle v_{\text{i(e)}} \rangle_v = \sqrt{\frac{8k_{\text{B}}T}{\pi m_{\text{i(e)}}}}. \quad (2.22)$$

As we can see, the dependence on particle species is only the inverse of the square root of mass. Thus, we do not have to pay much attention to specific species as long as we are interested in the ionization degree in a dusty environment.

In this study, we consider compact dust grains with density $\rho_{\text{grain}} = 3 \text{ g cm}^{-3}$. The mass of a dust grain is $m_{\text{grain}} = (4\pi/3)\rho_{\text{grain}}a^3$, and the number density of dust grains is $n_{\text{d}} = \rho_{\text{d}}/m_{\text{grain}} = f_{\text{dg}}\rho_{\text{n}}/m_{\text{grain}}$, where f_{dg} is the dust-to-gas mass ratio:

$$f_{\text{dg}} = \frac{\rho_{\text{d}}}{\rho_{\text{n}}}. \quad (2.23)$$

We take a and f_{dg} as free parameters.

2.2 Fast and Accurate Method for Ionization Degree Calculations

2.2.1 Gaussian Approximation of Charge Distribution of Dust Grains

In the basic equations, the third terms of Equations (2.11) and (2.12) contain a number of Z -dependent terms. This means that the wider the charge distribution we consider, the more reactions we have to solve. Additionally, Equation (2.13) consists of many equations.

Since the charge distribution of dust grains can be approximated by a Gaussian distribution (Okuzumi, 2009), $n_d(Z)$ can be written as

$$n_d(Z) = \frac{N_d}{\sqrt{2\pi\langle\delta Z^2\rangle}} \exp\left[-\frac{(Z - \langle Z \rangle)^2}{2\langle\delta Z^2\rangle}\right], \quad (2.24)$$

where N_d is the total number density of dust grains, defined as

$$N_d \equiv \sum_Z n_d(Z). \quad (2.25)$$

Instead of solving Equation (2.13) for each Z , we calculate the time evolution of the mean charge $\langle Z \rangle$ and the dispersion $\langle\delta Z^2\rangle$ of the charge distribution of dust grains. $\langle Z \rangle$ and $\langle\delta Z^2\rangle$ can be obtained from the following equations:

$$\langle Z \rangle \equiv \frac{1}{N_d} \sum_Z Z n_d(Z) \simeq \frac{1}{N_d} \int_{-\infty}^{\infty} Z n_d(Z) dZ, \quad (2.26)$$

$$\begin{aligned} \langle\delta Z^2\rangle &\equiv \langle Z^2 \rangle - \langle Z \rangle^2 \\ &\simeq \frac{1}{N_d} \int_{-\infty}^{\infty} Z^2 n_d(Z) dZ - \left[\frac{1}{N_d} \int_{-\infty}^{\infty} Z n_d(Z) dZ \right]^2, \end{aligned} \quad (2.27)$$

where $\langle \rangle$ denotes the averaged value weighted by the number density of dust grains, $n_d(Z)$.

We derive the differential equation for $\langle Z \rangle$ by taking the first moment of Equation (2.13):

$$\begin{aligned}
 \sum_Z Z \frac{d}{dt} n_d(Z) &= \sum_Z [k_{M+d}(Z) n_{M^+} n_d(Z) - k_{ed}(Z) n_e n_d(Z)] \\
 &= \left[\sum_Z k_{M+d}(Z) n_d(Z) \right] n_{M^+} - \left[\sum_Z k_{ed}(Z) n_d(Z) \right] n_e \\
 &= \langle k_{M+d} \rangle N_d n_{M^+} - \langle k_{ed} \rangle N_d n_e, \tag{2.28}
 \end{aligned}$$

where $\langle k_{M+d} \rangle$ and $\langle k_{ed} \rangle$ are $n_d(Z)$ weighted averaged rate coefficients.

With Equation (2.28) and

$$\begin{aligned}
 \frac{d}{dt} \langle Z \rangle &= \frac{d}{dt} \left[\frac{1}{N_d} \sum_Z Z n_d(Z) \right] \\
 &= \frac{1}{N_d} \left[\sum_Z Z \frac{d}{dt} n_d(Z) \right], \tag{2.29}
 \end{aligned}$$

we obtain

$$\frac{d \langle Z \rangle}{dt} = \langle k_{M+d} \rangle n_{M^+} - \langle k_{ed} \rangle n_e. \tag{2.30}$$

Next, we take the second moment of Equation (2.13):

$$\begin{aligned}
 \sum_Z Z^2 \frac{d}{dt} n_d(Z) &= \langle k_{M+d} \rangle N_d n_{M^+} + 2 \langle Z k_{M+d} \rangle N_d n_{M^+} \\
 &\quad + \langle k_{ed} \rangle N_d n_e - 2 \langle Z k_{ed} \rangle N_d n_e. \tag{2.31}
 \end{aligned}$$

In a similar way as before, we obtain the following equation:

$$\begin{aligned}
 \frac{d}{dt} \langle Z^2 \rangle &= \langle k_{M+d} \rangle n_{M^+} + 2 \langle Z k_{M+d} \rangle n_{M^+} \\
 &\quad + \langle k_{ed} \rangle n_e - 2 \langle Z k_{ed} \rangle n_e. \tag{2.32}
 \end{aligned}$$

Using this, we can derive the differential equation of $\langle \delta Z^2 \rangle$:

$$\begin{aligned}
 \frac{d\langle \delta Z^2 \rangle}{dt} &= \frac{d\langle Z^2 \rangle}{dt} - \frac{d\langle Z \rangle^2}{dt} \\
 &= \frac{d\langle Z^2 \rangle}{dt} - 2\langle Z \rangle \frac{d\langle Z \rangle}{dt} \\
 &= (\langle k_{M+d} \rangle + 2\langle Z k_{M+d} \rangle - 2\langle Z \rangle \langle k_{M+d} \rangle) n_{M^+} \\
 &\quad + (\langle k_{ed} \rangle - 2\langle Z k_{ed} \rangle + 2\langle Z \rangle \langle k_{ed} \rangle) n_e \\
 &= (\langle k_{M+d} \rangle + 2\langle k_{M+d} \delta Z \rangle) n_{M^+} \\
 &\quad + (\langle k_{ed} \rangle - 2\langle k_{ed} \delta Z \rangle) n_e. \tag{2.33}
 \end{aligned}$$

The full formulae for $\langle k_{M+d} \rangle$, $\langle k_{ed} \rangle$, $\langle k_{M+d} \delta Z \rangle$, and $\langle k_{ed} \delta Z \rangle$ are the following (see Appendix of Fujii et al., 2011):

$$\begin{aligned}
 \langle k_{M+d} \rangle &\simeq \pi a^2 \langle v_{M^+} \rangle_v \left\{ \frac{1}{2} \left(1 - \frac{q^2}{ak_B T} \langle Z \rangle \right) \operatorname{erfc} \left[\frac{\langle Z \rangle}{\sqrt{2\langle \delta Z^2 \rangle}} \right] \right. \\
 &\quad + \frac{q^2}{ak_B T} \sqrt{\frac{\langle \delta Z^2 \rangle}{2\pi}} \exp \left[-\frac{\langle Z \rangle^2}{2\langle \delta Z^2 \rangle} \right] \\
 &\quad + \frac{1}{2} \operatorname{erfc} \left[\sqrt{\frac{\langle \delta Z^2 \rangle}{2}} \frac{q^2}{ak_B T} - \frac{\langle Z \rangle}{\sqrt{2\langle \delta Z^2 \rangle}} \right] \\
 &\quad \left. \times \exp \left[\frac{1}{2} \left(\frac{q^2}{ak_B T} \right)^2 \langle \delta Z^2 \rangle - \left(\frac{q^2}{ak_B T} \right) \langle Z \rangle \right] \right\}, \tag{2.34}
 \end{aligned}$$

$$\langle k_{ed} \rangle \simeq \langle k_{M+d} \rangle |_{\langle Z \rangle \rightarrow -\langle Z \rangle} \tag{2.35}$$

$$\begin{aligned}
 \langle k_{M+d} \delta Z \rangle &\simeq \pi a^2 \langle v_{M^+} \rangle_v \frac{q^2}{2ak_B T} \langle \delta Z^2 \rangle \left(-\operatorname{erfc} \left[\frac{\langle Z \rangle}{\sqrt{2\langle \delta Z^2 \rangle}} \right] \right. \\
 &\quad \left. - \exp \left[-\frac{q^2}{ak_B T} \langle Z \rangle + \frac{1}{2} \left(\frac{q^2}{ak_B T} \right)^2 \langle \delta Z^2 \rangle \right] \right) \\
 &\quad \times \operatorname{erfc} \left[\frac{q^2}{ak_B T} \sqrt{\frac{\langle \delta Z^2 \rangle}{2}} - \frac{\langle Z \rangle}{\sqrt{2\langle \delta Z^2 \rangle}} \right], \tag{2.36}
 \end{aligned}$$

$$\begin{aligned}
 \langle k_{\text{ed}}\delta Z \rangle &\simeq \pi a^2 \langle v_e \rangle_v \frac{q^2}{2ak_{\text{B}}T} \langle \delta Z^2 \rangle \left(\operatorname{erfc} \left[-\frac{\langle Z \rangle}{\sqrt{2\langle \delta Z^2 \rangle}} \right] \right. \\
 &\quad \left. + \exp \left[\frac{q^2}{ak_{\text{B}}T} \langle Z \rangle + \frac{1}{2} \left(\frac{q^2}{ak_{\text{B}}T} \right)^2 \langle \delta Z^2 \rangle \right] \right. \\
 &\quad \left. \times \operatorname{erfc} \left[\frac{q^2}{ak_{\text{B}}T} \sqrt{\frac{\langle \delta Z^2 \rangle}{2}} + \frac{\langle Z \rangle}{\sqrt{2\langle \delta Z^2 \rangle}} \right] \right). \quad (2.37)
 \end{aligned}$$

In this Thesis, we use these formulae unless specially mentioned. When we neglect positively charged grains, these formulae can be approximated as

$$\langle k_{\text{M+d}} \rangle \simeq \pi a^2 \langle v_{\text{M}^+} \rangle_v \left(1 - \frac{q^2}{ak_{\text{B}}T} \langle Z \rangle \right), \quad (2.38)$$

$$\langle k_{\text{ed}} \rangle \simeq \pi a^2 \langle v_e \rangle_v \exp \left[\frac{1}{2} \left(\frac{q^2}{ak_{\text{B}}T} \right)^2 \langle \delta Z^2 \rangle + \left(\frac{q^2}{ak_{\text{B}}T} \right) \langle Z \rangle \right], \quad (2.39)$$

$$\langle k_{\text{M+d}}\delta Z \rangle \simeq -\pi a^2 \langle v_{\text{M}^+} \rangle_v \frac{q^2}{ak_{\text{B}}T} \langle \delta Z^2 \rangle, \quad (2.40)$$

$$\begin{aligned}
 \langle k_{\text{ed}}\delta Z \rangle &\simeq \pi a^2 \langle v_e \rangle_v \frac{q^2}{ak_{\text{B}}T} \langle \delta Z^2 \rangle \\
 &\quad \times \exp \left[\frac{q^2}{ak_{\text{B}}T} \langle Z \rangle + \frac{1}{2} \left(\frac{q^2}{ak_{\text{B}}T} \right)^2 \langle \delta Z^2 \rangle \right]. \quad (2.41)
 \end{aligned}$$

This approximation is valid when the grain size is not very small (Okuzumi, 2009). By using Gaussian approximation, the number of equations can be dramatically reduced.

2.2.2 Piecewise Exact Solution Method

The equations we have to solve are as follows:

$$\frac{dn_{M^+}}{dt} = \zeta n_n - \alpha_{M^+} n_{M^+} n_e - \langle k_{M^+d} \rangle N_d n_{M^+}, \quad (2.42)$$

$$\frac{dn_e}{dt} = \zeta n_n - \alpha_{M^+} n_{M^+} n_e - \langle k_{ed} \rangle N_d n_e, \quad (2.43)$$

$$\frac{d\langle Z \rangle}{dt} = \langle k_{M^+d} \rangle n_{M^+} - \langle k_{ed} \rangle n_e, \quad (2.44)$$

$$\begin{aligned} \frac{d\langle \delta Z^2 \rangle}{dt} &= (\langle k_{M^+d} \rangle + 2\langle k_{M^+d} \delta Z \rangle) n_{M^+} \\ &\quad + (\langle k_{ed} \rangle - 2\langle k_{ed} \delta Z \rangle) n_e. \end{aligned} \quad (2.45)$$

We solve our equations partially using a piecewise exact solution method (Inoue and Inutsuka, 2008). This method enables us to solve with large time steps.

First, we split our equations and solve analytically. The solution of

$$\frac{dn_{M^+}}{dt} = \zeta n_n - \langle k_{M^+d} \rangle N_d n_{M^+}, \quad (2.46)$$

is

$$\begin{aligned} n_{M^+}(t + \Delta t) &= \left(n_{M^+}(t) - \frac{\zeta n_n}{\langle k_{M^+d} \rangle N_d} \right) e^{-\langle k_{M^+d} \rangle N_d \Delta t} \\ &\quad + \frac{\zeta n_n}{\langle k_{M^+d} \rangle N_d}, \end{aligned} \quad (2.47)$$

where Δt is the time step of time integration, and the solution of

$$\frac{dn_e}{dt} = \zeta n_n - \langle k_{ed} \rangle N_d n_e \quad (2.48)$$

is

$$n_e(t + \Delta t) = \left(n_e(t) - \frac{\zeta n_n}{\langle k_{ed} \rangle N_d} \right) e^{-\langle k_{ed} \rangle N_d \Delta t} + \frac{\zeta n_n}{\langle k_{ed} \rangle N_d}. \quad (2.49)$$

We treat rate coefficients such as $\langle k_{jd} \rangle$ as constants during a single step. From Equations (2.42) – (2.44),

$$\begin{aligned} \frac{dn_e}{dt} - \frac{dn_{M^+}}{dt} &= \langle k_{M^+d} \rangle n_{M^+} N_d - \langle k_{ed} \rangle n_e N_d \\ &= N_d \frac{d\langle Z \rangle}{dt}, \end{aligned} \quad (2.50)$$

and with charge conservation,

$$N_d \langle Z \rangle(t) + n_{M^+}(t) - n_e(t) = \text{constant} = 0, \quad (2.51)$$

$$\begin{aligned} \langle Z \rangle(t + \Delta t) &= \langle Z \rangle(t) + \frac{n_e(t + \Delta t) - n_{M^+}(t + \Delta t)}{N_d} \\ &\quad - \frac{n_e(t) - n_{M^+}(t)}{N_d}. \end{aligned} \quad (2.52)$$

We use these solutions as initial conditions for the time integration of the remaining complex equation and terms of the slow reaction:

$$\begin{aligned} \frac{d\langle \delta Z^2 \rangle}{dt} &= (\langle k_{M^+d} \rangle + 2\langle k_{M^+d} \delta Z \rangle) n_{M^+} \\ &\quad + (\langle k_{ed} \rangle - 2\langle k_{ed} \delta Z \rangle) n_e \end{aligned} \quad (2.53)$$

$$\frac{dn_{M^+}}{dt} = -\alpha_{M^+} n_{M^+} n_e \quad (2.54)$$

$$\frac{dn_e}{dt} = -\alpha_{M^+} n_{M^+} n_e. \quad (2.55)$$

In conclusion, the equations to be solved numerically are Equations (2.47), (2.49), (2.52), and (2.53)-(2.55).

2.3 Test Calculations

In order to confirm the accuracy of our calculation method, we compare the result with the direct calculation of the original equations (2.11), (2.12), and (2.13). We assume the disk is hydrostatic and vertically isothermal, and adopt a typical surface density and temperature at 1 AU of 1700 g cm^{-2} and 280 K (Hayashi, 1981). The number density of the neutral gas and the ionization rate at the mid-plane are $n_n = 4.22 \times 10^{14} \text{ cm}^{-3}$ and $\zeta = 7.6 \times 10^{-19} \text{ s}^{-1}$, respectively. We choose a dust-to-gas mass ratio of $f_{\text{dg}} = 0.01$ and a dust radius of $0.1 \text{ }\mu\text{m}$. For solving the original set of equations, we consider grain charge variation of $-4 < Z < 4$, and set the initial conditions to be $n_{\text{M}^+} = 0$, $n_e = 0$, $n_d(0) = 1.11 \times 10^3 \text{ cm}^{-3}$, and $n_d(Z \neq 0) = 0$. For our speed-up method, we start the calculation with the initial conditions of $x_{\text{M}^+} = x_e = \langle Z \rangle = \langle \delta Z^2 \rangle = 0$. Figure 2.4 shows the result of the comparison. We can see that the results of the direct calculation and our method agree very well. With this setup, our method can integrate the equations with $\sim 10^5$ times longer time steps than the explicit time integration of the original equations.

The ionization degree immediately approaches equilibrium, but it takes about 10^7 s to be perfectly in equilibrium. This is the timescale for dust grains to collide with charged particles (Okuzumi, 2009). This timescale is written as

$$t^{-1} \simeq \frac{\zeta n_n}{n_d} \text{ [s}^{-1}\text{]}. \quad (2.56)$$

The number density of electrons is small because electrons travel faster

than ions and are more likely to be captured by dust grains. Thus, dust grains charge negatively. The total charge of positive ions is balanced by that of dust grains, and charge neutrality is satisfied.

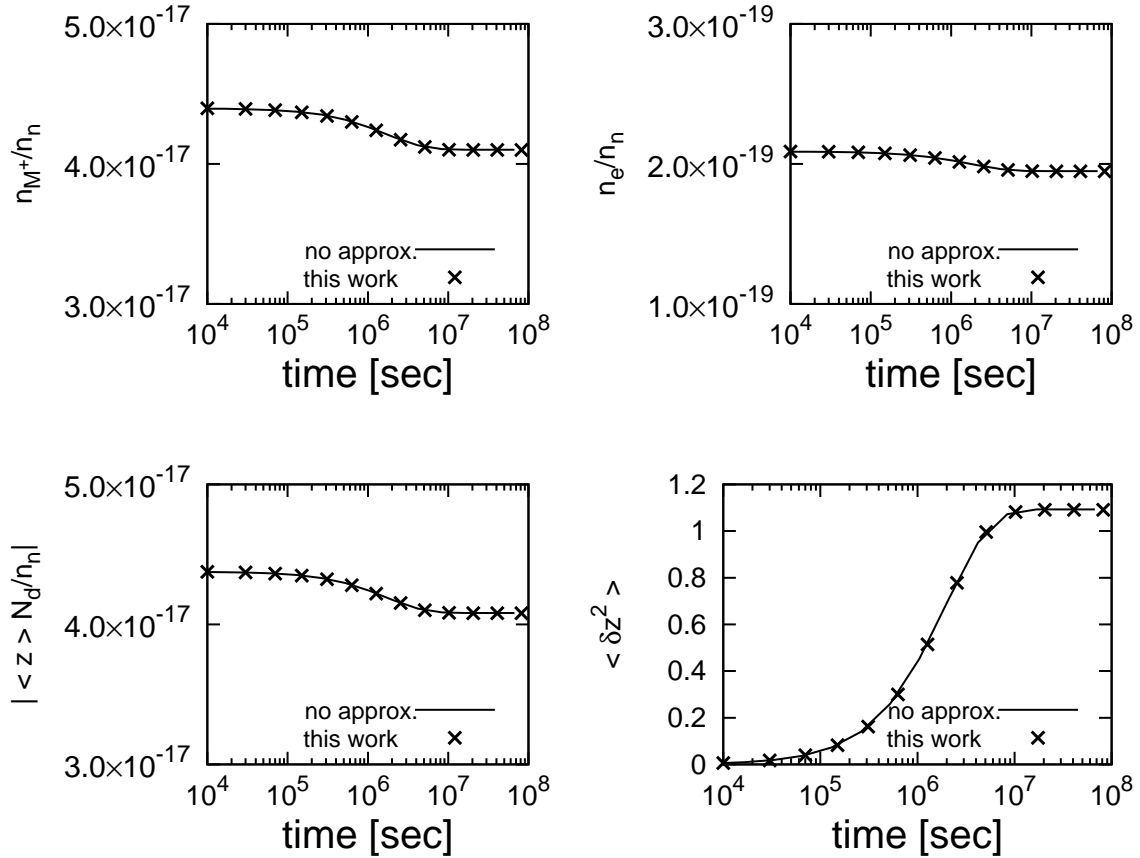


Figure 2.4: The top-left panel is the number density of heavy metal ions, the top-right panel is that of free electrons, and both are normalized by the number density of neutral gas. The bottom-left panel is the absolute value of the product of averaged dust charge and the total abundance of dust grains and shows the absolute value of the total charge held by dust grains. The bottom-right panel is the dispersion of the dust charge distribution. Lines show the results of the basic equations, and crosses show the results of our calculation with two kinds of speed-up method. These panels show that the Gaussian distribution approximation and a piecewise exact solution method are successful.

Chapter 3

Viability of the Magnetorotational Instability in Circumplanetary Disks

In this Chapter, MRI activity, as a possible angular-momentum transfer mechanism, in circumplanetary disks is discussed both in a standard model of satellite forming disk and a model based on recent numerical simulation results. Some parts of this chapter have previously appeared in Fujii et al. (2011) and Fujii et al. (2014b).

3.1 Ionization Degree in Circumplanetary Disks

Since circumplanetary disks are thought to be the formation sites of regular satellites (e.g., Canup and Ward 2002; Canup and Ward 2002; Sasaki et al. 2010), an understanding of their evolution is very important. Although the ionization degree is one of the most important factors for disk evolution in the context of the MRI, it has not been widely discussed in the literature. Takata and Stevenson (1996) calcu-

lated the ionization degree with a focus on the despin mechanism for proto-giant planets. However, the disk surface densities they considered were much higher than those of disk models for satellite formation, and they did not discuss the MRI. In this Section, we calculate the ionization degree in circumplanetary disks in order to investigate whether the MRI can operate there.

3.1.1 Properties of Circumplanetary Disks

To model a circumplanetary disks, we consider an actively-supplied gaseous accretion disk, also called the gas-starved disk model (Canup and Ward 2002, 2006; see Appendix of Sasaki et al. 2010). The radial profile of the temperature is given as

$$T_{\text{cir}} \simeq 160 \left(\frac{M_{\text{p}}}{M_{\text{J}}} \right)^{1/2} \left(\frac{r}{20R_{\text{J}}} \right)^{-3/4} \text{ K}, \quad (3.1)$$

where M_{p} is the mass of the central planet, M_{J} is that of Jupiter, r is the orbital radius from the central planet, and R_{J} is the radius of Jupiter. We adopt 5×10^6 yr for the timescale to accrete gas as heavy as the central planet, and assume the disk is vertically isothermal. With viscosity coefficient $\alpha = 5 \times 10^{-3}$, the surface density is given as

$$\Sigma_{\text{cir}} \simeq 100 \left(\frac{M_{\text{p}}}{M_{\text{J}}} \right) \left(\frac{r}{20R_{\text{J}}} \right)^{-3/4} \text{ g cm}^{-2}. \quad (3.2)$$

In Section 3.1, we assume $M_{\text{p}} = M_{\text{J}}$ and parameterize the vertical component of the plasma beta at mid-plane, β_0 , the radius of dust grains a , and the dust-to-gas mass ratio $f_{\text{dg}} = \rho_{\text{d}}/\rho_{\text{g}}$.

3.1.2 Limitations of Standard Model

We use our method that is described in Chapter 2 for ionization calculation in the standard model, the gas-starved disk. The abundance of radionuclides has greater uncertainty than in protoplanetary disks, but since the ionization by cosmic rays is efficient in this surface density regime, radionuclides do not affect the ionization degree very much. Also, circumplanetary disks are located at the orbital radius of gas giant planets which is rather far from the star, and therefore, X-ray ionization is less effective. Furthermore, the scale height of circumplanetary disks is far smaller than that of protoplanetary disks. Thus, geometrically, X-rays are less likely to reach the circumplanetary disks. In this section, we consider only cosmic rays as ionization sources.

Figure 3.1 shows the size of the dead zone, the region whose Elsasser number (Equation 1.6 or 1.9) is smaller than unity, for the model of $\beta_0 = 100$, $a = 10^{-3}$ cm, and $f_{\text{dg}} = 10^{-2}$. Note that the scale height at $r = 20R_{\text{J}}$ is about $1.6R_{\text{J}}$.

Hereafter, as a matter of convenience for the discussion of the MRI, we express the vertical distance in units of H . In Figure 3.2, we present the f_{dg} dependence of the size of the dead zones. One can see that dead zones cover large areas for all magnetic field strengths, and the presence of dust grains enlarges the dead zones. Especially in the case $\beta_0 = 10^6$, corresponding to weak magnetic field, the dead zone covers almost the entire region of the disk. Figure 3.3 shows the results for the various models of β_0 and a . The dust-to-gas mass ratio is kept the same as the inter stellar space in these plots. Larger grain size leads

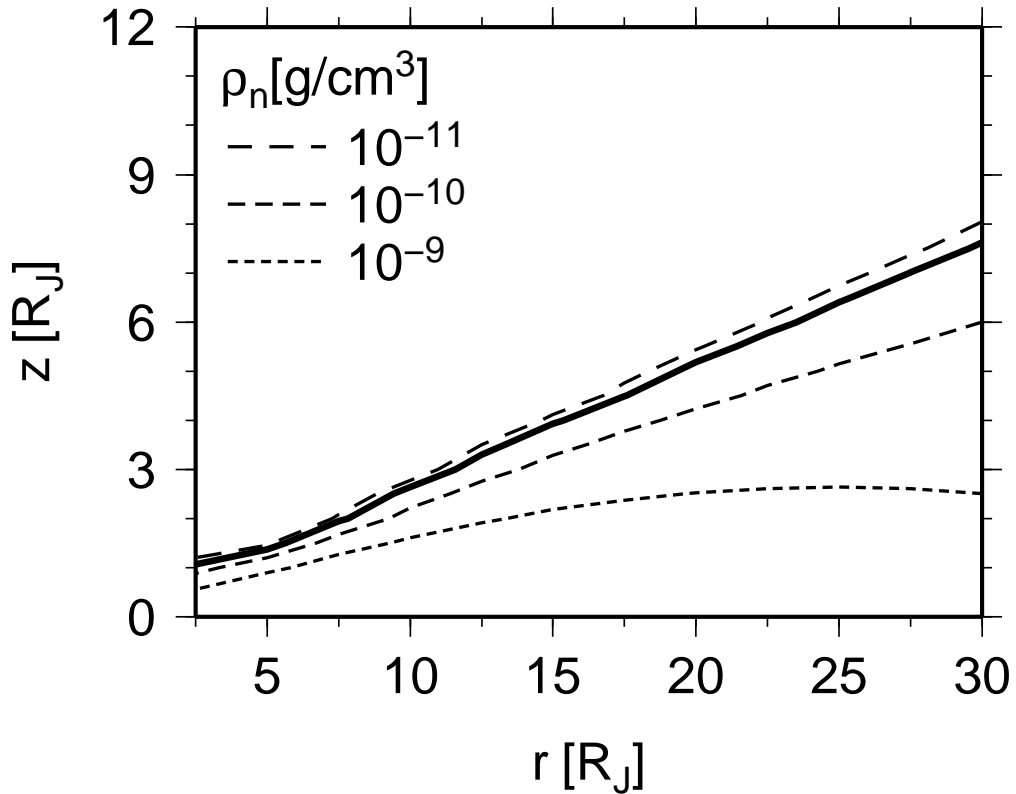


Figure 3.1: Size of the MRI-inactive region with $\beta_0 = 100$, $a = 10^{-3}\text{cm}$, and $f_{\text{dg}} = 10^{-2}$. The horizontal axis is orbital radius from the central planet and vertical axis is the distance from the mid-plane. The region under the thick line is the MRI-inactive region, dead zone. The density of the neutral gas is also shown as contour lines.

to higher ionization degree because the total surface density of dust grains becomes smaller under the constant dust-to-gas mass ratio.

Previous studies on circumplanetary disks or satellite formation mainly focused on MRI-active disks for theoretical reasons, however it turned out that circumplanetary disks are largely covered by the dead zones when we adopt a standard model. This suggests that close investigation in other disk models is needed.

We also performed calculations for the models of $f_{\text{dg}} = 10, 100$. The results for the models of $a = 1\text{mm}$ with various values of f_{dg} is

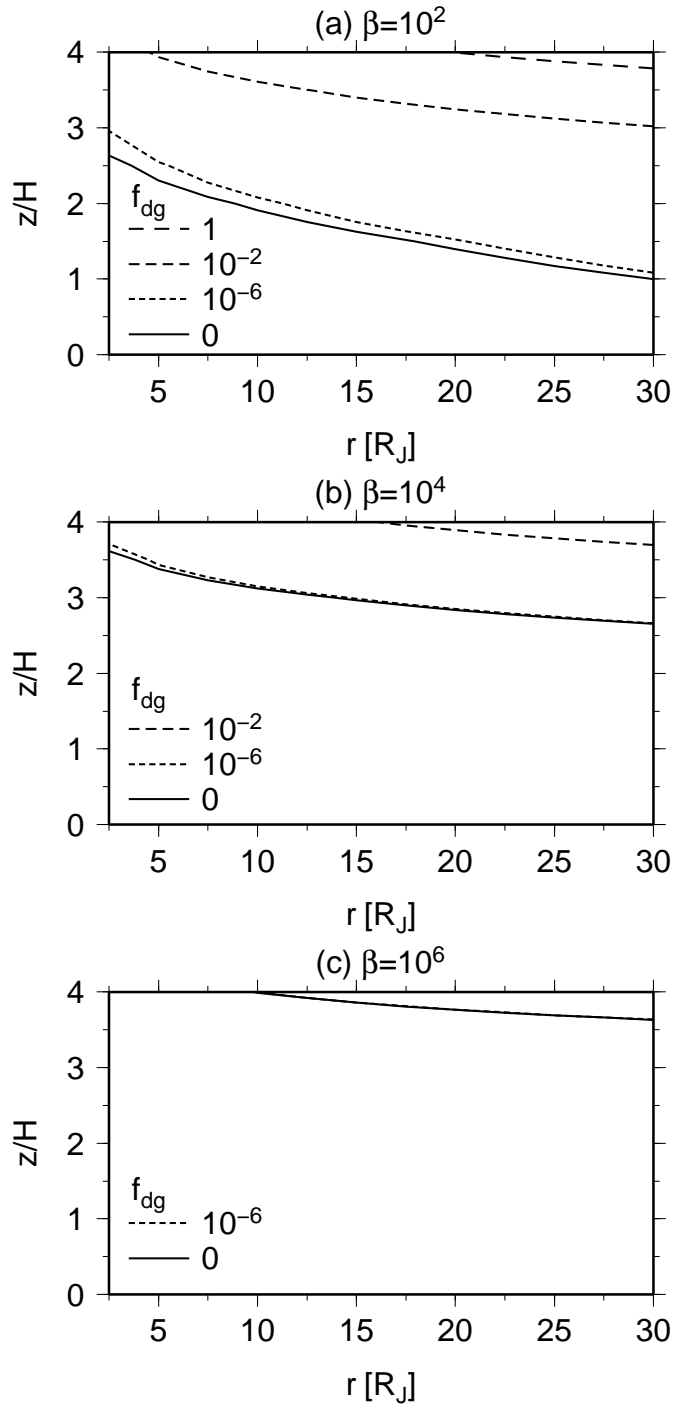


Figure 3.2: Boundaries of the MRI-inactive region in circumplanetary disks: (a) $\beta_0 = 10^2$, (b) $\beta_0 = 10^4$, and (c) $\beta_0 = 10^6$. The horizontal axes denote the orbital radius from the central planet, and the vertical axes are the distance from the mid-plane normalized by the scale height of the corresponding radius. The radius of dust grains is $a = 10\mu\text{m}$. Contour lines show the boundaries of the MRI-active regions and the dead zones for each model of the dust-to-gas mass ratio f_{dg} .

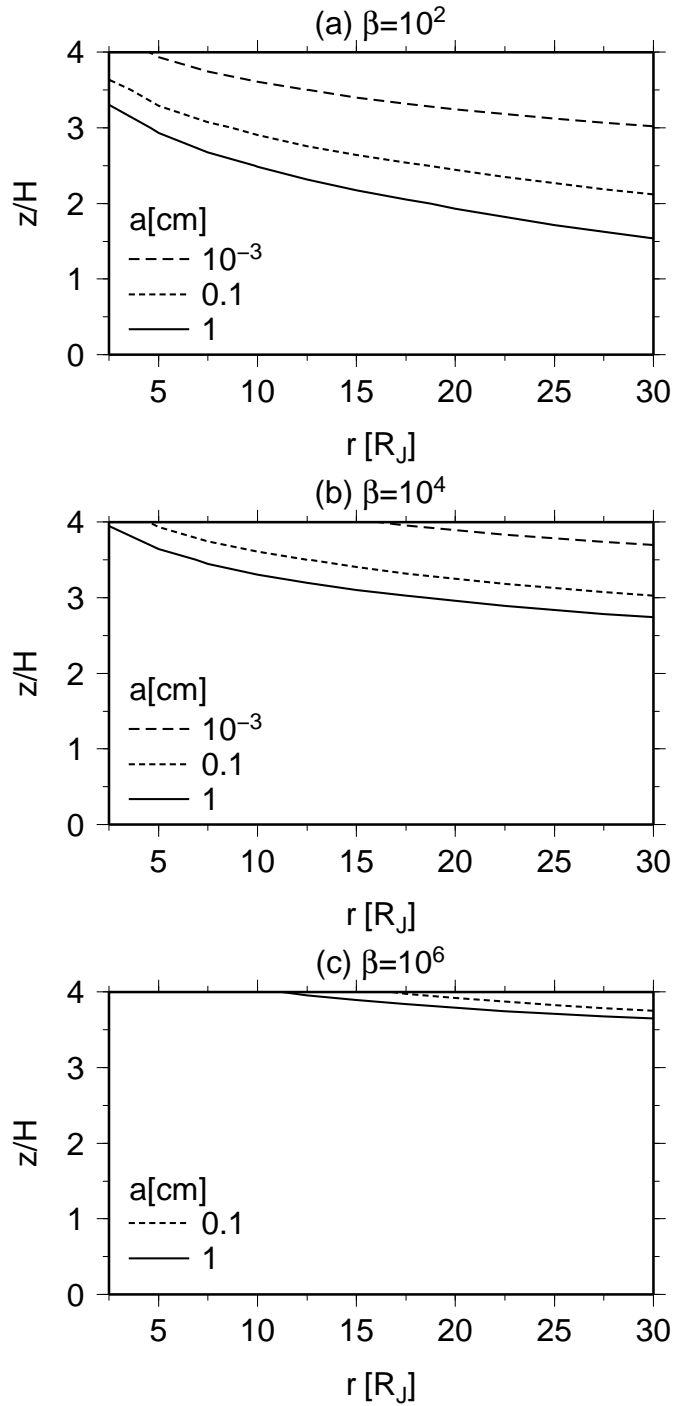


Figure 3.3: Same as 3.2, but the dust-to-gas mass ratio is fixed to $f_{\text{dg}} = 10^{-2}$, and we consider the dust grain radius a as a parameter.

| f_{dg} | n_e/n_n | $\langle Z \rangle$ | $\langle \delta Z^2 \rangle$ |
|-----------------|------------------------|---------------------|------------------------------|
| 100 | 4.83×10^{-19} | -2.26×10^3 | 6.46×10^3 |
| 10 | 8.97×10^{-17} | -3.70×10^4 | 9.56×10^3 |
| 1 | 1.75×10^{-15} | -4.49×10^4 | 9.83×10^3 |
| 10^{-2} | 1.76×10^{-13} | -4.50×10^4 | 9.83×10^3 |

Table 3.1: Ionization degree n_e/n_n , the mean charge of dust grains (normalized by the charge of an electron) $\langle Z \rangle$, and the dispersion of the charge distribution of dust grains $\langle \delta Z^2 \rangle$ at $r = 15R_J$, $z = 0$. The radius of dust grains is fixed at $a = 1\text{mm}$ and we take the dust to gas mass ratio f_{dg} as a parameter. Our method is effective when the charge distribution of dust grains is very wide, because it can reduce the number of exations to solve.

summarized in Table 3.1. When the grain size is small (e.g. $0.1 \mu\text{m}$), the mean charge and dispersion of the charge distribution of dust grains are also small, but when the grain size is relatively large (e.g. 1mm), those values become significantly large. Our method explained in Chapter 2 is highly effective in such cases.

3.2 Alternative Disk Models

3.2.1 Surface Density Evolution

In order to construct a realistic model of circumplanetary disks, the way of mass supply is important. Tanigawa et al. (2012) performed 3D high-resolution simulations of mass inflow from a protoplanetary disk to a circumplanetary disk. Through detailed analysis of the results, they obtained the mass infall rate onto a circumplanetary disk. We use their result to determine the surface density of circumplanetary disks. We solve a diffusion equation of a disk with mass infall from outside of the disk. We adopt the α model of Shakura and Sunyaev (1973). The diffusion equation of a Keplerian disk with a source term f is

$$\frac{\partial \Sigma}{\partial t} = \frac{1}{r} \frac{\partial}{\partial r} \left[3r^{1/2} \frac{\partial}{\partial r} \left(r^{1/2} \nu \Sigma \right) \right] + f, \quad (3.3)$$

where r is radius, ν is kinematic viscosity coefficient. For f , we use the result of Tanigawa et al. (2012).

They measured physical properties of infalling gas just before it falls onto a circumplanetary disk. Since the infall is supersonic, its properties do not depend on the architecture of the circumplanetary disk at the downstream and thus the physical properties are less uncertain. The mass and specific angular momentum of infalling gas they measured are $f_s \propto r^0$ and $h_s \propto r^1$, respectively. Thus, the effective mass flux is $f \propto r^{-1}$. This is because the angular momentum at the radius where gas falls onto a circumplanetary disk is smaller than that of Keplerian rotation at the same radius and the radial dependence of

angular momentum is smaller than the Keplerian profile: gas will move inward until it rotates at the Keplerian velocity if it conserves specific angular momentum, and the mass tends to be center-concentrated.

We assume that the central planet is located in the orbit of 5.2AU in a protoplanetary disk of a solar mass star. If we adopt the minimum mass solar nebula model (Hayashi, 1981), the surface density and the sound speed of the protoplanetary disk at 5.2AU are $\Sigma_{\text{P}} = 143 \text{ g cm}^{-2}$ and $c_{\text{sP}} = 6.58 \times 10^4 \text{ cm s}^{-1}$. We assume the central planet has 0.4 Jupiter masses. Using these values, we obtain the mass infall rate as

$$f = 1.3 \times 10^{-3} \epsilon \left(\frac{\Sigma_{\text{P}}}{143 \text{ g cm}^{-2}} \right) \left(\frac{r}{R_{\text{J}}} \right)^{-1} \text{ g cm}^{-2} \text{ s}^{-1}, \quad (3.4)$$

where ϵ is the dissipation factor of protoplanetary disk gas, and R_{J} is a Jupiter radius. We use this formula only within $r \sim 20R_{\text{J}}$ and set $f = 0$ at larger radii, because the power law index of the mass infall rate drops outside $\sim 20R_{\text{J}}$ (Tanigawa et al., 2012). When a (proto-)planet grows to some extent, a gap will open in the disk, and ϵ represents such situations. Since the viscous timescale of a circumplanetary disk is sufficiently smaller than that of a protoplanetary disk, we treat ϵ as a constant value. $\epsilon = 1$ corresponds to an initial condition.

We employ the standard α prescription,

$$\nu = \alpha c_{\text{s}} H = \alpha \frac{c_{\text{s}}^2}{\Omega_{\text{K}}}, \quad (3.5)$$

and $\alpha = 0.05$ to calculate choose ν . We solve Equation (3.3) numerically with the initial condition $\Sigma(t = 0) = 0$, time step $\Delta t = 1.0 \times 10^3 \text{ s}$, and cell width $\Delta r = 0.85R_{\text{J}}$. The calculation range is $0.85R_{\text{J}} \leq r \leq 210R_{\text{J}}$. The boundary conditions are $\nu = 0$ at the inner

boundary and $\Sigma = 0$ at the outer boundary. We assume that the disk is vertically hydrostatic and give the gas density profile as

$$\rho_g(r, z) \equiv \frac{\Sigma}{\sqrt{2\pi}H} \exp\left(-\frac{z^2}{2H^2}\right), \quad (3.6)$$

and the temperature of the disk gas as $T = 123\text{K}$.

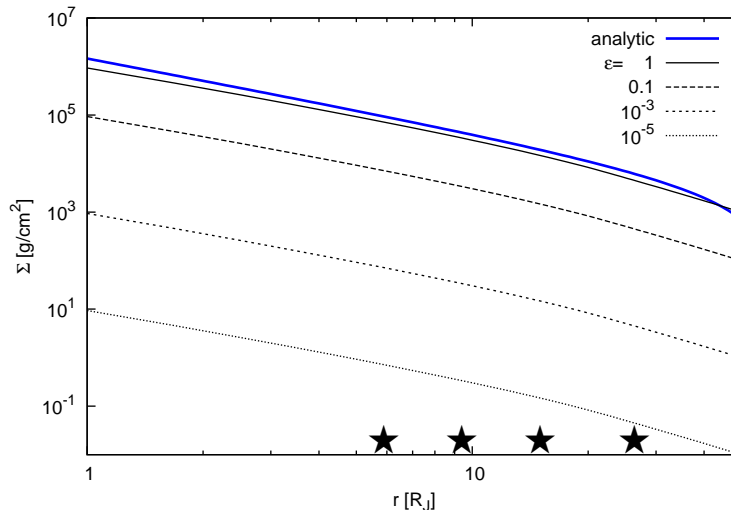


Figure 3.4: Surface densities of circumplanetary disks with $\alpha = 0.05$. Each line shows the result of a different value of ϵ , the dissipation factor of protoplanetary disk gas. The blue thick line is the analytic solution (see 3.2.2). Black stars indicate the orbits of Galilean moons.

In Fig. 3.4, we plot the surface density in steady states with $\epsilon = 1, 0.1, 10^{-3}, 10^{-5}$. Note that the critical surface density to be gravitationally unstable is several orders of magnitude larger than the $\epsilon = 1$ case (the solid black line).

3.2.2 Analytic Treatment

We can analytically solve Equation (3.3) using Equation (3.5) when α is a constant value and the disk is steady and isothermal (cf. Appendix

of Canup and Ward, 2002). The source term f is proportional to r^{-1} so we write $f \equiv A/r$, where A is a constant. If we write $\nu = \nu_0 (r/r_0)^{\frac{3}{2}}$, where ν_0 is the kinematic viscosity coefficient for $r = r_0$, the solution of

$$0 = \frac{1}{r} \frac{\partial}{\partial r} \left[3r^{\frac{1}{2}} \frac{\partial}{\partial r} \left(r^{\frac{1}{2}} \nu \Sigma \right) \right] + \frac{A}{r}, \quad (3.7)$$

is

$$\Sigma = \frac{r_0^{\frac{3}{2}}}{\nu_0} \left(-\frac{2}{9} A r^{-\frac{1}{2}} + C_1 r^{-\frac{3}{2}} + C_2 r^{-2} \right), \quad (3.8)$$

where C_1 and C_2 are constants. C_2 should be zero since the torque $r^{1/2} \nu \Sigma$ vanishes at $r = 0$. The mass accretion rate of a steady state at the inner boundary, \dot{M}_p , is

$$\begin{aligned} \dot{M}_p &\simeq -2\pi r_{\text{in}} \Sigma v_r \\ &= 6\pi r_{\text{in}}^{\frac{1}{2}} \frac{\partial}{\partial r} \left(r_{\text{in}}^{\frac{1}{2}} \nu \Sigma \right) \\ &= 3\pi C_1, \end{aligned} \quad (3.9)$$

where r_{in} is the radius of the inner boundary and v_r is the radial velocity of the gas. We consider the second term on the right hand side of Equation (3.8) to be dominant. Since the inner edge of a disk is far smaller than the outer edge of the region with infall, r_b , the total infall rate onto the circumplanetary disk \dot{M}_s can be approximated as

$$\begin{aligned} \dot{M}_s &= 2\pi \int_{r_{\text{in}}}^{r_b} f r dr \\ &\simeq 2\pi A r_b. \end{aligned} \quad (3.10)$$

In a steady state, the mass falling onto the central planet should be equal to the inflow from the surrounding protoplanetary disk, thus

| | |
|---|--------------------------|
| gas dissipation factor ϵ | 1, 10^{-3} , 10^{-5} |
| dust-to-gas ratio f_{dg} | 0 (dust free), 0.01 |
| dust radius a [μm] | 0.1, 10 |
| mid-plane value of plasma beta (z component) β_0 | 10^4 , 10^5 |

Table 3.2: Parameters for calculations in Section 3.2.3

$\dot{M}_{\text{p}} = \dot{M}_{\text{s}}$ and C_1 can be derived as

$$C_1 = \frac{2}{3}Ar_{\text{b}}. \quad (3.11)$$

In this way, we obtain the analytic solution for the surface density:

$$\Sigma = \frac{A}{\nu_0}r_0^{\frac{3}{2}} \left(-\frac{2}{9}r^{-\frac{1}{2}} + \frac{2}{3}r_{\text{b}}r^{-\frac{3}{2}} \right). \quad (3.12)$$

This solution for $\epsilon = 1$ and $r_{\text{b}} = 20R_{\text{J}}$ is plotted in Fig. 3.4. We consider only the mass accreted onto the central planet and neglect the mass extending outwards, thus the analytic solution is slightly larger than the numerical solution. About 10% of the infalling mass flux exits the disk outwards.

3.2.3 MRI Activity in Circumplanetary Disks

We calculate the ionization degree in circumplanetary disks for the surface densities obtained in Section 3.2.1. The parameters employed in our calculations are shown in Table 3.2. Note that cases with larger f_{dg} or smaller a than the ranges shown result in smaller MRI-active regions and the results with smaller f_{dg} or larger a approach those of the dust-free calculations. Since the magnetic field strength is uncertain, we choose optimistic values of β_0 for MRI to operate. If we focus only on the MRI, there are no heating sources if the disk is MRI-dead. The radial profiles of temperature structure are not affected

dramatically by MRI-activity as long as the disk is not hot enough for thermal ionization to be effective. Thus, we assume isothermality in our calculations of ionization degree to be consistent with the disk model. In this section, we take into account cosmic rays, X-rays, and radionuclides as ionization sources (Equation 2.14).

Fig. 3.5 shows the results for the case of $\alpha = 0.05$, $\epsilon = 1$, and $f_{\text{dg}} = 0$. The region above the solid line $\Lambda = 1$ and inside the gray shaded area ($\beta_z > 8\pi^2$) is unstable to MRI as dictated by the conditions discussed in Section 1.3.2. The hatched region illustrates $\beta_z > 2000$, the criterion for turbulence to be well developed (refer to Equation 1.11). Thus, a region of well-developed MRI turbulence is above $\Lambda = 1$ and within the hatched region. For the parameters of Fig. 3.5, there is no region that has well-developed MRI turbulence. This means that under these settings, the MRI cannot generate the accretion stress, $\alpha = 0.05$, which we have assumed in the calculations of surface density. A calculation with smaller α results in a smaller region with $\Lambda > 1$ because the surface density is larger and the ionization degree is lower. Consequently, we cannot find a self-consistent solution for Σ and α when $\epsilon = 1$.

The results for $\epsilon = 10^{-3}$ are shown in Fig. 3.6, which corresponds to the case of gap opening or global disk dispersal. Without dust grains, active layers with well-developed turbulence appear at large radii, but with dust grains, such layers do not exist in satellite-forming regions. Fig. 3.7 shows the results for $\epsilon = 10^{-5}$. The MRI-active layers become thicker but the situation does not change dramatically. It is difficult to

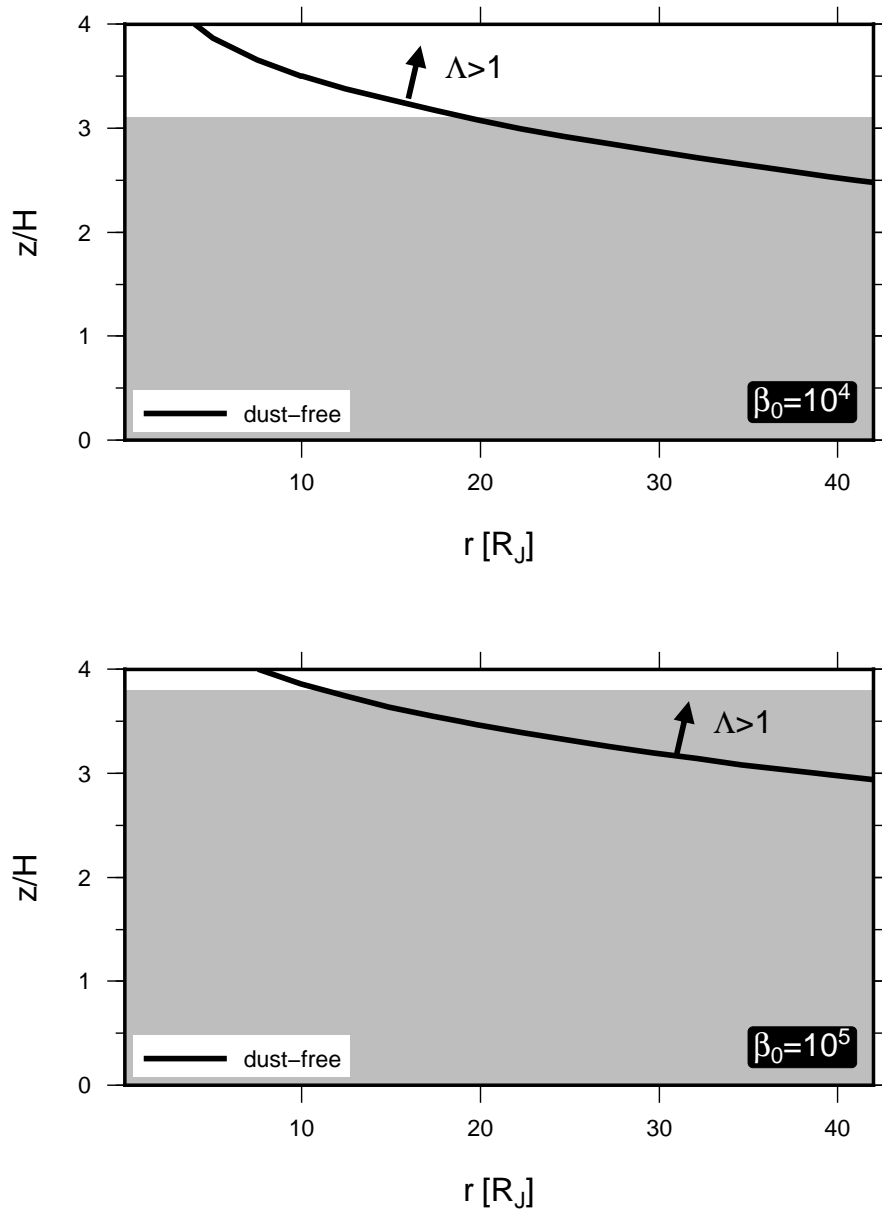


Figure 3.5: Borders of MRI-active/inactive regions. The horizontal axis is radius normalized by Jupiter radius, and the vertical axis is the vertical extent of the disk normalized by disk scale height. The solid lines show $\Lambda = 1$ for the dust-free case, and the region above the lines are $\Lambda > 1$. Shaded and hatched areas are the regions $\beta_z > 8\pi^2$ and $\beta_z > 2000$, respectively. The top panel is the case with $\beta_0 = 10^4$ and the bottom panel is the case with $\beta_0 = 10^5$. These are cases in which the infall rate is not decreased ($\epsilon = 1$). We plot only the results of dust-free cases. If there are dust grains, the ionization degree is smaller and the line $\Lambda = 1$ is higher. Gas from the protoplanetary disk infalls onto the region $r < 20 R_J$.

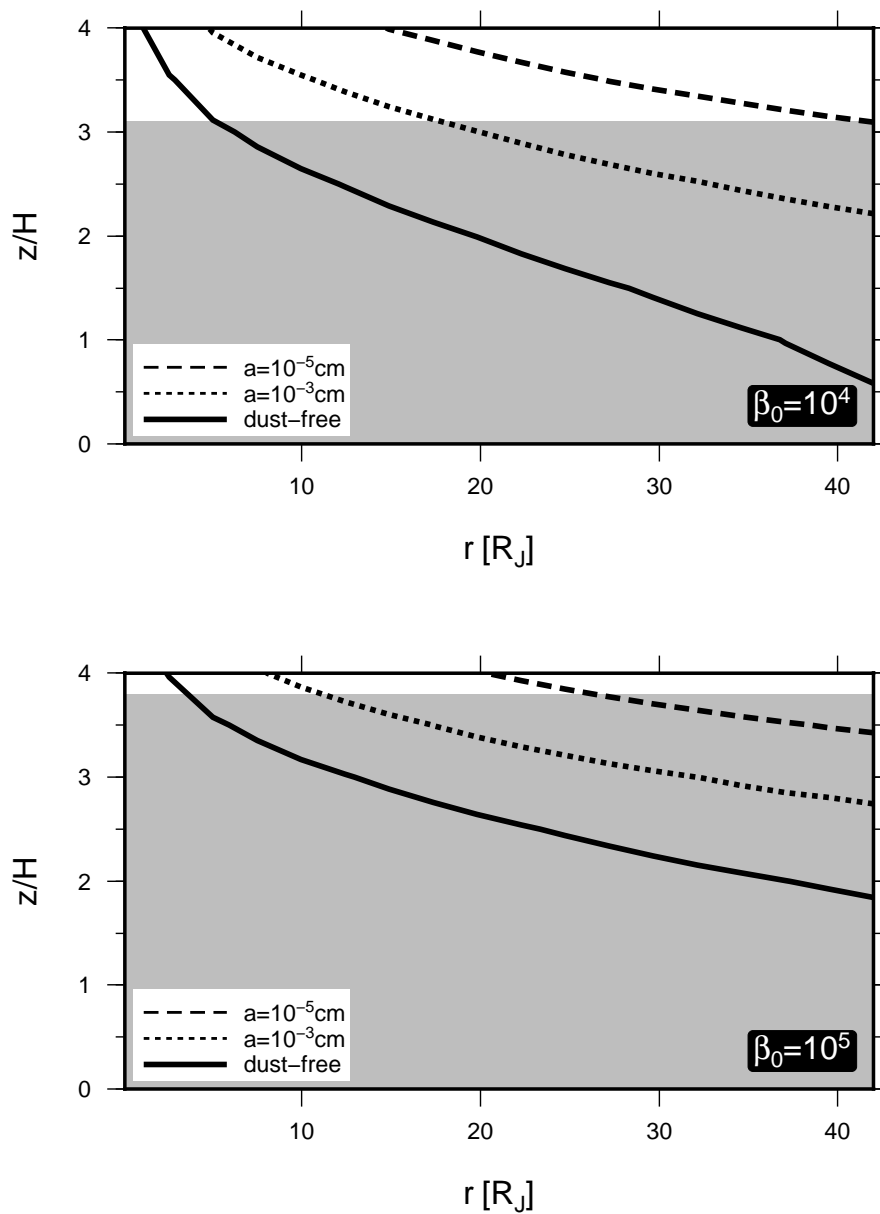


Figure 3.6: Same as Figure 3.5 but for the case of $\epsilon = 10^{-3}$. The radius of dust grains, a , used in these calculations is indicated in the figure.

sustain well-developed MRI turbulence in circumplanetary disks with dust grains, especially in areas experiencing gas infall.

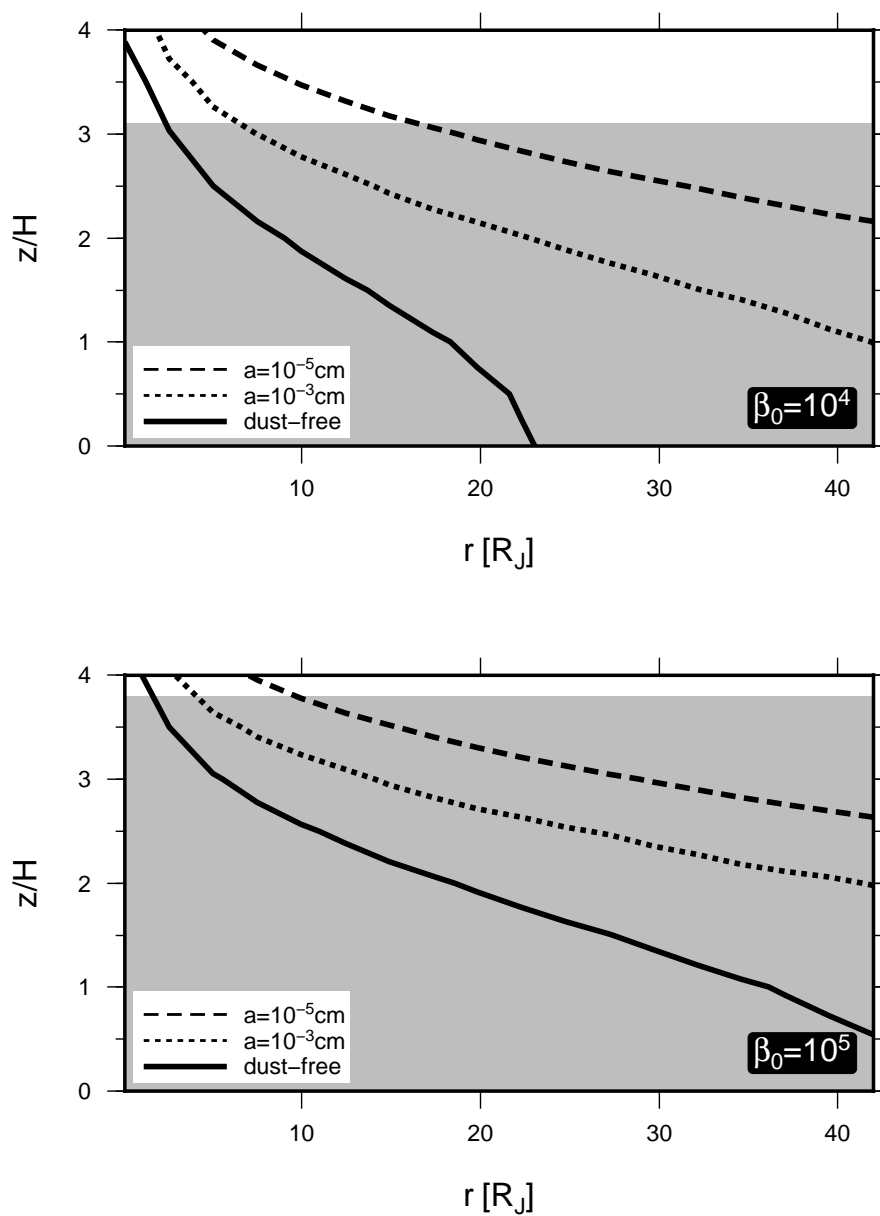
When the surface density is smaller, the ionization degree is larger and the line $\Lambda = 1$ is lower. We estimate the minimum surface density needed to form satellites to find the lower limit of the line $\Lambda = 1$. The timescale to form a satellite of radius R_s and density ρ_s orbiting at r is

$$\begin{aligned} \tau_s &\approx \frac{1}{\Omega} \frac{\rho_s R_s}{\Sigma_{\text{sol}} F_g} \\ &\sim 8\text{yr} \left(\frac{R_s}{2500 \text{ km}} \right) \left(\frac{\rho_s}{2 \text{ g cm}^{-3}} \right) \left(\frac{F_g}{100} \right)^{-1} \\ &\quad \times \left(\frac{\Sigma_{\text{sol}}}{3 \times 10^3 \text{ g cm}^{-2}} \right)^{-1} \left(\frac{r}{15R_J} \right)^{3/2}, \end{aligned} \quad (3.13)$$

where Σ_{sol} is the surface density of solids and $F_g \equiv 1 + (v_{\text{esc}}/v_\infty)^2$ is the gravitational focusing factor for colliding objects with relative velocity at infinity v_∞ and mutual escape velocity v_{esc} (Canup and Ward, 2002; Lissauer and Stewart, 1993; Ward, 1996). To form a satellite whose radius, density, and orbit are similar to Ganymede's within the lifetime of the disk, $\tau_s \sim 10^7$ yr, the required surface density of solids is

$$\Sigma_{\text{sol}} \sim 10^{-3} \text{ g cm}^{-2} \left(\frac{r}{15R_J} \right)^{3/2} \left(\frac{R_s}{2500 \text{ km}} \right) \left(\frac{\rho_s}{2 \text{ g cm}^{-3}} \right) \left(\frac{F_g}{100} \right)^{-1}. \quad (3.14)$$

The value of F_g depends on the size of the proto-satellite. Since we want to know the minimum value of Σ_{sol} , we choose the maximum value of the gravitational focusing factor, $F_g \sim 100$, when $v_\infty \simeq (M_s/3M_p)^{1/3} v_K$ (v_K is the Keplerian velocity around the planet at the proto-satellite orbit). If we assume the dust-to-gas mass ratio

Figure 3.7: Same as Fig. 3.6 but for the case of $\epsilon = 10^{-5}$.

does not depend on the height and take $f_{\text{dg}} = 10^{-2}$, the surface density of gas should be larger than $\Sigma \sim 0.1 \text{ g cm}^{-2}$. According to this estimation, and Fig. 3.4, it seems quite difficult to form satellites with $\epsilon = 10^{-5}$ or smaller. Therefore, we do not consider even smaller infall rates.

Next, we investigate the surface density at each radius that can sustain well-developed MRI turbulence. The results are summarized in Fig. 3.8. The surface densities which can sustain well-developed turbulence for $z > 2H$, $z > 0.5H$, and for the entire height at each radius are shown. The mid-plane plasma beta considered here is $\beta_0 = 10^5$. If we choose larger β_0 , the line $\Lambda = 1$ shifts higher which means the MRI-active region becomes smaller. On the other hand, if we choose smaller β_0 , the region with $\beta z > 2000$ is smaller, and having large MRI-active regions becomes difficult.

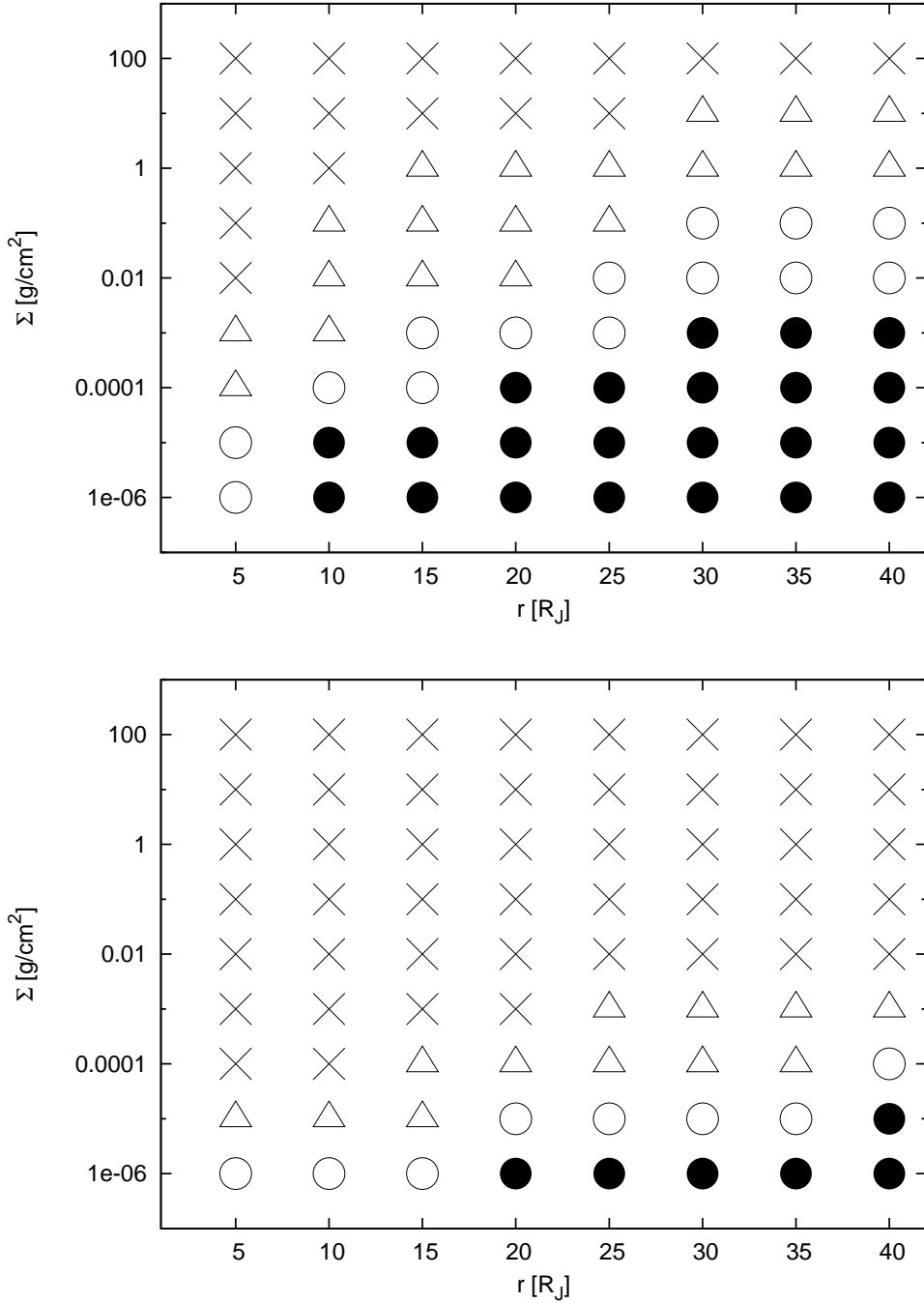


Figure 3.8: Relation between disk surface density and MRI activity at each radius. \bullet represents the surface densities at the given radius that have well-developed MRI turbulence through the entire height of the disk, \circ represents the surface densities for have well-developed turbulence only above $0.5H$, and \triangle represents those which have well-developed turbulence only above $2H$. Since we choose $\beta_0 = 10^5$, $\beta_z < 2000$ above $2.8H$ and well-developed turbulence cannot be sustained in such a region. We plot \times for the surface densities with which we cannot find regions of $\Lambda > 1$ below $2.5H$. The top panel is the result of a dust-free calculation and the bottom panel is that of a case with dust grains of $a = 0.1 \mu\text{m}$. With dust grains, the MRI-active region is smaller because of the lower ionization degree.

3.3 Implications

We find that when accounting for cosmic rays, X-rays, and radionuclides, circumplanetary disks are not likely to sustain well-developed MRI turbulence. In contrast to protoplanetary disks, the volume ratio of MRI-active regions to dead zones for circumplanetary disks is very small. This is because the typical length scale of circumplanetary disks is smaller by several orders of magnitude than that of protoplanetary disks. This makes the timescale of magnetic diffusion smaller. According to Equation (1.6), even if v_{Az} and η are the same, the Elsasser number tends to be smaller in circumplanetary disks. For example, typical ionization degrees at 5AU in a protoplanetary disk and at $15R_J$ in a circumplanetary disk are both $\sim 10^{-10}$, but the Keplerian frequency of a protoplanetary disk at 5AU is $\sim 10^{-8} \text{ s}^{-1}$ and that of a circumplanetary disk at $15R_J$ is $\sim 10^{-5} \text{ s}^{-1}$. Therefore, it is very difficult for MRI turbulence to be well developed in circumplanetary disks unless the surface density is very small, as we show in Fig. 3.8.

If there are no other mechanisms to give rise to viscosity and disks are not massive, the gas piles up in circumplanetary disks until the disks become massive enough to be gravitationally unstable. It is possible to promote gas accretion by gravitational instability (GI), but it may not reduce the disk surface density much below the critical value for GI. Therefore the surface density is expected to remain large for a long time and satellites may form in such thick and calm disks.

If there is viscous heating in such a massive disk, it will easily heat

up, and thermal ionization may drive the MRI (Lubow and Martin, 2012). Even if GI can drive turbulence, it does not necessarily mean the turbulence can generate heat in situ. The question of where the energy dissipates remains open (Balbus and Papaloizou, 1999; Goodman and Rafikov, 2001; Muto et al., 2010). We should be careful in treating the heating by gravitational turbulence. Further study of energy dissipation by GI is necessary.

If thermal ionization triggers the MRI, disks would be less massive because of a high accretion rate. Suppose that if at each annulus of a disk, gravitational energy is converted into thermal energy and radiates as a black body from the disk surface, the effective temperature is

$$T_{\text{eff}} = \left(\frac{3GM_p\dot{M}}{8\pi\sigma_{\text{SB}}r^3} \right)^{1/4}, \quad (3.15)$$

where M_p is the planet mass, \dot{M} is the mass accretion rate, and σ_{SB} is the Stefan-Boltzmann constant. We can estimate the mid-plane temperature, T_c , from the approximation $T_c \simeq \tau^{1/4}T_{\text{eff}}$ ($\tau \gg 1$), where τ is optical depth, given by $\tau \sim \kappa\Sigma$ where κ is opacity. Here we use $\dot{M} = 3\pi\nu\Sigma$. Then, the mid-plane temperature can be written as

$$T_c = 1.0 \times 10^3 \left(\frac{\kappa}{5 \text{ cm}^2 \text{ g}^{-1}} \right)^{1/5} \left(\frac{\alpha}{10^{-2}} \right)^{-1/5} \left(\frac{M_p}{M_J} \right)^{3/10} \\ \times \left(\frac{\dot{M}}{3.1 \times 10^{-7} M_J \text{ yr}^{-1}} \right)^{2/5} \left(\frac{r}{10 R_J} \right)^{-9/10} \text{ K}, \quad (3.16)$$

where M_J is the Jupiter mass. When the mid-plane temperature exceeds about 1000K, the ionization degree becomes sufficiently high to sustain the MRI. The inner disk may be hot enough to have thermal

ionization especially during the early phases of gas giant formation; however, the outer disk seems to remain cool. More detailed calculations of the mid-plane temperature of circumplanetary disks have been done by Keith and Wardle (2014).

Chapter 4

Ionization Dynamics in Protoplanetary Disks

In this chapter, the effects of ionization dynamics in protoplanetary disks are examined. We show a simple model estimation and evaluate chemical timescales. We also perform three dimensional MHD simulations with chemical species. Section 4.2 has been published as Fujii et al. (2014a).

4.1 Effects of Non-equilibrium Ionization

A proper treatment of the disk ionization degree is important for non-ideal MHD simulations. When the chemical timescale is much shorter than the dynamical timescale, the assumption of ionization equilibrium is valid, and we can use the equilibrium solution of ionization degree to compute diffusivities. If the chemical timescale is longer than the dynamical timescale, however, non-equilibrium ionization may affect the dynamics. In the absence of dust grains, the chemical timescale is known to be very large, and the dead zone size can

be smaller due to vertical turbulent mixing of ionized gas (Ilgner and Nelson, 2008; Inutsuka and Sano, 2005; Turner et al., 2007). On the other hand, in the presence of dust grains, vertical mixing is effective only in limited cases (Turner and Sano, 2008). In this chapter, we investigate the effects of non-equilibrium ionization with dust grains on the evolution of protoplanetary disks.

4.2 A Toy Model of Turbulent Mixing

When the abundance of small dust grains is negligibly small, ionized gas in the surface layer can be transferred deep inside protoplanetary disks by MHD turbulence, and the sizes of the dead zones decrease (Inutsuka and Sano, 2005). In this section, we carry out a simple model calculation to test the effect of turbulent mixing in the presence of dust grains.

We adopt the MMSN model (Hayashi, 1981) and choose $f_{\text{dg}} = 10^{-2}$ and $\beta_0 = 10^4$. We take into account cosmic rays, X-rays, and radionuclides as ionization sources (Equation 2.14), and model the vertical movement of a fluid element along an eddy as

$$z(t) = 2H \sin\left(\frac{\Omega t}{2}\right) + 2H, \quad (4.1)$$

where $z(t)$ is the distance from the mid-plane at time t , Ω is the Keplerian frequency, and H is the disk scale height. Note that, this is the only section of this chapter where scale height is defined by Equation (1.5). The time evolution of ionization degree along eddies is calculated to observe the effects of turbulent mixing on dead zone size.

Figure 4.1 shows the results. With sub-micron grains, there seems to be almost no difference between the case with an eddy and that without. With a slight increase in the size of the grains, however, we can see a difference between the two. In the latter case, the timescale of mixing we assumed is smaller than that of the chemical reactions. The timescales of the chemical reactions depend on grain size (or number density of grains), gas density, ionization rate, and so on. The sizes of a dead zone may decrease through vertical mixing, but further investigation through time-dependent calculations of the ionization degree with MHD simulations is needed.

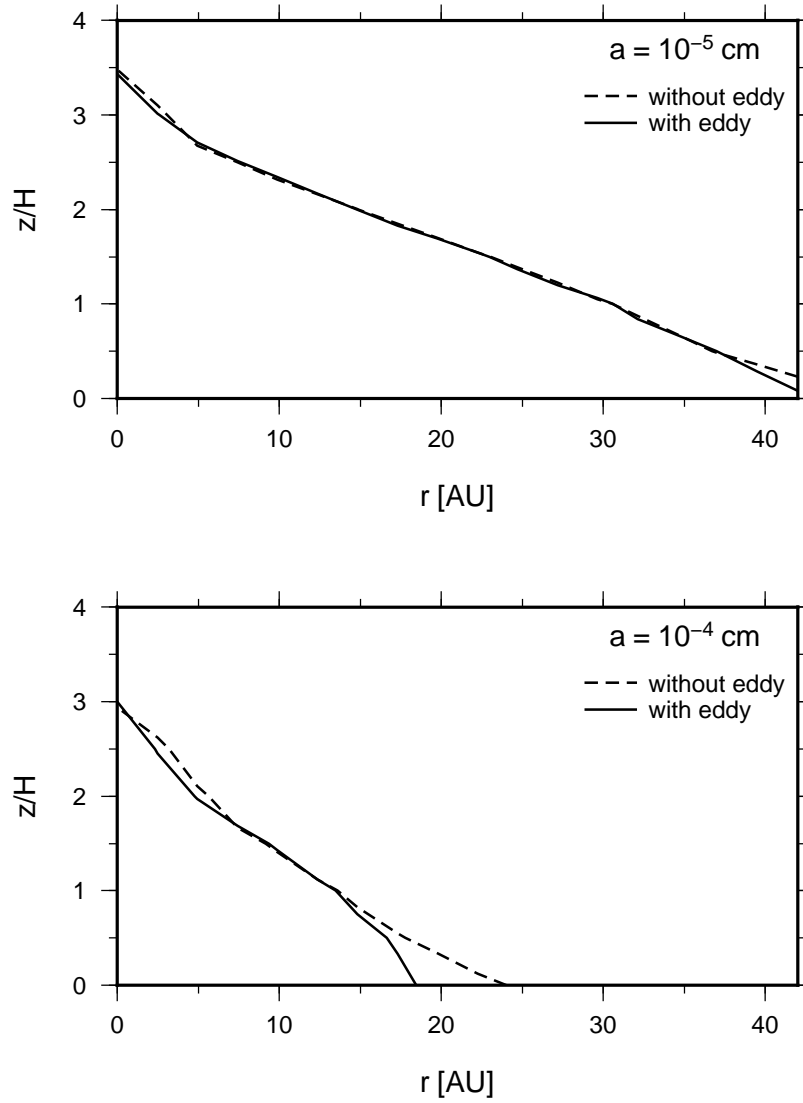


Figure 4.1: Boundaries of dead zones with grain size $a = 10^{-5}$ cm (top panel) and $a = 10^{-4}$ cm (bottom panel). The horizontal axes denote the radius of a protoplanetary disk, and the vertical axes show the vertical extent of the disk normalized by the scale height of the corresponding radius. The solid lines show the cases without eddies, and the dashed lines show the cases with eddies. The regions below the lines are dead zones.

4.3 Timescales

We rewrite the rate equations for chemical reactions (Equations (2.42)-(2.45)) that we derived in Section 2.2:

$$\frac{dn_{M^+}}{dt} = \zeta n_n - \alpha_{M^+} n_{M^+} n_e - \langle k_{M^+d} \rangle N_d n_{M^+}, \quad (4.2)$$

$$\frac{dn_e}{dt} = \zeta n_n - \alpha_{M^+} n_{M^+} n_e - \langle k_{ed} \rangle N_d n_e, \quad (4.3)$$

$$\frac{d\langle Z \rangle}{dt} = \langle k_{M^+d} \rangle n_{M^+} - \langle k_{ed} \rangle n_e, \quad (4.4)$$

$$\begin{aligned} \frac{d\langle \delta Z^2 \rangle}{dt} &= (\langle k_{M^+d} \rangle + 2\langle k_{M^+d} \delta Z \rangle) n_{M^+} \\ &+ (\langle k_{ed} \rangle - 2\langle k_{ed} \delta Z \rangle) n_e. \end{aligned} \quad (4.5)$$

In order to estimate the timescales of the reactions and the abundance of each species in protoplanetary disks, we solve Equations (4.2)-(4.5) for the MMSN disk model (Hayashi, 1981). For the calculation, we use the method described in Chapter 2 with cosmic rays, stellar X-rays, and radionuclides as ionization sources.

The dominant species as a function of disk radius for $\beta_0 = 10^5$ and $a = 10^{-4}$ cm with various f_{dg} are shown in Figure 4.2. From charge neutrality, the charge of all species balance each other throughout the evolution. In the high-density regime, the total charge of metal ions is balanced with that of dust grains; n_{M^+} is comparable to $|\langle Z \rangle N_d|$ (denoted by dots in Figure 4.2). Note that the electron number density is several orders of magnitude smaller than n_{M^+} and $|\langle Z \rangle N_d|$ because they are mostly absorbed by dust grains. Thus, $\langle Z \rangle$ is a negative value. On the other hand, in the low-density regime, n_{M^+} is in charge balance with n_e (denoted by large circles in Figure 4.2) because a sufficient number of electrons and ions is supplied by ionization. The

intermediate case, defined as the smaller of n_e or $|\langle Z \rangle N_d|$ being at least 10% of the other quantity, is denoted by small circles. Similar plots for $a = 10^{-5}$ are shown in Figure 4.3. In these parameter ranges, mostly, metal ions and electrons are balanced near the dead zone boundary. In Figure 4.4, the dominant species near the dead zone boundaries for various strengths of magnetic field are plotted. Since the chemical reactions are not affected by magnetic fields, only the line showing $\Lambda = 1$ varies. The dead zone boundaries are located in the areas where charged dust grains are not a dominant species.

However, grain surface reactions are important for determining the chemical timescale. From Equation (4.3), the timescales of ionization, radiative recombination, and capture onto grain surface are written as

$$t_{\text{ioniz}} \sim \frac{n_{\text{M}^+}}{\zeta n_{\text{n}}}, \quad (4.6)$$

$$t_{\text{rec}} \sim \frac{1}{\alpha_{\text{M}^+} n_{\text{M}^+}}, \quad (4.7)$$

$$t_{\text{cap}} \sim \frac{1}{\langle k_{\text{ed}} \rangle N_d}. \quad (4.8)$$

When the system is in equilibrium, t_{ioniz} balances with either t_{rec} or t_{cap} . The borders of areas where grain surface capture of electrons dominates gas phase recombination, and vice versa, are plotted in green in Figures 4.5-4.9. The dead-zone boundaries are shown in blue, and the lines along which the timescale of chemical reactions, t_{ioniz} , equals the typical eddy turnover time of MRI turbulence, $t_{\text{Kep}} \equiv 1/\Omega$, is plotted in red. It can be seen that the green lines are far above the blue lines in most of the plots. Thus, although charged dust grains

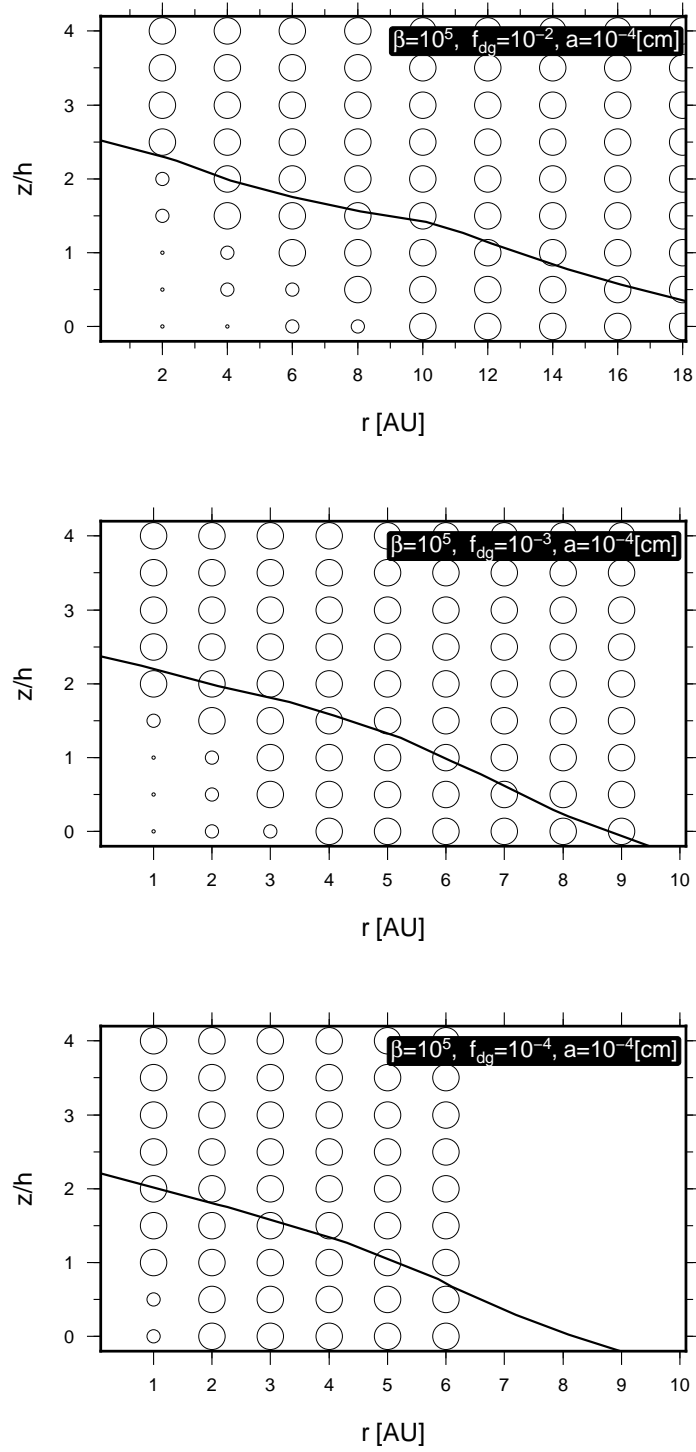


Figure 4.2: Combinations of species holding positive and negative charge for $\beta_0 = 10^5$ and $a = 10^{-4}$ cm and, from top to bottom, $f_{dg} = 10^{-2}$, 10^{-3} , 10^{-4} . Large circles mean that n_{M^+} and n_e hold most of the positive and negative charge. Dots show that the metal ions and dust grains are in charge balance, i.e., $qn_{M^+} + q\langle Z \rangle N_d = 0$. Small circles represent the intermediate case. The solid curve corresponds to $\Lambda = 1$.

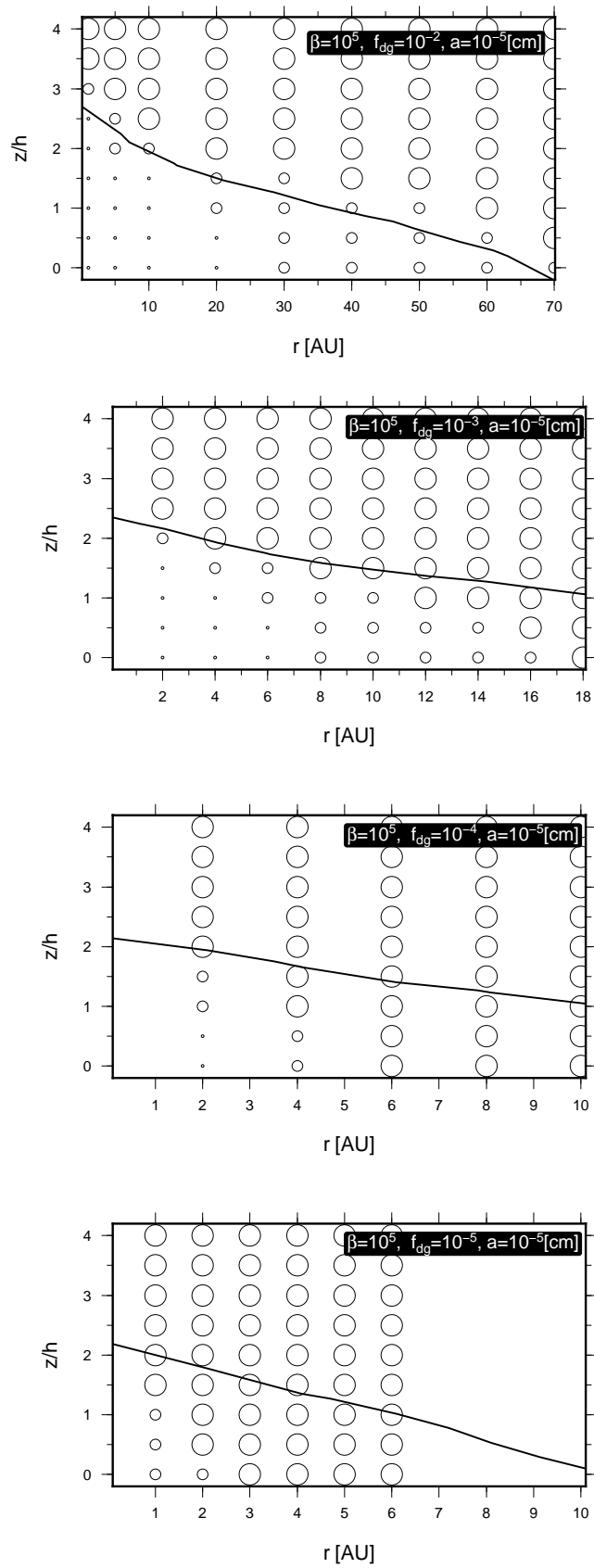


Figure 4.3: Same as Figure 4.2 but for $a = 10^{-5}$ cm and, from top to bottom, $f_{dg} = 10^{-2}, 10^{-3}, 10^{-4}, 10^{-5}$.

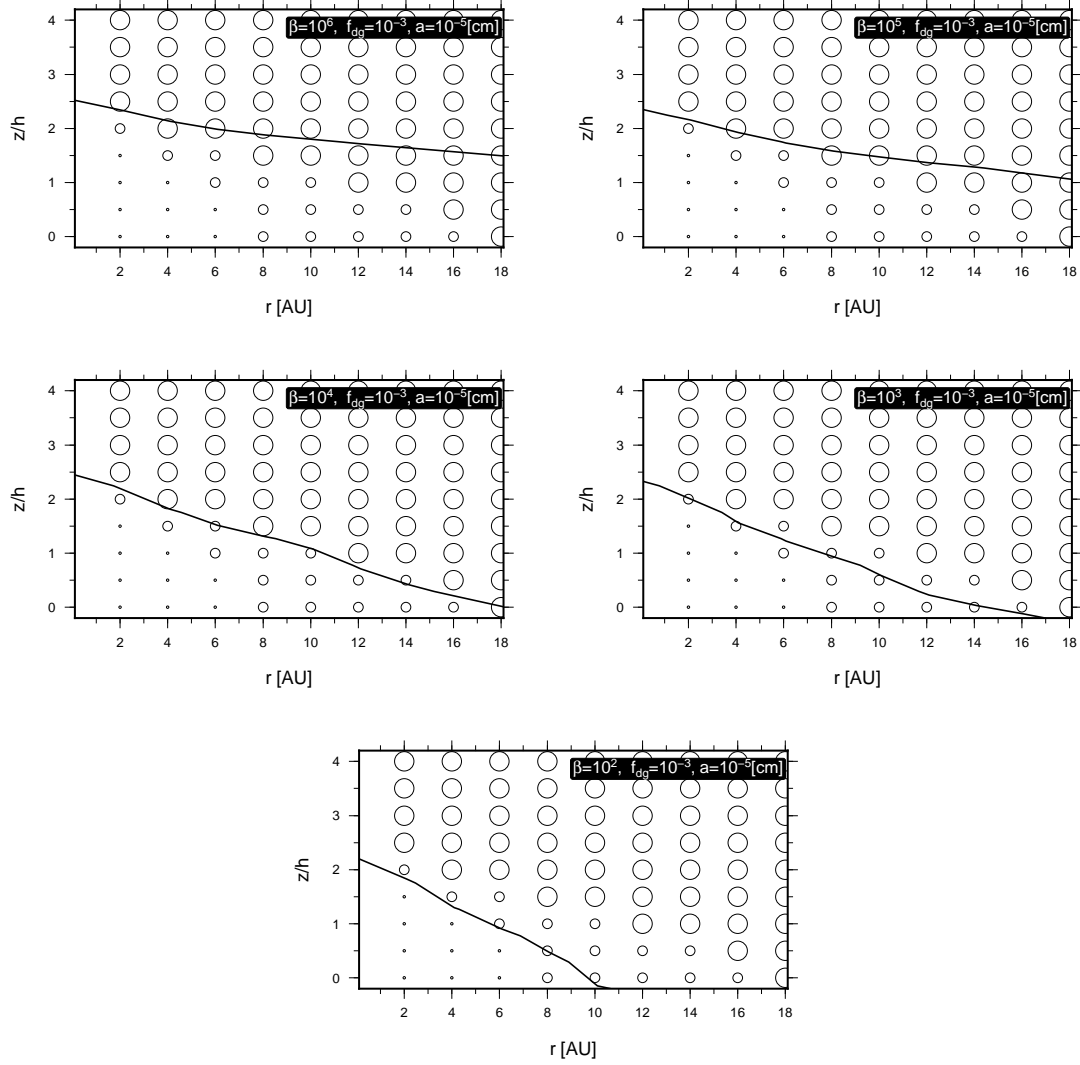


Figure 4.4: Same as Figure 4.3 but for β_0 is varied between 10^2 and 10^6 with f_{dg} held constant at 10^{-3} . Note that only the line showing $\Lambda = 1$ varies.

are less abundant near a dead-zone boundary, grain surface reactions dominate the gas phase reactions in large areas, including near the boundary of dead zones. In this section, we choose the set of parameters $\beta_0 = 10^6$, $f_{\text{dg}} = 10^{-2}$, and $a = 10^{-5}$ cm as a fiducial model. In Figure 4.5, the dead-zone boundary is located at a larger scale height for weaker magnetic field. This indicates a better chance of vertical mixing for weaker magnetic field cases, unless a stronger magnetic field causes very strong turbulence. However, the distance between the blue and red lines is large for the fiducial parameter setting. In the left side panels of Figure 4.6, grain size is an order of magnitude larger than in the fiducial model, and in the right side panels, the dust-to-gas mass ratio is an order of magnitude lower. Basically, these two changes have a similar effect. Thus, the dead-zone boundaries appear at a similar place. In Figure 4.7, the changes in f_{dg} and a are two orders of magnitude in total, and in Figures 4.8 and 4.9, three and four orders of magnitude, respectively. The smaller the value of f_{dg} , or the larger the value of a , the lower the location of the red lines becomes, but at the same time, the size of the dead zones becomes smaller. Thus, there are not many cases for which the dead zone size is affected by vertical mixing of ionized materials with these parameter settings.

In Figure 4.10, the results for a disk whose surface density is 0.01 times that of the MMSN model (0.01MMSN) are shown. In the bottom panel, the line for which the timescale of chemical reactions equals the typical eddy turnover time of MRI turbulence is located in the

vicinity of the dead-zone boundary. Thus, this case is thought to be worth investigating in detail with numerical simulations.

The abundance of each chemical species as a function of distance from the mid-plane at 2AU for the 0.01MMSN model is shown in Figure 4.11. Since the values of $\langle Z \rangle$ and $\langle dZ^2 \rangle$ are mainly determined by temperature and grain size, they do not vary with height at a given orbit.

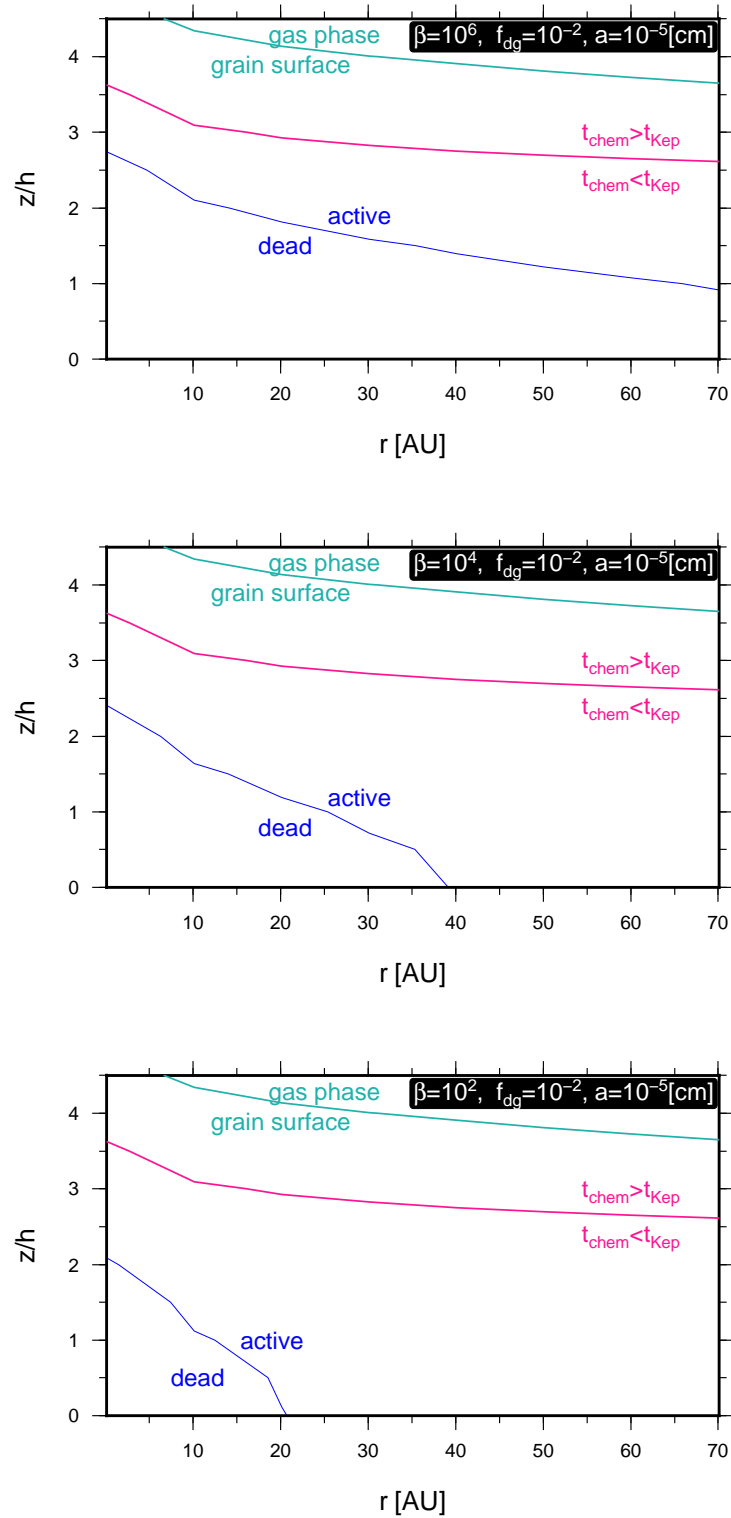


Figure 4.5: Reaction timescales and dead zone boundaries for $f_{dg} = 10^{-2}$, $a = 10^{-5}$ cm, and, from top to bottom, $\beta_0 = 10^6$, 10^4 , 10^2 . The dead-zone boundary is shown in blue. In the region above the green line, gas phase recombination is faster than grain surface capture of dust grains. The red line shows the location where the timescale of chemical reactions, t_{chem} , equals the dynamical timescale, t_{Kep} .

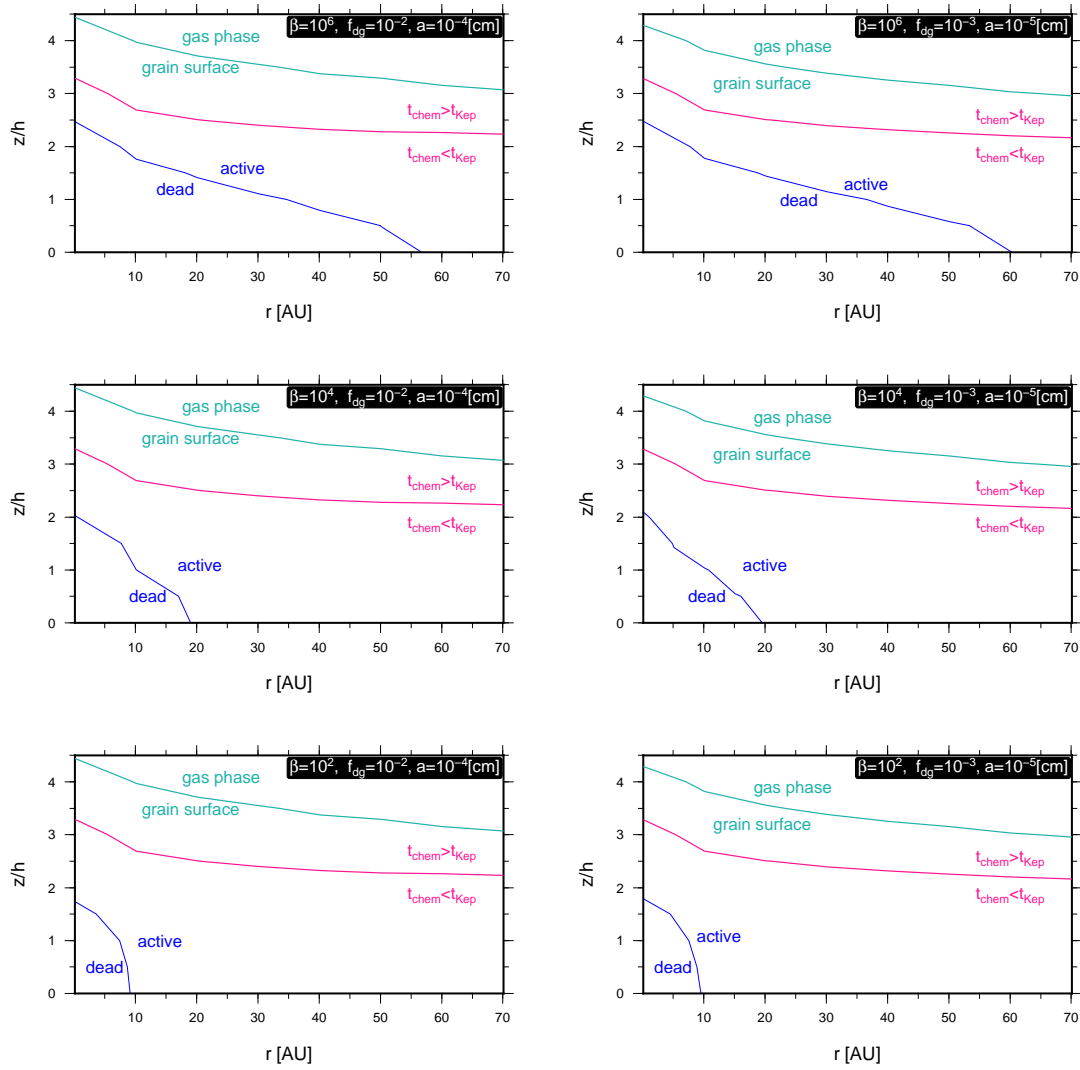


Figure 4.6: Line colors have the same meanings as in Figure 4.5. The left side panels are the cases with $f_{\text{dg}} = 10^{-2}$ and $a = 10^{-4}$ cm, and the right side panels are the cases with $f_{\text{dg}} = 10^{-3}$ and $a = 10^{-5}$ cm. On both sides, the values of β_0 from top to bottom are 10^6 , 10^4 , and 10^2 .

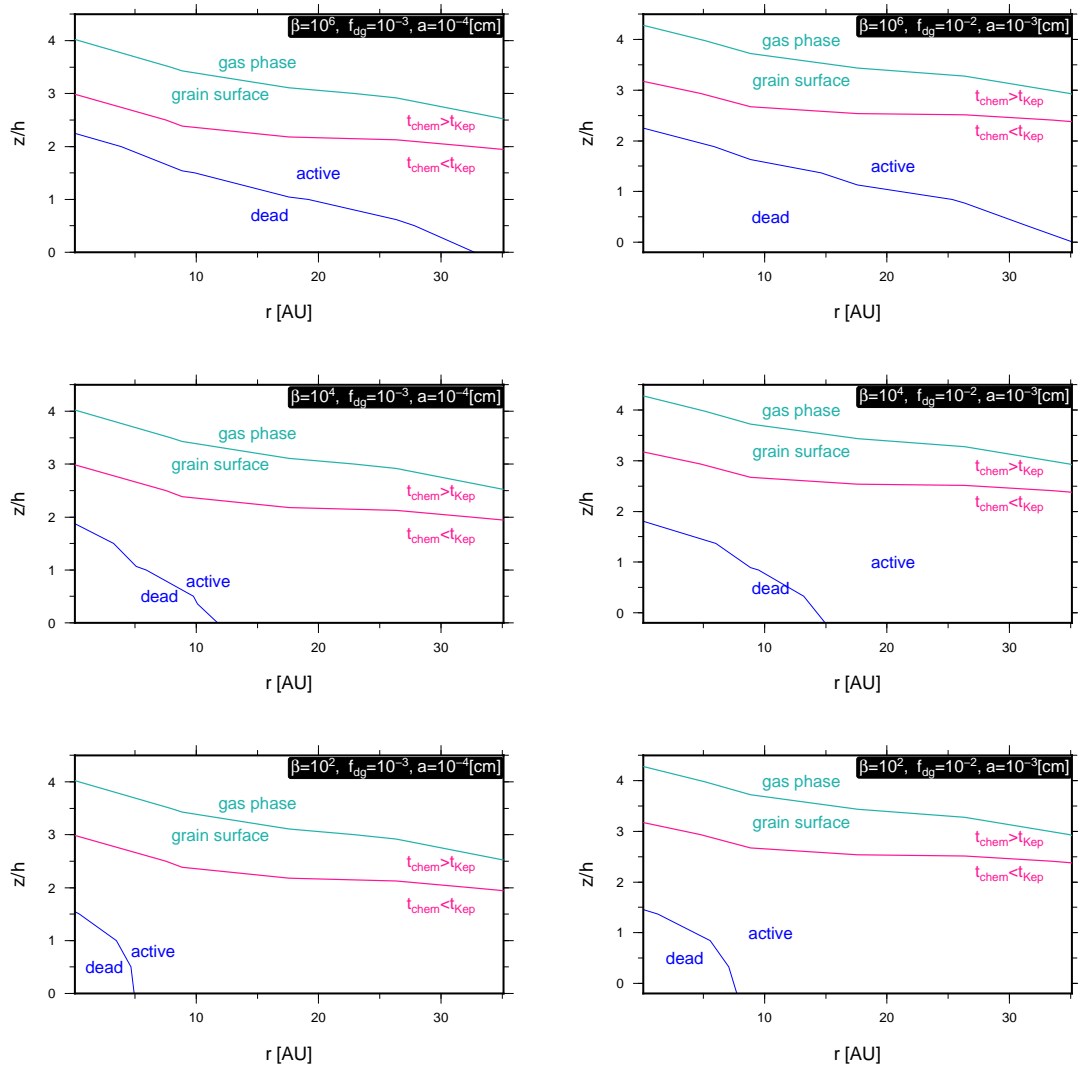


Figure 4.7: Line colors have the same meanings as in Figure 4.5. The left side panels are the cases with $f_{\text{dg}} = 10^{-3}$ and $a = 10^{-4}$ cm, and the right side panels are the cases with $f_{\text{dg}} = 10^{-2}$ and $a = 10^{-3}$ cm. On both sides, the values of β_0 are 10^6 , 10^4 , and 10^2 from top to bottom.

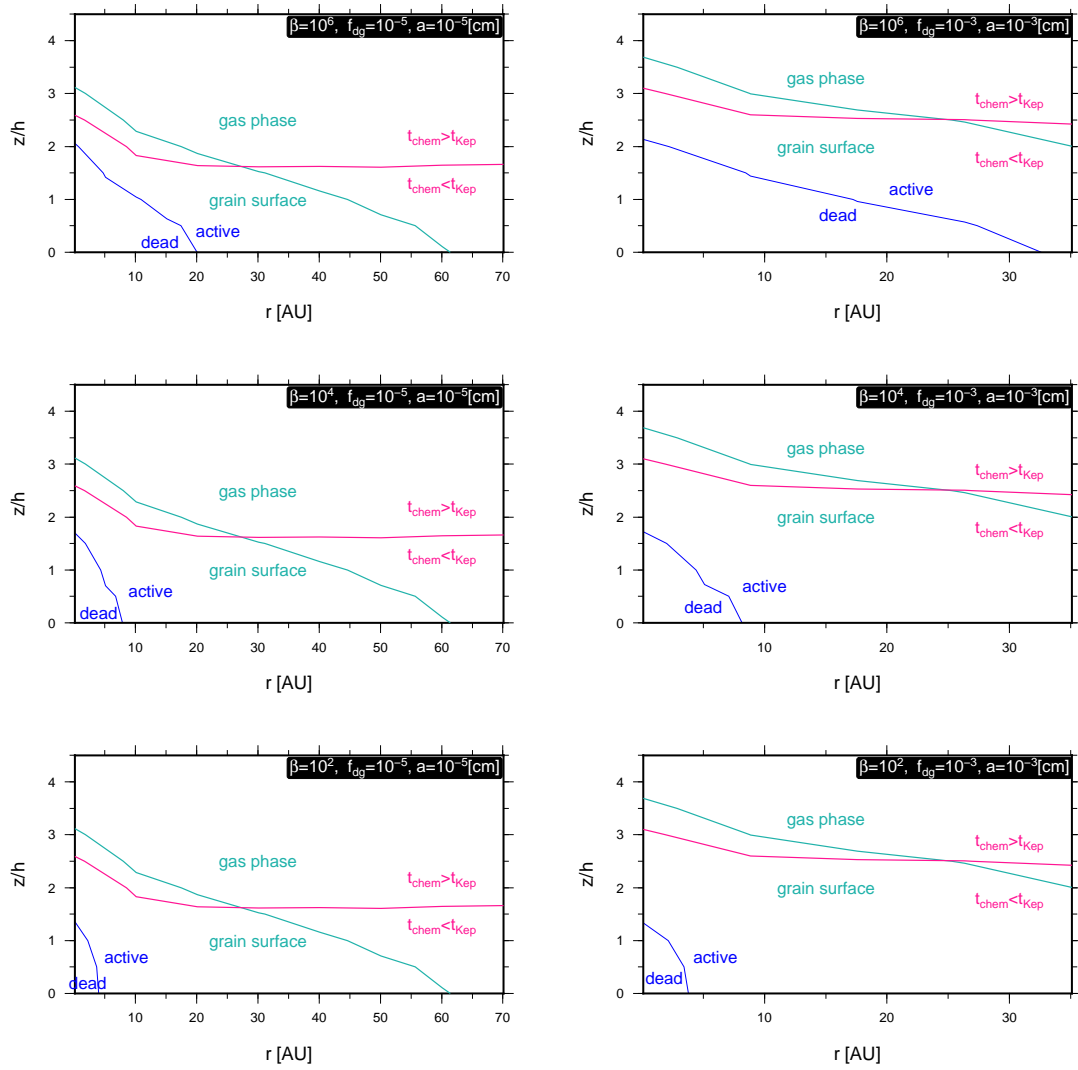


Figure 4.8: Line colors have the same meanings as in Figure 4.5. The left side panels are the cases with $f_{\text{dg}} = 10^{-5}$ and $a = 10^{-5}$ cm, and the right side panels are the cases with $f_{\text{dg}} = 10^{-3}$ and $a = 10^{-3}$ cm. On both sides, the values of β_0 are 10^6 , 10^4 , and 10^2 from top to bottom.

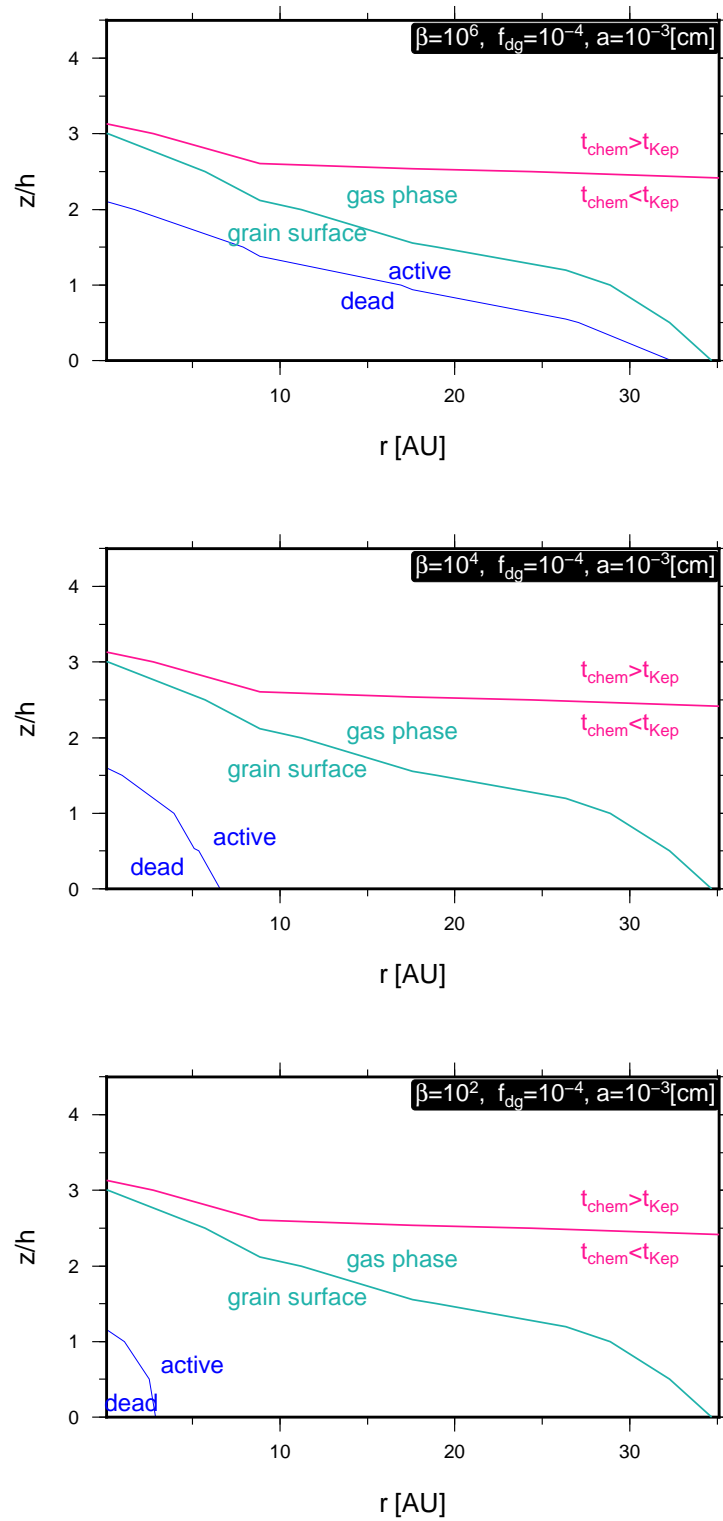


Figure 4.9: Line colors have the same meanings as in Figure 4.5. Here, $f_{dg} = 10^{-4}$, $a = 10^{-3}$ cm, and the values of β_0 are 10^6 , 10^4 , and 10^2 from top to bottom.

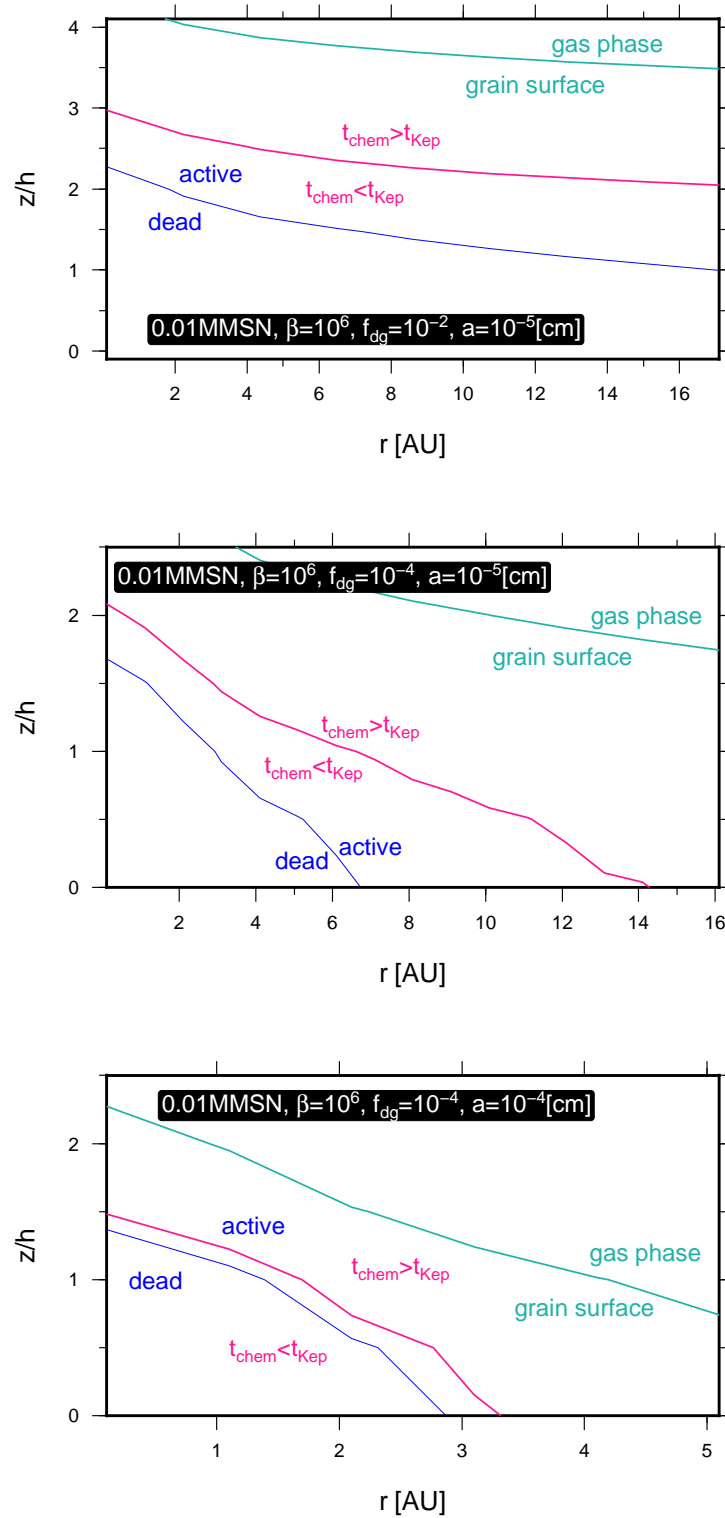


Figure 4.10: Results for the 0.01MMSN model. Line colors have the same meanings as in Figure 4.5. β_0 is kept as 10^6 , and from top to bottom, the cases with $f_{\text{dg}} = 10^{-2}$ and $a = 10^{-5}$ cm, $f_{\text{dg}} = 10^{-4}$ and $a = 10^{-5}$ cm, and $f_{\text{dg}} = 10^{-4}$ and $a = 10^{-4}$ cm are shown.

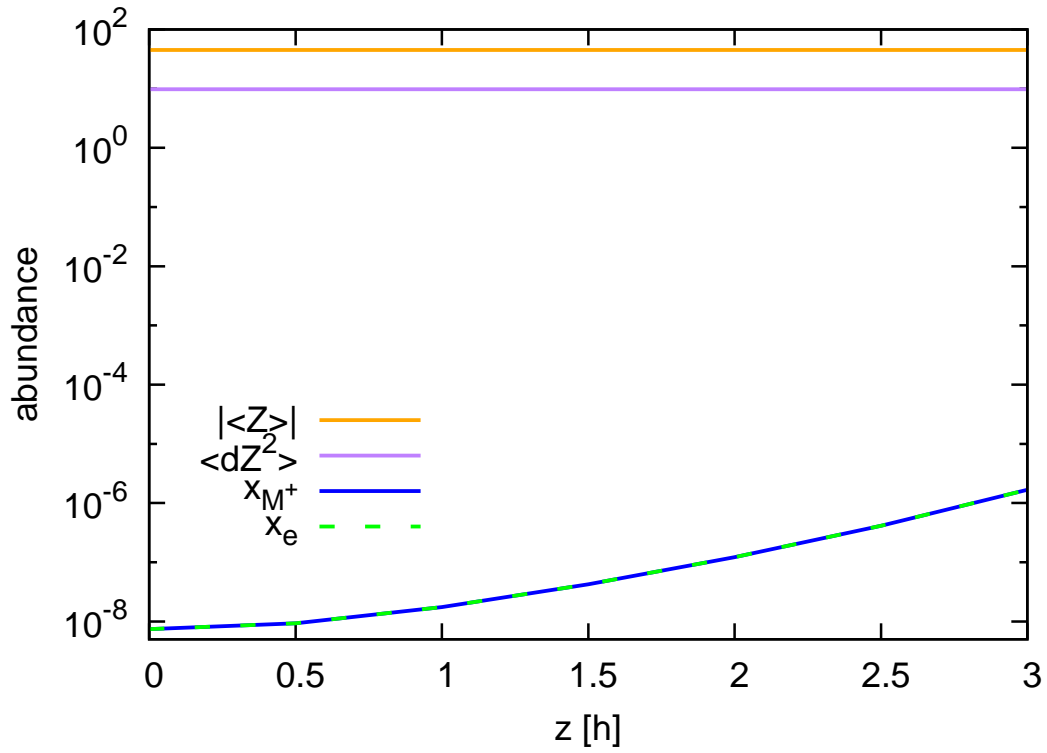


Figure 4.11: Equilibrium values of $|\langle Z \rangle|$, $\langle dZ^2 \rangle$, $x_{M^+} \equiv n_{M^+}/n_n$, and x_e at 2AU in the 0.01MMSN model. We choose the parameter set of $\beta_0 = 10^6$, $f_{\text{dg}} = 10^{-4}$, and $a = 10^{-4}$ cm (from the bottom panel of Figure 4.10).

4.4 MHD Simulations

In this section, we investigate the effects of non-equilibrium ionization on detailed numerical simulations of magnetized protoplanetary disks.

4.4.1 Simulation Setup

We consider a small patch of disk of size much smaller than the distance from the central star r_0 . This patch is called a shearing box (Goldreich and Lynden-Bell, 1965). In a shearing box, a cylindrical coordinate system centered on the star can be approximated by a local Cartesian coordinates as $x = r - r_0$, $y = r_0\phi$, and z rotating with the Keplerian velocity of the center of the box (Figure 4.4.1).

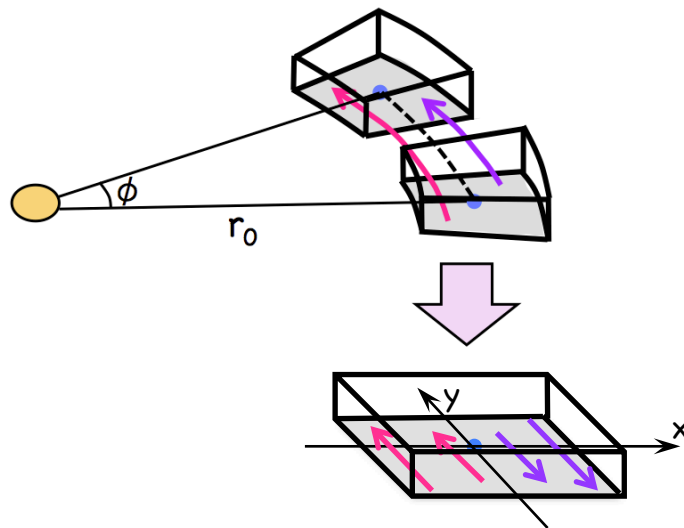


Figure 4.12: Illustration of the shearing box approximation.

We use the Athena MHD code (Stone et al., 2008) to solve the MHD equations in a shearing box (Hawley et al., 1995) for conservation of

mass, conservation of momentum, and the induction equation:

$$\frac{\partial \rho}{\partial t} + \nabla \cdot (\rho \mathbf{v}) = 0, \quad (4.9)$$

$$\begin{aligned} \frac{\partial \rho \mathbf{v}}{\partial t} + \nabla \cdot (\rho \mathbf{v} \mathbf{v} - \mathbf{B} \mathbf{B}) + \nabla \left(P + \frac{1}{2} B^2 \right) \\ = 3\rho \Omega^2 \mathbf{x} - \rho \Omega^2 \mathbf{z} - 2\mathbf{\Omega} \times \rho \mathbf{v}, \end{aligned} \quad (4.10)$$

$$\frac{\partial \mathbf{B}}{\partial t} - \nabla \times (\mathbf{v} \times \mathbf{B}) = \nabla \times (-\eta \nabla \times \mathbf{B}), \quad (4.11)$$

where ρ is density, \mathbf{v} is velocity, P is the gas pressure, \mathbf{B} is the magnetic field, and η is Ohmic resistivity, which is defined by Equation (1.7). $\hat{\mathbf{x}}$, $\hat{\mathbf{y}}$, and $\hat{\mathbf{z}}$ are unit vectors pointing in the radial, azimuthal, and vertical directions, respectively. We use an isothermal equation of state, $P = \rho c_s^2$. Note that we choose the system of units to have magnetic permeability $\mu = 1$ and, to avoid the extra factor of $\sqrt{4\pi}$, use units for magnetic field such that the magnetic pressure is $B^2/2$. The second term on the right-hand side of Equation (4.10) is the vertical gravity from the central star, and the inclusion of this in the momentum equation allows our simulations to have vertical density stratification. The first and third terms are the centrifugal force and Coriolis force, respectively. An orbital advection algorithm (Johansen et al., 2009; Masset, 2000) is also implemented. The velocity can be decomposed into the background shear flow $\mathbf{v}_K = -3/2\Omega x \hat{\mathbf{y}}$ and velocity fluctuations \mathbf{u} :

$$\mathbf{v} = \mathbf{v}_K + \mathbf{u}. \quad (4.12)$$

Note that \mathbf{v}_K is time independent. Using Equation (4.12), Equations

(4.9-4.11) can be rewritten as

$$\frac{\partial \rho}{\partial t} + v_K \frac{\partial \rho}{\partial y} + \nabla \cdot (\rho \mathbf{u}) = 0, \quad (4.13)$$

$$\begin{aligned} \frac{\partial \rho \mathbf{u}}{\partial t} + v_K \frac{\partial \rho \mathbf{u}}{\partial y} + \nabla \cdot (\rho \mathbf{u} \mathbf{u} - \mathbf{B} \mathbf{B}) + \nabla \left(P + \frac{1}{2} B^2 \right) \\ = 2\rho \Omega u_y \hat{\mathbf{x}} - \frac{1}{2} \rho \Omega u_x \hat{\mathbf{y}} - \rho \Omega^2 \mathbf{z}, \end{aligned} \quad (4.14)$$

$$\frac{\partial \mathbf{B}}{\partial t} - \nabla \times (\mathbf{v}_K \times \mathbf{B}) - \nabla \times (\mathbf{u} \times \mathbf{B}) = -\nabla \times (\eta \nabla \times \mathbf{B}). \quad (4.15)$$

When we split Equations (4.13-4.15) into a linear advection part and a fluctuation part, the linear advection part is given by

$$\frac{\partial \rho}{\partial t} + v_K \frac{\partial \rho}{\partial y} = 0, \quad (4.16)$$

$$\frac{\partial \rho \mathbf{u}}{\partial t} + v_K \frac{\partial \rho \mathbf{u}}{\partial y} = 0, \quad (4.17)$$

$$\frac{\partial \mathbf{B}}{\partial t} - \nabla \times (\mathbf{v}_K \times \mathbf{B}) = 0, \quad (4.18)$$

and the fluctuation part is given by

$$\frac{\partial \rho}{\partial t} + \nabla \cdot (\rho \mathbf{u}) = 0, \quad (4.19)$$

$$\begin{aligned} \frac{\partial \rho \mathbf{u}}{\partial t} + \nabla \cdot (\rho \mathbf{u} \mathbf{u} - \mathbf{B} \mathbf{B}) + \nabla \left(P + \frac{1}{2} B^2 \right) \\ = 2\rho \Omega u_y \hat{\mathbf{x}} - \frac{1}{2} \rho \Omega u_x \hat{\mathbf{y}} - \rho \Omega^2 \mathbf{z}, \end{aligned} \quad (4.20)$$

$$\frac{\partial \mathbf{B}}{\partial t} - \nabla \times (\mathbf{u} \times \mathbf{B}) = -\nabla \times (\eta \nabla \times \mathbf{B}). \quad (4.21)$$

Note that Equations (4.19-4.21) have the same formulation as Equations (4.9-4.11). In order to increase the efficiency of calculations, the advection part and fluctuation part are solved separately.

The y -boundary conditions are strictly periodic. For the x -boundary conditions, the orbital velocity difference is considered. Thus, when we denote the box size in the x direction as L_x ,

$$f(x, y, z) \mapsto f(x \pm L_x, y \mp wt, z), \quad (4.22)$$

$$\rho v_y(x, y, z) \mapsto \rho v_y(x \pm L_x, y \mp wt, z) \mp \rho w, \quad (4.23)$$

where $f = (\rho, \rho v_x, \mathbf{B})$ and $w = 3/2\Omega L_x$ is the orbital velocity difference across the box (Gressel and Ziegler, 2007; Hawley et al., 1995). For the z -boundary, we adopt outflow boundary conditions which allow only an outgoing flow and set the vertical velocity to zero in the case of an inward flow. The density is extrapolated assuming hydrostatic equilibrium and the other variables are extrapolated with zero slope.

In this chapter (excluding Section 4.2), we define the scale height as $h = \sqrt{2}c_s/\Omega$ and use $h = 1$, $\Omega = 1$, and $\rho_0 = 1$, where ρ_0 is the mid-plane density. We set the initial density profile to be $\rho = \rho_0 \exp(-z^2/h^2)$ and choose a constant net vertical magnetic field $B_{z,0}$ so that $\beta = 10^6$ at the mid-plane. Initially, a density floor of 10^{-6} is applied, and about 30 orbits after the simulation is started it is changed to 5×10^{-5} . This is to avoid the small time steps caused by large Alfvén velocities. The abundances of electrons and metal ions are set to zero at the beginning. The box size is $(x, y, z) = (\pm 0.5h, \pm 2h, \pm 4h)$ and is divided into (16, 32, 384) grid zones.

For the ionization degree calculation, we use Equation (2.14) for the ionization rate, and Equations (2.38)-(2.41) for the rate coefficients of grain surface absorption of charged particles. We use the equilibrium

values for $\langle Z \rangle$ and $\langle dZ^2 \rangle$ from Figure 4.11 and only solve the time evolution of electron and metal ion number densities:

$$\frac{\partial n_{M^+}}{\partial t} + \nabla \cdot (n_{M^+} \mathbf{v}) = \zeta n_n - \alpha_{M^+} n_{M^+} n_e - \langle k_{M^+d} \rangle N_d n_{M^+}, \quad (4.24)$$

$$\frac{\partial n_e}{\partial t} + \nabla \cdot (n_e \mathbf{v}) = \zeta n_n - \alpha_{M^+} n_{M^+} n_e - \langle k_e \rangle N_d n_e. \quad (4.25)$$

4.4.2 Results

We present the simulation results at 2AU of the MMSN model with 0.01 times smaller surface density (0.01MMSN model). In Figure 4.13 a snapshot of the velocity field is shown. Channel flows and velocity shears can be seen as eddies.

In most of the following plots, a space average over the x - y plane and a time average over 100-200 orbits are taken. In Figure 4.14 we plot the magnetic energy B_j^2 , where j represents the x, y, z components. Both the x and y components of the magnetic field were initially zero, thus these components are generated through the evolution. Although the magnetic field is amplified, the mean field is remains small. Figure 4.15 shows plots of $\langle B_x B_y \rangle$ and $\langle B_x \rangle \langle B_y \rangle$. As we can see, $\langle B_x B_y \rangle$ is a few orders of magnitude larger than $\langle B_x \rangle \langle B_y \rangle$. This means that the magnetic field is turbulent rather than coherent. We calculate $\alpha = \langle \rho u_x u_y - B_x B_y \rangle / \langle \rho \rangle c_s^2$ and present the results in Figure 4.16.

The gas accretion rates in the surface layers are higher than those inside the disk.

We observe a disk wind, an outward flow from the surface of the disk caused by MHD turbulence (Suzuki and Inutsuka, 2009). Figure

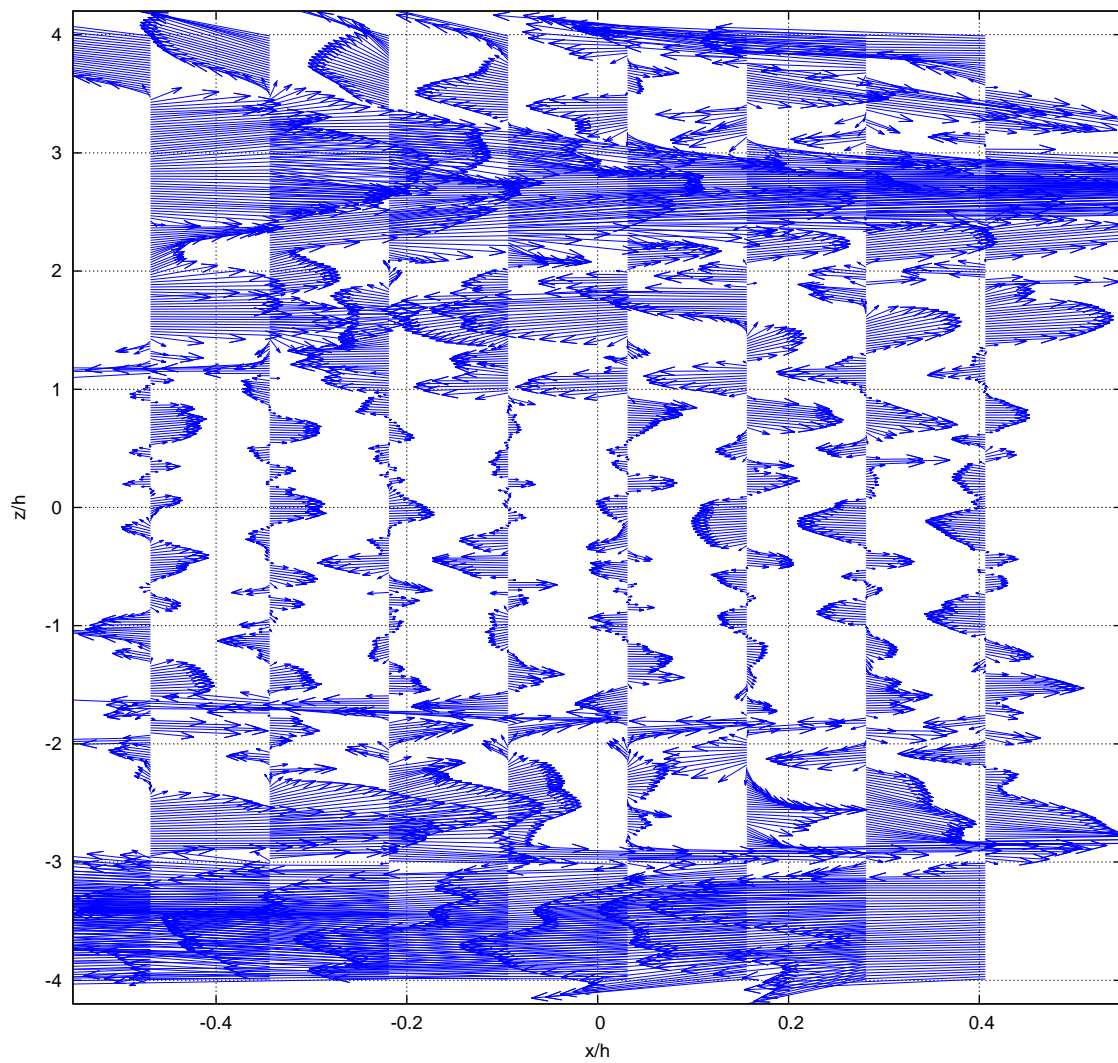


Figure 4.13: Snapshot of the velocity field on the x - z plane ($y=0$) 199.75 orbits after the simulation started.

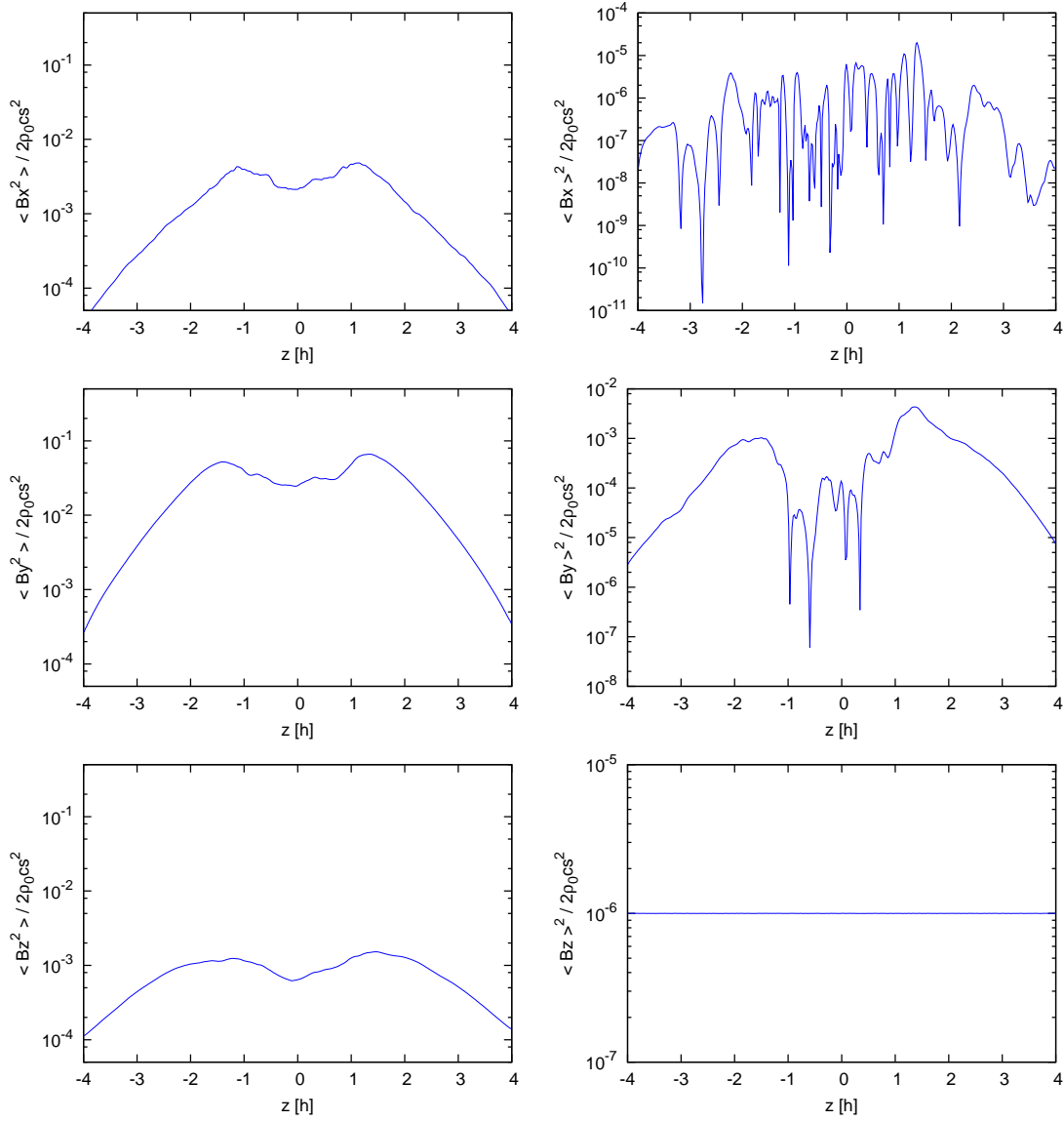


Figure 4.14: Horizontally-averaged magnetic energy of each component. A time average is also taken over 100-200 orbits.

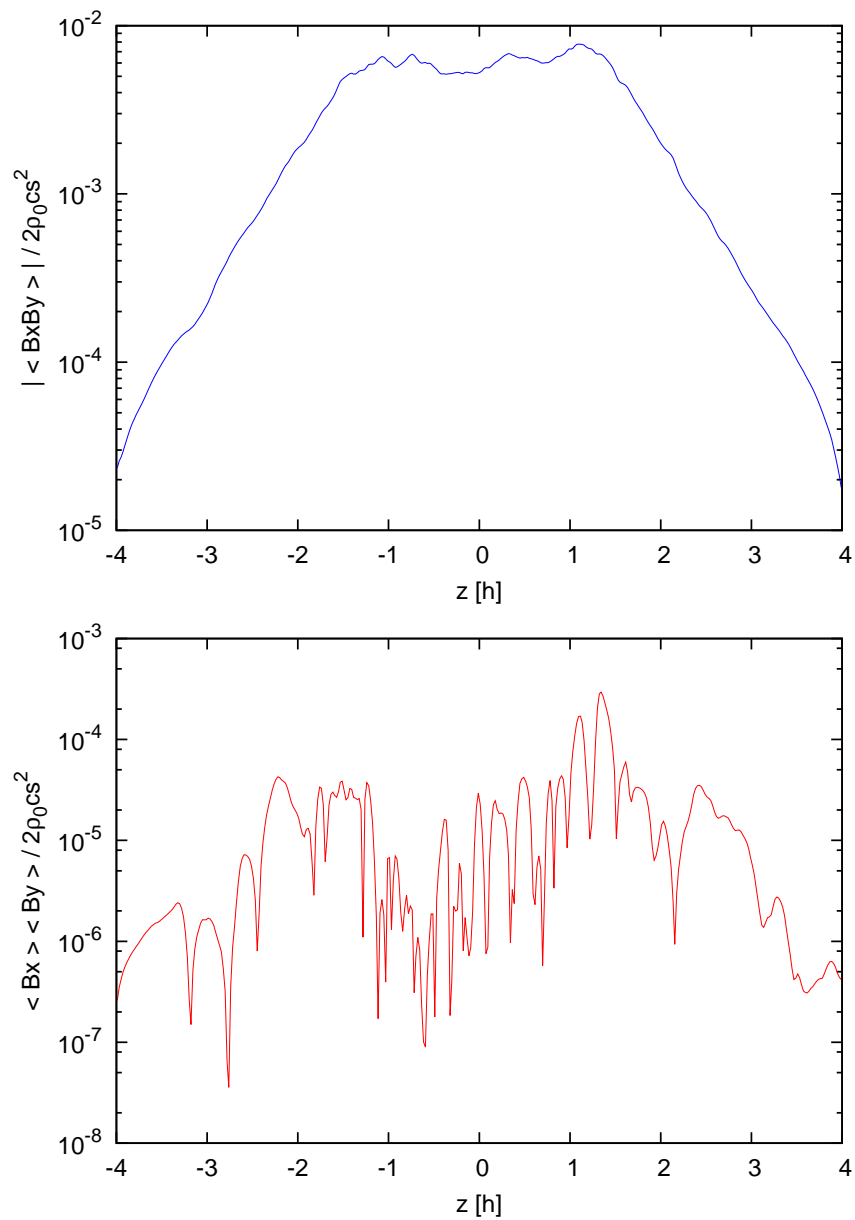


Figure 4.15: Averaged Maxwell stress $B_x B_y$ (upper panel) and its coherent component (lower panel). Averages are taken in the same manner as for Figure 4.14.

4.17 shows the wind velocity, given by $\langle v_z \rangle \equiv \langle \rho v_z \rangle / \langle \rho \rangle$. One can see that there are outward flows and the velocity increases from a height of around $\pm 2.5h$. In Figure 4.18 we plot the z -component of mass flux in the t - z plane at quarter-orbit intervals. One can see that mass flows out from the vertical boundaries. The cycle of this quasi-periodic time variation is ~ 5 -10 orbits, which is consistent with Suzuki and Inutsuka (2009) and Suzuki et al. (2010). In Figure 4.19 the initial and averaged density profiles are shown. Initially the disk is hydrostatic, but because of the disk wind mass is loaded up to the surface layers. A comparison of the ionization degree obtained by the simulation and the equilibrium solutions for the ionization degree of one-zone calculations is shown in Figure 4.20. At high altitudes, the ionization degree from the simulation is smaller than that of the one-zone calculations. This is because low-ionization-degree gas in deeper regions of the disk is transported to the surface layer by the disk wind.

The timescale of vertical advection by the disk wind is $t_{\text{adv}} = h/|v_z|$. When we take the typical eddy turnover time of MRI turbulence, $1/\Omega$, as a correlation time, the timescale of turbulent diffusion is written as $t_{\text{diff}} = h^2\Omega/\delta v_z^2$. According to Figure 4.21, the timescale of turbulent diffusion is too large to have vertical mixing of chemical species. On the other hand, the advection timescale is relatively small except in the vicinity of the mid-plane, where the advection timescale cannot be defined because v_z is almost zero. Above and below $\pm 3h$, fluid elements can travel more than one scale height by the time needed for chemical reactions to reach equilibrium. Although the averaged verti-

cal velocity profile is smooth (Figure 4.17), the actual time evolution of the vertical velocity shows strong time variation. Figure 4.22 plots the horizontally-averaged ionization degree as a function of height at every quarter an orbital period. Note that the vertical axis is correct only for the lowest plot (the other plots are vertically offset for clarity). We can see the correlation of ionization degree at shifted heights, which shows the vertical propagation of ionization degree as waves.

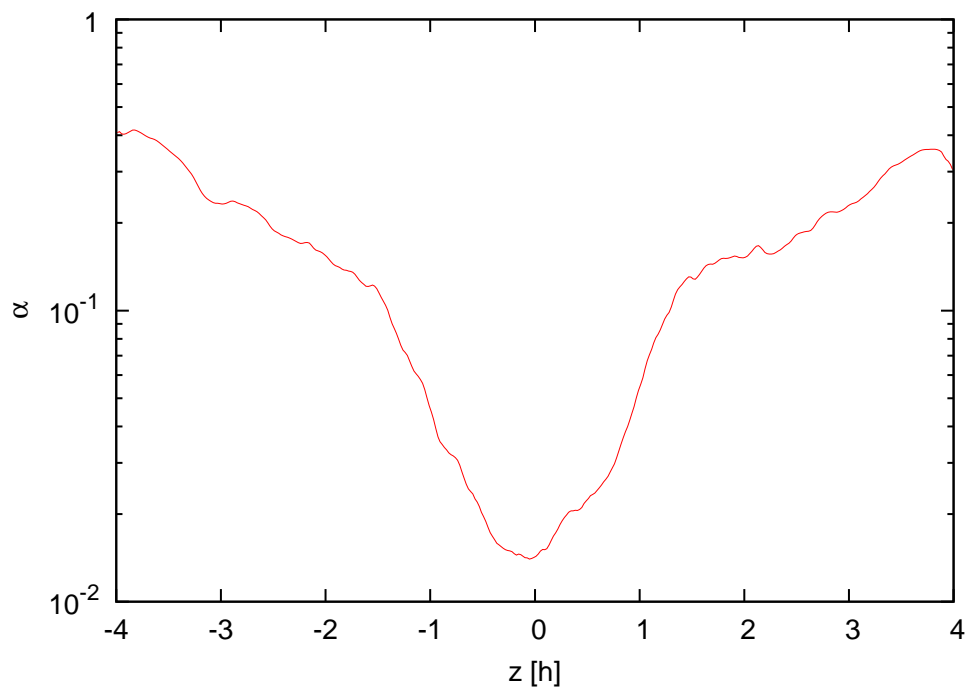
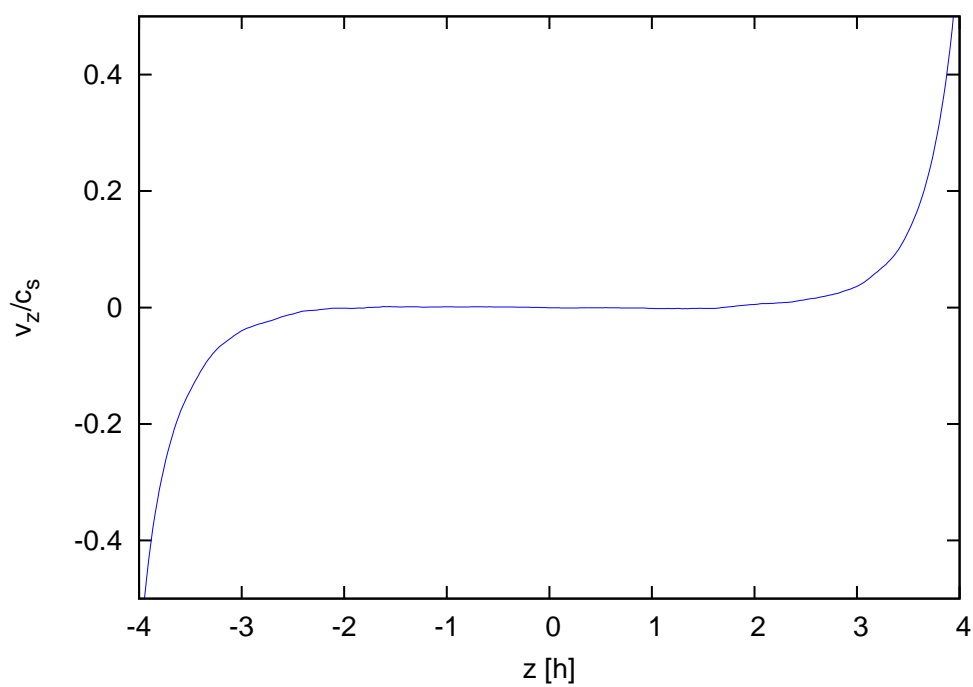


Figure 4.16: Averaged alpha parameter.

Figure 4.17: Averaged velocity of the disk wind. The wind starts to accelerate at around $\pm 2.5 h$.

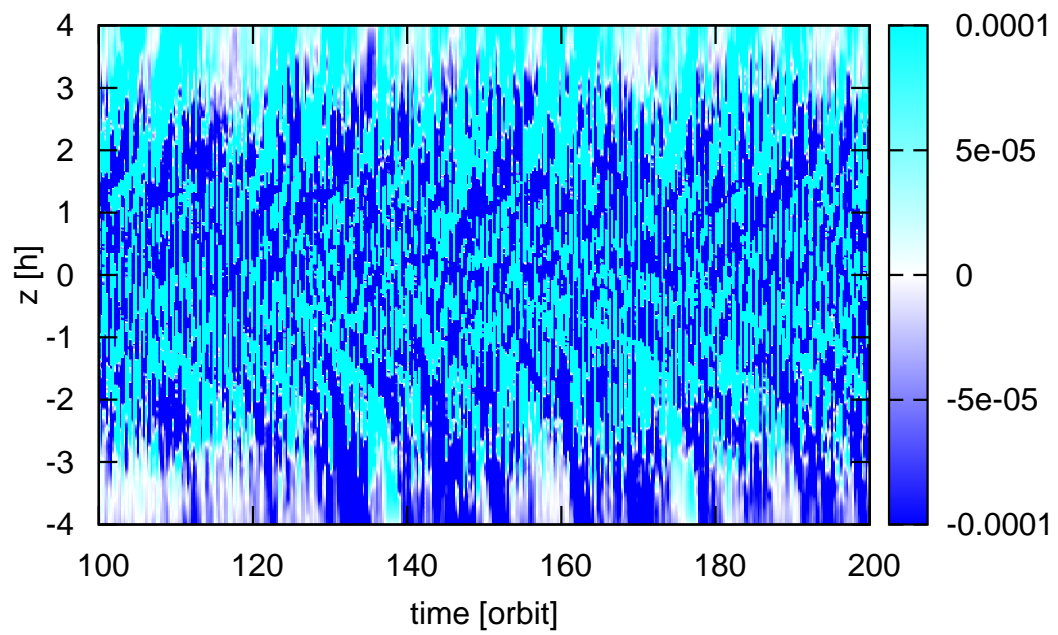


Figure 4.18: Time variation of horizontally-averaged vertical mass flux, $\rho v_z / (\sqrt{2} \rho_0 c_s)$.

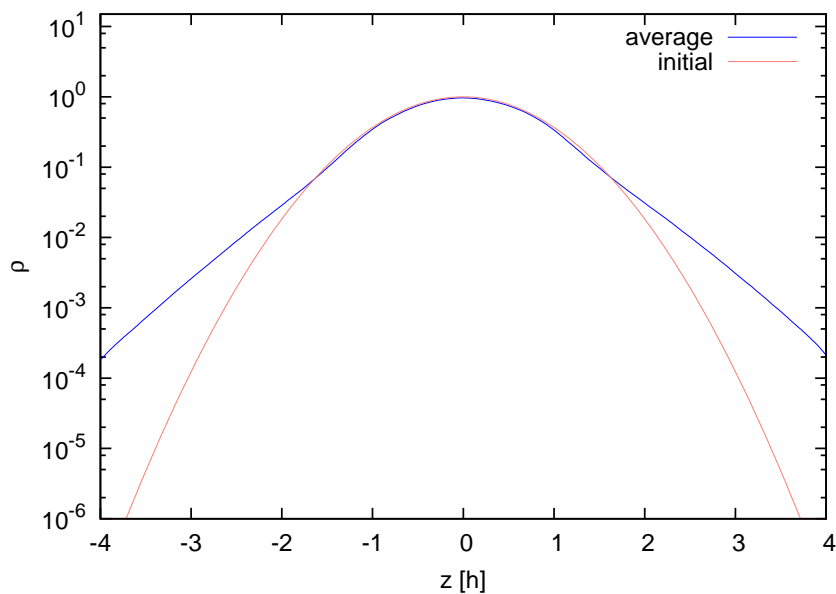


Figure 4.19: Averaged and initial density. The initial hydrostatic profile is kept near the mid-plane, but the density increases due to the disk wind in the surface layers.

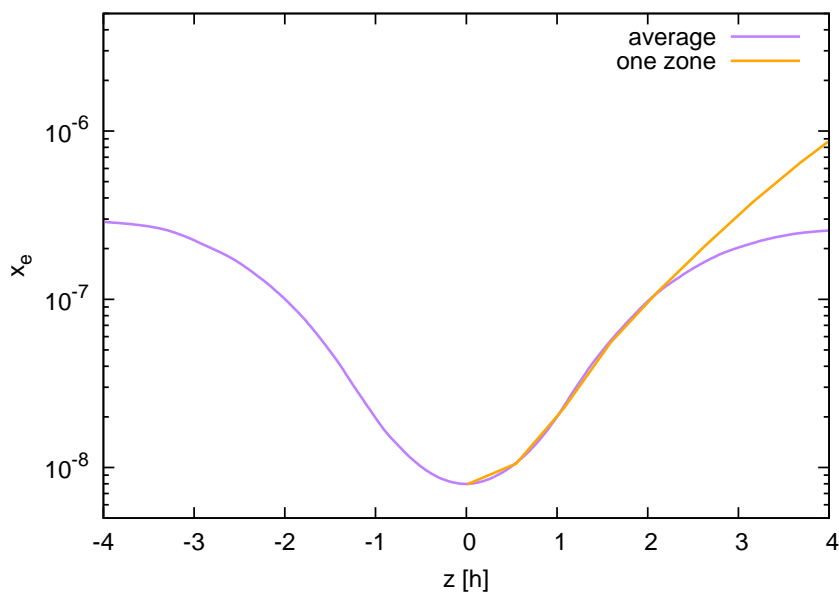


Figure 4.20: Ionization degree; the purple line is the averaged simulation result and the orange line shows the equilibrium solutions of one-zone calculations with the same density profile.

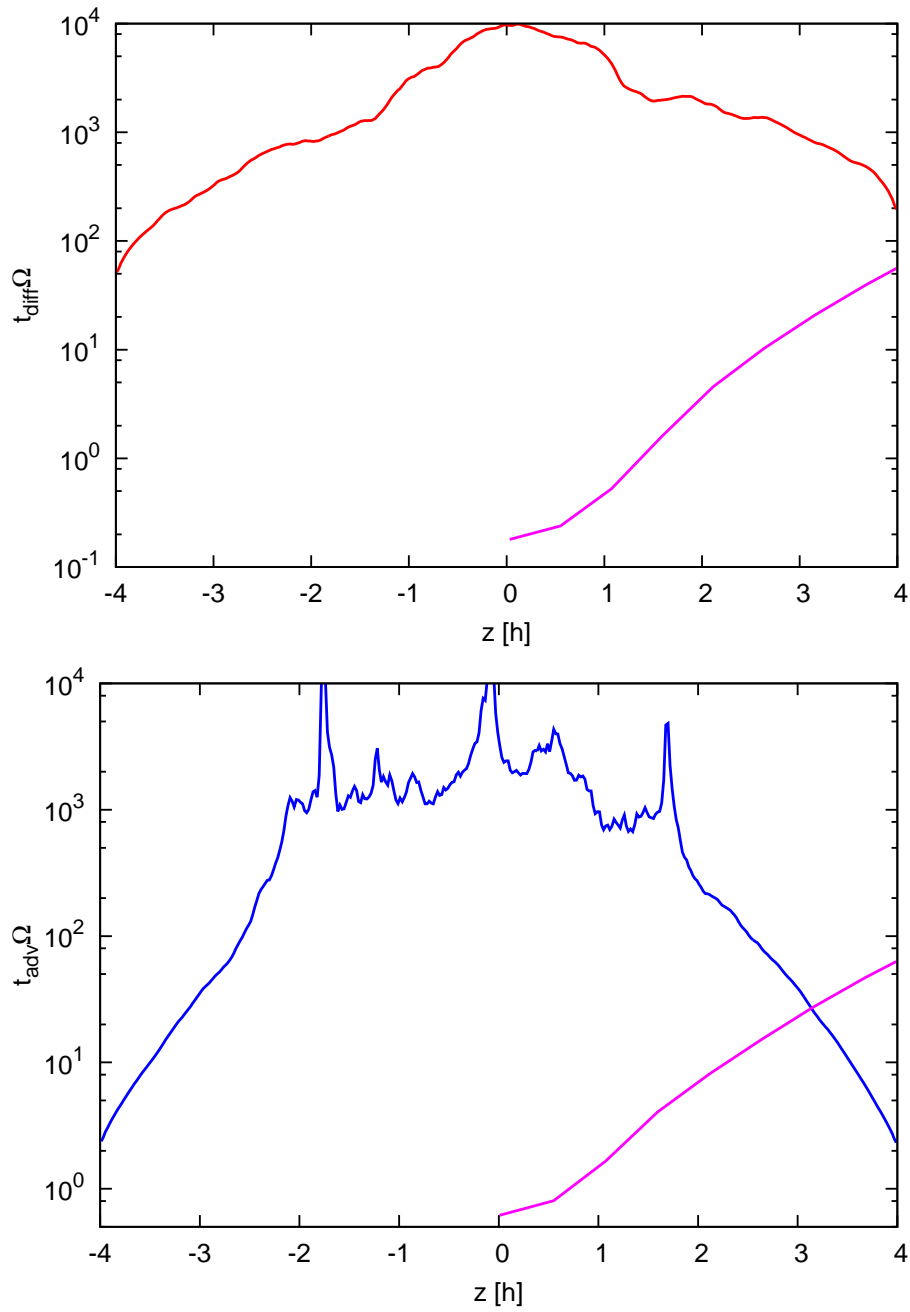


Figure 4.21: Timescales of diffusion by turbulence (upper panel) and vertical advection by the disk wind (lower panel). The timescale for chemical reactions to reach equilibrium is shown in magenta.

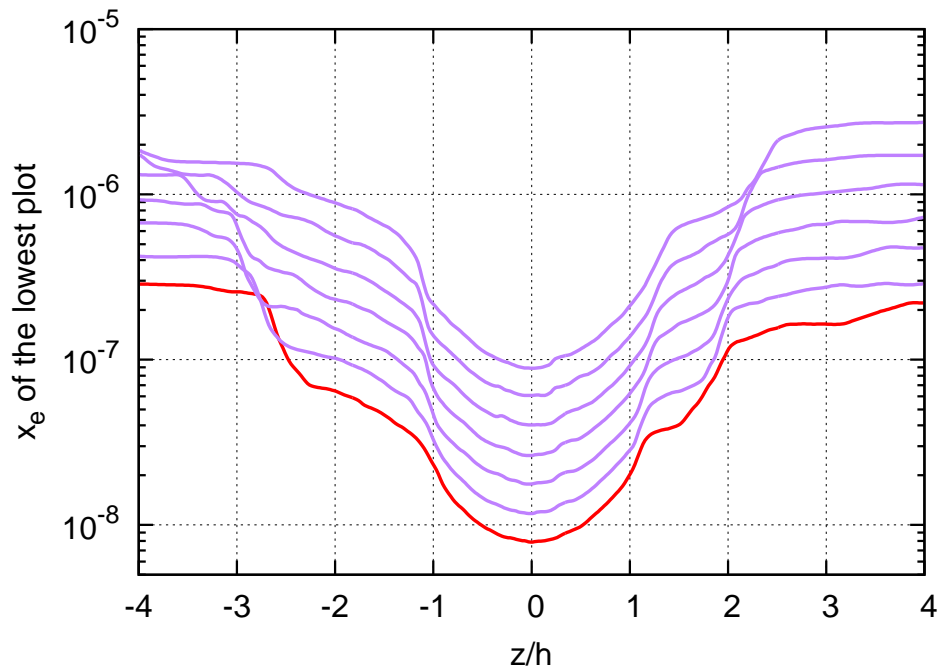


Figure 4.22: Propagation of ionization degree. The value of the ionization degree averaged over the x - y plane is plotted as a function of height. From the lowest to uppermost lines, time is increased by one quarter of an orbital period. Large gradients at about $1.5 h$, $1.2 h$, $-1 h$, and $-2.3h$ propagate outward. Note that the vertical axis is correct only for the lowest plot (the other plots are vertically offset for clarity).

4.5 Conclusions and Discussion

In order to search for the conditions for which non-equilibrium ionization affects MHD evolution, we estimated the timescale for the ionization degree of protoplanetary disk gas to reach equilibrium using various parameter settings. In our fiducial model, $\beta = 10^6$, $f_{\text{dg}} = 10^{-2}$, and $a = 10^{-5}$ cm, the grain surface reaction of charged particle absorption dominates throughout most of the disk. In this regime, generally, the chemical timescale is very short, and thus we can use the equilibrium solution of ionization degree when we treat non-ideal MHD effects. If the timescale of ionization chemistry is longer than that of the dynamical evolution, however, non-equilibrium ionization may affect the dynamics. Chemical timescales are very large in the absence of small dust grains. In this Thesis, we studied the timescales for the cases of a small abundance of grains and/or larger grains. We find that, in the MMSN model, the chemical timescales are much shorter than the dynamical timescale near the dead zone boundaries —if we reduce dust grains too much, the dead zone becomes smaller and the separation of the line on which the chemical timescale equals the dynamical timescale and the dead zone boundary does not become small. In the case of the 0.01MMSN model, there exist parameter ranges in which the line of $t_{\text{chem}} = t_{\text{Kep}}$ is close to the dead zone boundary.

We performed MHD simulations at 2AU of the 0.01MMSN model with $\beta = 10^6$, $f_{\text{dg}} = 10^{-4}$, and $a = 10^{-4}$ cm, corresponding to the disk evolution stage when the gas has mostly dissipated and most of the small grains have grown into larger bodies. We find that the

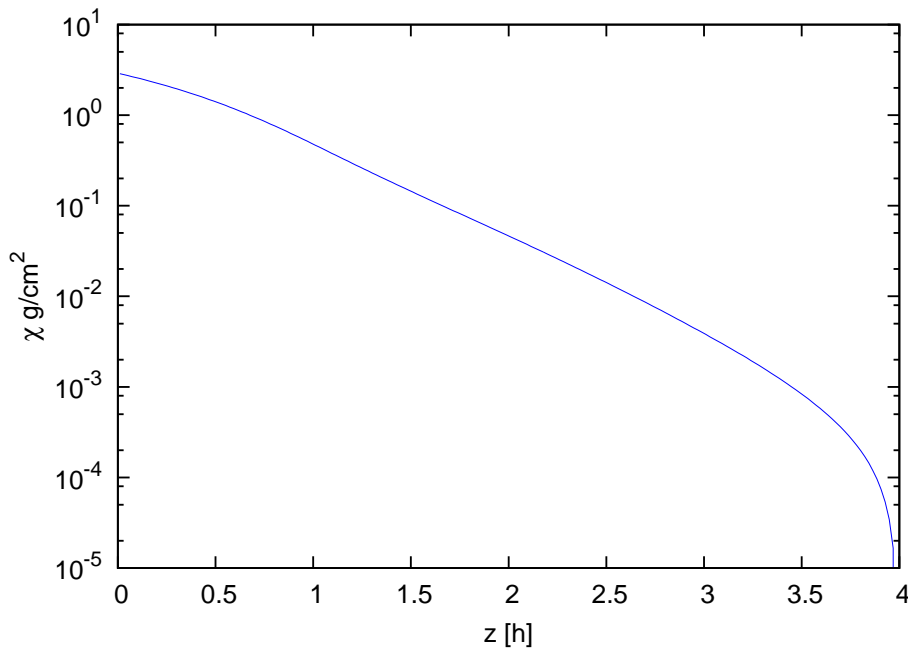


Figure 4.23: Vertical column density as a function of z up to the outside of the disk. Note that z is defined at the upper cell boundary in this plot.

actual timescale of turbulent mixing is more than two orders of magnitude larger than our assumption, $1/\Omega$, and turbulent mixing is not observed. Instead, we find that the timescale of vertical advection due to the disk wind is smaller than that of the ionization degree to reach equilibrium in the disk surface layer, and the ionization degree becomes smaller than the equilibrium value above/below about $\pm 2h$. This may change MRI activity in the surface layer in which ambipolar diffusion is effective. The inclusion of ambipolar diffusion in our numerical simulations is future work. In addition, the transfer of poorly ionized gas to the disk surface should strongly affect the chemical evolution of protoplanetary disks.

Originally we focused on the vicinity of dead zone boundaries, therefore we did not pay much attention to the disk surface. How-

ever, ionization due to far ultraviolet (FUV) radiation is very effective in surface layers. The typical depth to which FUV ionization is important is $\sim 0.02 \text{ g cm}^{-2}$ (Perez-Becker and Chiang, 2011). In Figure 4.23, we plot the column density as a function of z up to the outside of the disk (see Equation 2.16) of our simulation results. At $2h$, above which the ionization degree is lower than the equilibrium solution, the vertical column density is larger than 0.02 g cm^{-2} owing to the disk wind. Thus, our neglecting FUV ionization is not expected to produce large errors.

Chapter 5

Summary and Future Prospects

As the cradles of planets and satellites, protoplanetary and circumplanetary disks are important ingredients in their formation theories. Although it is difficult to observe circumplanetary disks owing to their small size and luminosity, observation of protoplanetary disks is a very active area of modern astrophysics. These observations imply that the gas in disks undergoes inward accretion toward the central stars. In order to have such inward gas accretion, the angular momentum of the gas must be removed. At present, MHD turbulence driven by the MRI is the most promising mechanism to explain this angular momentum transport. Since the gas in the disk must be sufficiently ionized for the MRI to operate, ionization degree is a key factor for the disk evolution.

We have developed a fast and accurate method to calculate the ionization degree in protoplanetary and circumplanetary disks. This method enables time-dependent calculations by using the following speed-up techniques:

- Gaussian charge distribution of dust grains

We adopted a Gaussian distribution for the charge distribution of dust grains (Okuzumi, 2009). With this approximation we can reduce the number of terms and equations to solve. This method is powerful, especially when we consider large dust grains or a small dust-to-gas mass ratio.

- Piecewise exact solution method

We utilized the piecewise exact solution method developed by Inoue and Inutsuka (2008). We analytically solve sets of rapid reaction terms in advance, and solve the remaining terms numerically with the analytic solutions as initial conditions of time integration. This method enables large time steps for calculations regardless of the timescale of rapid reactions.

The advantages of our method are that it is fast enough to be implemented into MHD codes and solve ionization dynamics at every time step, and it can resolve short-timescale phenomena such as the evolution of protoplanetary disks under variable X-ray ionization due to stellar flares. Because the dynamical timescale and chemical timescale are comparable, this method is also useful in circumplanetary disks. Our method can calculate the ionization degree quickly even when the dispersion of the grain charge distribution is very large (e.g. about 10^4 ; the number of basic equations to solve in this case is about 20,000).

We estimated the size of regions that can sustain magnetic turbulence in circumplanetary disks. We calculated the ionization degree in disks accounting for galactic cosmic rays, X-rays from the host star of the surrounding protoplanetary disk, and the decay of short-lived

radionuclides as ionization sources and evaluated the MRI activity. We adopted the α model and solved the diffusion equation of a disk with infalling mass flux from a protoplanetary disk obtained by Tanigawa et al. (2012). Even by varying parameters such as gas infall rate, magnetic field, dust-to-gas mass ratio, and radius of dust grains over a wide range, it was difficult to find a sufficiently large MRI-active region that can sustain well-developed turbulence, a region where both the Elsasser number is larger than unity and the magnetic pressure is sufficiently smaller than the gas pressure. We found that the surface density that can sustain well-developed MRI turbulence is $\Sigma \sim 0.001\text{--}0.01 \text{ g cm}^{-2}$ for a typical satellite-forming region, even without dust grains. Note that we have performed the calculations for a very optimistic set of assumptions for activation of the MRI. If metals are frozen out onto dust grains or cosmic rays are shielded by stellar activity, it becomes even more difficult to sustain the MRI.

This suggests that gas accretion in circumplanetary disks is slower than previously thought, and satellites can be formed slowly, perhaps by gravitational collapse. The temperature of the disk might be lower than expected because viscous heating is not very efficient.

There remain various uncertainties concerning circumplanetary disks, for example, how many dust grains remain after planet formation, and how large are they. We have to study the ionization degree in various cases. In this Thesis, we assumed dust grains of fixed size, thus the result may change if we consider the coagulation of dust grains, or if we consider ice as dust grains.

Recently, Turner, Lee, and Sano (2014) have investigated the possibility of the MRI in various models of circumplanetary disks from the literature. They choose the mid-plane value of plasma beta to be 10^3 . Their condition to sustain the MRI is that the magnetic pressure must be smaller than the gas pressure, which is satisfied below 3.7 scale heights. They concluded that there are active layers at the disk surface. Our results are consistent with theirs when we choose the condition that $\beta_z > 8\pi^2$ to sustain the MRI. For example, Figure 3 of Turner et al. (2014) and Fig. 3.5 of this Thesis show similar models of surface density, and both have surface active layers. Note that even if the MRI can be sustained at the disk surface, it does not necessarily mean that there is well-developed turbulence. When MRI turbulence is well developed, the magnetically dominated atmosphere encroaches on a lower altitude and the region of well-developed turbulence becomes smaller (Okuzumi and Ormel, 2013). The main difference between Turner et al. (2014) and our work is that we consider the criterion for turbulence to be well developed as well as that of just having the onset of the MRI.

As we mentioned earlier, if gravitational instability is the only mechanism of gas accretion, a massive and static disk will remain even after infall from the protoplanetary disk terminates. This suggests that the lifetime of circumplanetary disks may be longer than that of protoplanetary disks. Thus, perhaps we are more likely to be able to observe circumplanetary disks than previously thought (e.g., Mamajek et al., 2012), and satellite formation may occur over a long

timescale. On the other hand, it remains important to consider other mechanisms for angular momentum transport. A possible mechanism is spiral density waves caused by a non-axisymmetric potential (e.g., Machida et al., 2010; Martin and Lubow, 2011; Rivier et al., 2012), but this must be investigated in more detail. Another possibly important mechanism for satellite formation is the capture of planetesimals when they cross circumplanetary disks (Fujita et al., 2013) (see Estrada and Mosqueira, 2006, for the gas-poor case). Since our results suggest a large surface density, capture is expected to be effective. Non-axisymmetry in the density structure caused by these proto-satellites may play a role in angular momentum transport and it may be interesting to analyze that effect.

We implemented our scheme to calculate the ionization degree into the Athena MHD code (Stone et al., 2008) and examined the effects of non-equilibrium dynamics. When the charged-particle absorption by dust grains is effective, i.e., in the high-density regime, the timescale of chemical reactions is very small. Thus, the ionization degree reaches equilibrium immediately and the equilibrium approximation is valid for computing the dynamical evolution. When small dust grains are not abundant, however, the chemical timescale can be close to or longer than the dynamical timescale. In such a case, we have to take into account the non-equilibrium evolution of ionization chemistry to investigate the accretion disk evolution.

Assuming the late evolution stage of a protoplanetary disk when the disk gas has mostly dissipated and small grains have grown larger,

we performed 3D numerical simulations using the Athena code. Consistent with Suzuki and Inutsuka (2009) and Suzuki et al. (2010), the disk wind, a flow from inside the disk to the outside caused by MHD effects, can be seen in our simulations. We find that the vertical distribution of electrons changes from the equilibrium solution of the corresponding height. This is because the disk wind transfers poorly ionized gas near the disk mid-plane to the upper and lower surface layers. This may affect MRI activity in the ambipolar regime. Also, this effect may influence chemical evolution. Further investigation with a wider parameter region is planned for our future work. Since the dynamical timescale is smaller in circumplanetary disks, the effect of vertical advection/turbulent mixing is thought to be more important, and it may be interesting to carry out similar work in circumplanetary disks.

Acknowledgments

First of all, I would like to express my deepest appreciation to my supervisor, Shu-ichiro Inutsuka, for his insightful guidance during the course of my study. I am extremely grateful to Satoshi Okuzumi for his indispensable wisdom. I have enjoyed collaborating with Takeru K. Suzuki, Hiroshi Kobayashi, Takayuki Tanigawa, and Sanemichi Z. Takahashi. I am thankful for the support of Kengo Tomida, Kazunari Iwasaki, and Yusuke Tsukamoto. I would like to offer special thanks to my friends Soonyoung Roh, Jennifer M. Stone, and Satoko Sorahana for being great office mates, for fun language exchanges, and for good advice, both professional and personal. I appreciate the kind help offered by Jennifer M. Stone in scientific writing (and for always checking my English, not only in this Thesis). Thank you to Torsten Stamer for making English corrections to this Thesis. I am indebted to Machiko Yoshida for keeping the laboratory running smoothly. I acknowledge Tsutomu T. Takeuchi for support from the Strategic Young Researchers Overseas Visits Program for Accelerating Brain Circulation from MEXT (R2405). This work was supported by JSPS KAKENHI Grant Number 24-4770. Numerical computations were in part carried out on Cray XC30 at the Center for Computa-

tional Astrophysics, National Astronomical Observatory of Japan.

Bibliography

- P. Andre, D. Ward-Thompson, and M. Barsony. *ApJ*, 406:122–141, (1993).
- P. J. Armitage. *Astrophysics of Planet Formation*. Astronomical Society of the Pacific Conference Series. (2009).
- B. A. Ayliffe and M. R. Bate. *Mon. Not. R. Astron. Soc.*, 393:49–64, (2009).
- S. A. Balbus and J. F. Hawley. *ApJ*, 376:214–233, (1991).
- S. A. Balbus and J. C. B. Papaloizou. *ApJ*, 521:650–658, (1999).
- O. M. Blaes and S. A. Balbus. *ApJ*, 421:163–177, (1994).
- R. M. Canup and W. R. Ward. *AJ*, 124:3404–3423, (2002).
- R. M. Canup and W. R. Ward. *Nature*, 441:834–839, (2006).
- L. I. Cleeves, F. C. Adams, and E. A. Bergin. *ApJ*, 772:5, (2013).
- A. Crida and S. Charnoz. *Science*, 338:1196–, (2012).
- B. Ercolano and A. E. Glassgold. *Mon. Not. R. Astron. Soc.*, 436: 3446–3450, (2013).
- P. R. Estrada and I. Mosqueira. *Icarus*, 181:486–509, (2006).

- Y. I. Fujii, S. Okuzumi, and S. Inutsuka. *ApJ*, 743:53, (2011).
- Y. I. Fujii, S. Okuzumi, and S. Inutsuka. *The Labyrinth of Star Formation, Advances in Solid State Physics*, 36:81, (2014).
- Y. I. Fujii, S. Okuzumi, T. Tanigawa, and S. Inutsuka. *ApJ*, 785:101, (2014).
- T. Fujita, K. Ohtsuki, T. Tanigawa, and R. Suetsugu. *AJ*, 146:140, (2013).
- P. Goldreich and D. Lynden-Bell. *Mon. Not. R. Astron. Soc.*, 130:125–158, (1965).
- J. Goodman and R. R. Rafikov. *ApJ*, 552:793–802, (2001).
- O. Gressel and U. Ziegler. *Computer Physics Communications*, 176:652–659, (2007).
- O. Gressel, R. P. Nelson, and N. J. Turner. *Mon. Not. R. Astron. Soc.*, 422:1140–1159, (2012).
- E. Gullbring, L. Hartmann, C. Briceño, and N. Calvet. *ApJ*, 492:323–341, (1998).
- K. E. Haisch, Jr., E. A. Lada, and C. J. Lada. *ApJL*, 553:L153–L156, (2001).
- L. Hartmann, N. Calvet, E. Gullbring, and P. D'Alessio. *ApJ*, 495:385–400, (1998).
- J. F. Hawley, C. F. Gammie, and S. A. Balbus. *ApJ*, 440:742–763, (1995).

- C. Hayashi. *Progress of Theoretical Physics Supplement*, 70:35–53, (1981).
- J. Igea and A. E. Glassgold. *ApJ*, 518:848–858, (1999).
- M. Ilgner and R. P. Nelson. *A&A*, 445:205–222, (2006).
- M. Ilgner and R. P. Nelson. *A&A*, 483:815–830, (2008).
- T. Inoue and S. Inutsuka. *ApJ*, 687:303–310, (2008).
- S. Inutsuka and T. Sano. *ApJL*, 628:L155–L158, (2005).
- A. Johansen, A. Youdin, and H. Klahr. *ApJ*, 697:1269–1289, (2009).
- S. L. Keith and M. Wardle. *Mon. Not. R. Astron. Soc.*, 440:89–105, (2014).
- C. J. Lada. *Star Forming Regions, IAU Symposium*, 115:1–17, (1987).
- J. J. Lissauer and G. R. Stewart. In *Protostars and Planets III*, pages 1061–1088, (1993).
- S. H. Lubow and R. G. Martin. *ApJL*, 749:L37, (2012).
- M. N. Machida, E. Kokubo, S. Inutsuka, and T. Matsumoto. *Mon. Not. R. Astron. Soc.*, 405:1227–1243, (2010).
- E. E. Mamajek, A. C. Quillen, M. J. Pecaut, F. Moolekamp, E. L. Scott, M. A. Kenworthy, A. Collier Cameron, and N. R. Parley. *AJ*, 143:72, (2012).
- R. G. Martin and S. H. Lubow. *Mon. Not. R. Astron. Soc.*, 413:1447–1461, (2011).

- F. Masset. *A&A Suppl.*, 141:165–173, (2000).
- I. Mosqueira and P. R. Estrada. *Icarus*, 163:198–231, (2003).
- T. Muto, T. K. Suzuki, and S. Inutsuka. *ApJ*, 724:448–463, (2010).
- M. Ogihara and S. Ida. *ApJ*, 753:60, (2012).
- S. Okuzumi. *ApJ*, 698:1122–1135, (2009).
- S. Okuzumi and S. Hirose. *ApJ*, 742:65, (2011).
- S. Okuzumi and C. W. Ormel. *ApJ*, 771:43, (2013).
- M. Oppenheimer and A. Dalgarno. *ApJ*, 192:29–32, (1974).
- D. Perez-Becker and E. Chiang. *ApJ*, 727:2, (2011).
- G. Rivier, A. Crida, A. Morbidelli, and Y. Brouet. *A&A*, 548:A116, (2012).
- T. Sano and S. M. Miyama. *ApJ*, 515:776–786, (1999).
- T. Sano, S. M. Miyama, T. Umebayashi, and T. Nakano. *ApJ*, 543:486–501, (2000).
- T. Sasaki, G. R. Stewart, and S. Ida. *ApJ*, 714:1052–1064, (2010).
- N. I. Shakura and R. A. Sunyaev. *A&A*, 24:337–355, (1973).
- J. M. Stone, T. A. Gardiner, P. Teuben, J. F. Hawley, and J. B. Simon. *ApJS*, 178:137–177, (2008).
- T. K. Suzuki and S. Inutsuka. *ApJL*, 691:L49–L54, (2009).
- T. K. Suzuki, T. Muto, and S. Inutsuka. *ApJ*, 718:1289–1304, (2010).

- T. Takata and D. J. Stevenson. *Icarus*, 123:404–421, (1996).
- M. Tamura. *American Institute of Physics Conference Series*, 1158: 11–16, (2009).
- T. Tanigawa, K. Ohtsuki, and M. N. Machida. *ApJ*, 747:47, (2012).
- N. J. Turner and T. Sano. *ApJL*, 679:L131–L134, (2008).
- N. J. Turner, T. Sano, and N. Dziourkevitch. *ApJ*, 659:729–737, (2007).
- N. J. Turner, M. H. Lee, and T. Sano. *ApJ*, 783:14, (2014).
- T. Umebayashi and T. Nakano. *ApJ*, 690:69–81, (2009).
- T. Umebayashi and T. Nakano. *PASJ*, 33:617–635, (1981).
- A. L. Uribe, H. Klahr, and T. Henning. *ApJ*, 769:97, (2013).
- W. R. Ward. In *Completing the Inventory of the Solar System*, volume 107 of *Astronomical Society of the Pacific Conference Series*, pages 337–361, (1996).